UNIVERSITÀ DEGLI STUDI DELLA TUSCIA DI VITERBO

DIPARTIMENTO DI SCIENZE AGRARIE E FORESTALI (DAFNE)
DIPARTIMENTO DI ECONOMIA, INGEGNERIA, SOCIETÀ E IMPRESA (DEIM)

Corso di Dottorato di Ricerca in

ECOSISTEMI E SISTEMI PRODUTTIVI
(Curriculum: Ingegneria dei biosistemi)
XXX Ciclo

Biomass gasification plants: different configuration and development of gas sensors for on-line and high temperature analysis

(**s.s.d. ING-IND/09**)

Tesi di dottorato di:

Dott.ssa Vanessa Pallozzi

Coordinatore del corso

Prof. Silvio Franco

Tutor

Prof. Maurizio Carlini

Co-tutor

Prof. Enrico Bocci
Ing. Andrea Di Carlo
Dott. Fabio Zaza

A.A. 2016/2017

Abstract

Productive systems and their exploitation of conventional fossil fuels for their energy needs generate increasingly negative impacts on the global ecosystem, involving all sectors as economic, social and environmental. Human activities and global researches, therefore, have to move towards renewable energies and improvements in energy efficiency. Among renewables, biomass is a very attractive resource since its great and widespread availability, its possibility to be stored and to produce both heat and power. Gasification is currently one of the most profitable process for biomass conversion, but more efforts on the process reliability and efficiency need to be conducted in order to enhance the use of this technology. Chemoresistive gas sensors are a suitable choice in this sense, providing efficient controls and measurements with simplicity in function, relatively low cost and direct high temperature operation. The aim of this work is, then, to study and develop chemoresistive gas sensors, based on perovskite oxides, for the application in biomass waste gasification plants with different configurations and purposes. Hence, experimental studies on biomass steam gasification in a bench-scale and in a pilot 100 kW_{th} innovative dual bubbling fluidized bed (DBFB) gasifier, together with those on gas cleaning and conditioning system based on dolomite guard bed coupled with an exhaust vegetable oil scrubber, were performed. Producer gases with high energetic value were obtained, having also a tars content below the limits accepted in an internal combustion engine thanks to good and durable operation of the gas cleaning system. Moreover, a global simulation and a sensitivity study on a commercial plant (1 MW_{th} input) for the production of pure hydrogen by means of the innovative DBFB gasifier have been carried out, in order to evaluate its global efficiency and to identify the streams and their main features for sensors applications. It was chosen to globally analyse a biomass gasification plant for pure hydrogen production, since its higher restrictions in terms of contaminants and syngas quality and its high temperature gas conditioning steps. Results demonstrated the great variability of plant's performances dependent by process input parameters as steam to biomass ratio in the gasifier and operating temperature and residence time of water gas shift reactor. Synthesis, characterization and testing of novel perovskite materials for sensing purposes were then conducted. After theoretical and chemometric evaluations focused on reaction parameters, such as citric acid to metal ions ratio, pH acidity and fuel to

oxidizer ratio, for auto-combustion synthesis improvement and optimization, powders of $LaTi_{0.4}Fe_{0.6}O_3$ were prepared and tested in CO, H_2 and H_2S atmosphere, providing high sensitivity and thermochemical stability for CO sensing. Additional investigations on the effects of titanium amount were also performed, revealing that the best solutions for CO detection are $LaTi_{0.2}Fe_{0.8}O_3$ or $LaTi_{0.4}Fe_{0.6}O_3$. H_2 sensing was, instead, enhanced with partial substitution with cobalt ions in the based materials, in particular $LaCo_{0.4}Fe_{0.6}O_3$ provided a very high sensitivity. A chemometric analysis was also carried out for the evaluation of optimal tests parameters.

Keywords: *biomass; gasification; chemoresistive gas sensors; perovskites; $LaFeO_3$.*

Estratto

I sistemi produttivi e il relativo sfruttamento delle convenzionali fonti fossili di energia per il soddisfacimento dei bisogni energetici generano sempre maggiore impatto negativo sull'ecosistema globale, investendo tutti i settori quali quello economico, sociale ed ambientale. Le attività umane e il mondo della ricerca, quindi, devono necessariamente muoversi verso le energie rinnovabili e il miglioramento dell'efficienza energetica. Tra le rinnovabili, la biomassa è una risorsa altamente vantaggiosa grazie alla sua grande e diffusa disponibilità in tutto il mondo, la sua possibilità di stoccaggio, per produrre energia contestualmente alla sua necessità, e la produzione sia di energia termica che elettrica. La gassificazione è uno dei processi più efficienti per la conversione delle biomasse, ma necessita comunque di maggiori avanzamenti sull'affidabilità e l'efficienza del processo in modo da incoraggiare l'uso di questa tecnologia. I sensori di gas chemoresistivi rappresentano un'ottima opportunità in questo senso, fornendo efficaci misure e controlli del sistema insieme a semplicità di funzionamento, relativamente basso costo e funzionamento on-line e ad alta temperatura. Lo scopo di questo lavoro è, quindi, lo studio e lo sviluppo di sensori di gas chemoresistivi, basati su ossidi perovskitici, per l'applicazione in impianti di gasificazione di biomassa residuale con diverse scopi e configurazioni. Sono stati effettuati, quindi, studi sperimentali su gasificazione di biomassa con vapore sia in un reattore di scala di laboratorio che in un pilota da 100 kW_{th} di energia di ingresso, basato su un innovativo gassificatore a doppio letto fluido bollente (DBFB), oltre a prove sperimentali su un sistema di pulizia e condizionamento del gas prodotto basato su un letto di guardia catalitico di dolomite e uno scrubber ad olio vegetale esausto. Sono stati ottenuti gas con alto contenuto energetico e con contenuto di tars entro i limiti accettati da un motore a combustione interna grazie al lungo e buon funzionamento del sistema di pulizia del gas. In più, è stata effettuata una simulazione globale di un impianto commerciale (1 MW_{th}) per la produzione di idrogeno puro attraverso il gassificatore DBFB, in modo da valutare la sua efficienza globale e da identificare i punti e le relative principali caratteristiche per l'applicazione dei sensori. I risultati hanno dimostrato la grande variabilità delle prestazioni dell'impianto al variare dei parametri di input al processo quali steam to biomass (SB) e temperatura operativa e tempo di residenza del reattore di water gas shift. Inoltre, sono state portate avanti la sintesi, la caratterizzazione e il test di innovativi materiali perovskitici

per l'utilizzo come materiali sensitivi. Dopo analisi teoriche e chemometriche sul perfezionamento e ottimizzazione del metodo di sintesi, sono state preparate polveri di $LaTi_{0.4}Fe_{0.6}O_3$ e testate in presenza di CO, H_2 e H_2S, fornendo alta sensibilità e stabilità termica per la misura del monossido di carbonio. Sono state allora effettuate ulteriori analisi sull'effetto del contenuto di titanio: $LaTi_{0.2}Fe_{0.8}O_3$ o $LaTi_{0.4}Fe_{0.6}O_3$ sono risultate essere le migliori soluzioni per l'individuazione del CO. La misura dell'idrogeno, invece, è stata perfezionata con la parziale sostituzione con ioni di cobalto nei materiali di base: in particolare, il materiale $LaCo_{0.4}Fe_{0.6}O_3$ ha fornito un'alta sensibilità. Infine, è stata condotta anche un'analisi chemometrica per la valutazione dei parametri di test ottimali.

Parole chiave: *biomasse; gassificazione; sensori di gas chemoresistivi; pervskiti; $LaFeO_3$.*

Contents

Figures index

Tables index

Nomenclature

Latin letters

A	Arrhenius parameter (1/s)
b_{ij}	coefficient of multivariate polynomial function
c_i	conversion rate (%)
C_i	molar concentration (M)
CA/M	citric acid to metal ions ratio
E	activation energy (kJ/mol)
F/O	fuel to oxidizer ratio
$k_{\alpha i}$	reaction equilibrium constant
$\dot{m}_i$	mass flow rate (kg/s, kg/h)
n	number of moles
p	statistical significance
Q	gas flow rate (Nml/min)
R_i	sensor response (Ω)
S	sensitivity
t	Goldshimidt tolerance factor
X_i	concentration (ppm)
x	titanium content

Greek letters

α_i	relative concentration
σ	conductivity
φ	equivalence ratio
Φ	normalized equivalence ratio
η	hydrogen chemical efficiency
v	speed of response (kΩ/s)

Abbreviation

BFB	Bubbling Fluidized Bed
CA	Citric Acid
CFB	Circulating Fluidized Bed
CHP	Combined Heat and power
DBFB	Dual Bubbling Fluidized Bed
DeS	Desulphurization reactor
EDS	Energy Dispersive X-ray Spectroscopy
ER	Equivalence Ratio
FB	Fluidized Bed
FC	Fuel Cell
GHG	greenhouse gas emissions
HHV	Higher Heating Value
ICE	Internal Combustion Engine
MFC	Mass Flow Controller
mGT	Micro Gas Turbine
MCFC	Molten Carbonate Fuel Cell

LHV	Lower Heating Value
PEMFC	Proton Exchange Membrane Fuel Cell
PSA	Pressure Swing Adsorber
SB	Steam to Biomass
SEM	Scanning Electron Microscope
SOFC	Solid Oxide Fuel Cell
TC	Thermocouple
WGS	Water Gas Shift
XRD	X-Ray Diffraction

Subscription

bio,daf	biomass dry and ash free
e	electric
eq	equilibrium
0	baseline
a	analyte
M	metal ions
st	stoichiometric
t	total
th	thermal

Introduction

Energy supply is at the basis of every productive system, from the agricultural to the industrial ones. Since the industrial revolution in the XIX century, the impact of the global "techno-system" has generated increasingly negative impacts on the planet balance considering all sectors (economic, social, environmental), due to the unsustainable policies adopted. The 5° Assessment Report of the Intergovernmental Panel on Climate Change (IPCC) affirms that the human influence on climate is clear and it could be, with a probability larger than 95%, the prevailing responsible of the global warming registered from 1950 onwards [1]. In addition, the Millennium Ecosystem Assessment estimated that 60% of the world's ecosystems risks the extinction as a direct consequence of human activities [2]. The necessity of a radical change is then evident. The crucial mission of global Nations and research fields is to move productive systems towards the preservation of ecosystems, together with the instauration of an economic and social sustainable development. With these scopes, a number of worldwide and European policies were arranged and are still developing, such as Kyoto Protocol in the 1997, Europe 2020 strategy in 2010, Energy Roadmap 2050 in 2011, Paris Agreement in 2015 and the Italian National Energetic Strategies (SEN), which implement the European Directives at a national level [3–7]. All of these global strategies aim to slow down the global warming, whose main causes are greenhouse gas emissions (GHG), especially those of carbon dioxide (CO_2) [8,9], and to provide an alternative solution to the conventional energy supply sources. Conventional fossil fuels, in fact, besides being the principal responsible for GHG emissions, are non-renewable energy sources, whose availability is gradually decreasing and whose production is concentrated in a limited number of countries: the conversion to renewable and sustainable energy sources is then fundamental to avoid energetic crisis and to preserve global ecosystem. The energy supply issue, hence, concerns different worldwide society sectors and the cooperation between all of them: environmental, energetic, productive, social and most of all economic. For this reason, the United Nations Conference in 2012, "Rio+20", focused the attention principally on the developing of a *green economy*, for a sustainable developing and the poverty elimination, overcoming the present economic crisis and avoiding the occurring of new ones. It is defined as an economy that leads to an improving of human wealth and social equity, reducing as much as possible environmental

and ecological risks. It aims to low-carbon usage, high efficiency of the resource and a social interest [10]. Worldwide policies are oriented in this perspective, including in their directive three key targets: the reduction of GHG emissions, the promotion of renewable energy resources and the improvement in energy efficiency, all for limiting the global warming well below 2°C. Therefore, research studies on renewables energies and tools for maximization of energy efficiency and reliability of relative power plants are extremely important. Among renewables, biomass is one of the most promising resource, since its great advantages. Biomass, in fact, is characterized by a great diffusion and high availability all over the world, allowing to establish a more sustainable and equilibrated society, besides a carbon free ecosystem. With the possibility to use biomass waste for energy purpose, then, it is possible to obtain both the reduction of dependence from fossil fuels and of environmental problems related to disposal and to methane emissions that occur in their degradation process. Moreover, with biomass is possible to limit the uncertainty typical of renewables, thanks to the possibility of storage and accumulation, and it is also possible to produce both heat and power production [11,12]. Gasification is currently considered one of the most effective technologies to produce power and biofuels from biomass. The optimization of biomass conversion plants, however, could be improved by using an efficient system control, able to instantly measure gas composition and other important parameters and simultaneously adjust input conditions of the process, in order to maximize the reliability and efficiency of the whole plant. Standard analytical techniques for the monitoring of hydrocarbons and other involved gases, based on gas/liquid chromatography and mass spectrometry, besides being relatively expensive and large in size, are not able to operate directly, nor at high temperatures. Chemoresistive gas sensors, instead, are a very promising technology in this sense, due to their simple structure, small size, low cost, possibility to work on-site, coupled with good sensitivity, stability and speed of response [13,14]. Moreover, using perovskite-type oxides as sensing material, raises the possibility to operate also at relatively high temperatures as those involved in biomass gasification systems.

The aim of this work is to study and develop chemoresistive gas sensors, based on perovskite oxide, for the application in biomass waste gasification plants. In particular, a preliminary research activity was focused on an innovative biomass steam gasification, the relative different plant configuration and gas cleaning techniques for the different biomass

conversion purposes. After obtained an extended knowledge on biomass gasification system and their better integration with gas sensor devices, research activities were focused on the synthesis, characterization and testing of innovative perovskite materials for the sensing of typical biomass gasification gases. The activities involved and the results obtained within this work were conducted thanks to the cooperation of different national and international universities and research centres, as Tuscia University, Marconi University, Sapienza University, ENEA research centre in Casaccia and EC-Joint Research Centre in Petten.

In *chapter 1* the state of art of biomass gasification, gas cleaning and fuel utilization is presented, while in *chapter 2* that of gas sensors, their sensing material and operation is provided. C*hapter 3* reports the experimental activity performed in the bench-scale fluidized bed gasifier, that in the pilot dual fluidized bed gasifier and the global simulation on a real gasification power plant. In C*hapter 4* the experimental activities carried out in the field of chemoresistive gas sensors are discussed, including studies on synthesis, materials and testing optimization. Finally, in *chapter 5* some conclusion and outlooks for the future have been drawn.

1. Biomass Gasification

Biomass

Biomass is ever since the major source of energy in most of the developing countries. Unfortunately, it was not always completely exploited. Starting from the end of the XIX century, indeed, its importance was gradually reduced since the arising of the fossil fuels era. In XX century, however, the First Oil Shock in 1970 allowed a new increase of the percentage of energy produced by biomass. The crucial role of biomass as source of energy is today totally recognized, thanks to the increasing awareness of the depletion of fossil fuels and the greater attention of the population to environmental issues. Since this, the worldwide government policies and research activities are always more interested in biomass conversion technologies development and establishment.

Biomass is defined as all the organic materials on Earth, vegetal or animal, that have stored sunlight in the form of chemical energy and that could be transformed for energy purposes. Even if is difficult to find a generally accepted definition, according to the United Nation Framework Convention on Climate Change (UNFCCC, 2005) it is defined as "*non-fossilized and biodegradable organic material originating from plants, animals and micro-organisms. This shall also include products, by-products, residues and waste from agriculture, forestry and related industries as well as the non-fossilized and biodegradable organic fractions of industrial and municipal wastes*". The same definition is accepted even by Italian regulations. In general, biomass directly or indirectly originates from the process of photosynthesis and thus constitutes an important renewable energy source derived from the sun. However, fossil fuels (coal, oil and natural gas), though they were formed in past eras starting from organic vegetable and animal matter, and their derivatives (such as plastics) are not considered biomass, since their regeneration time is far greater than the utilization time. The materials considered as biomass are [15]:

- woody and herbaceous species deriving from agricultural crops and forestry;
- agricultural and forestry residues (straw, brushwood, barks, etc.);
- agro-industrial residues (rice husk, olive residues, bagasse, etc.);
- livestock residues (animal manure, etc.);
- organic fraction of municipal solid waste, also called humid fraction.

Depending on its origin, it is possible to have residual biomass or biomass derived from dedicated energy crops. Residues and waste matter of agricultural, agro-industrial and forestry origin obviously fall within the first case, together with the humid fraction of Municipal Solid Wastes (MSW). Energy recovery from residual biomass is doubly advantageous because on one hand it reduces dependence from fossil fuels and on the other hand it alleviates environmental problems related to their disposal and to methane emissions that occur in their degradation process (it must be remembered that methane is twentyfold more powerful than carbon dioxide as a greenhouse gas). Biomass can additionally be classified as [16]:

- triglycerides (rape, soy, sunflower, etc.), from which vegetable oils and biodiesel are produced;
- amorphous sugars (starch, glucose, etc.), used to produce bioethanol;
- lignocellulosic or woody (poplar, black locust, grasses, miscanthus etc.), dedicated to solid and gas fuel production.

Biomass is a renewable energy resource, since its generation rate could surely be greater than the consumption one. It is evident that, for an environmentally sustainable utilisation of biomass, it is necessary to couple the collection of natural material with a following process of reinstatement (reforestation, etc.). Moreover, it is also CO_2 neutral, since amounts of carbon monoxide generated during biomass conversion are equal to those absorbed during its growth. Apart from these good characteristics, typical of all renewable resources, biomass shows also other great advantages [17,18]. Biomass, indeed, is the fourth worldwide energy resource (following oil, coal and natural gas). Besides being an abundant resource, biomass is even widespread almost all over the world, with the possibility of reducing countries supplying and energy depending issues and helping to create a more sustainable system even from a social point of view. Moreover, it allows to solve or at least limit the conventional supplying uncertainty of renewable sources, since it can be accumulated, and then used when necessary. In addition, it can be converted in solid, liquid or gaseous fuels, suitable for simultaneous heat and power production, differently from other renewable energies. Finally, it allows the exploitation of unemployed areas with dedicated crops or the conversion of agricultural lands, generating positive occupational implications.

Also some disadvantages characterized biomass as energy source, even if they are not expected to affect its attractiveness [19]. First of all, a low energy density, both in terms of lower heating value (LHV), that for dry solid biomass is about 15 ÷ 20 MJ/kg (versus 42 MJ/kg of oil and 50 MJ/kg of methane) and, more in general, in terms of land productivity, since wide areas are required to produce significant quantities of raw material. This affects also transport, storage and handling in complexity and costs. Moreover, production is generally strongly dependent on weather and environmental conditions and it is not constant during the year, besides being not cost-free because necessity of irrigation and fertilisers. Some of these issues, however, can be defeated in the case of residual and biomass waste and with the installation of conversion plant of proper size, namely the one related to the biomass availability in the local installation area.

Biomasses are characterized by different chemical properties [20], such as moisture, chemical composition and lower heating value. Two kind of analysis are at the basis of biomass characterization: the ultimate and proximate analyses. The ultimate analyses consist on the measurements of the content of the chemical elements, such as Carbon (C), Hydrogen (H), Oxygen (O), Sulphur (S) and Nitrogen (N), usually expressed in mass % on dry material (wt% dry) or on dry and ash free material (wt% daf) or as received material (wt% ar). The proximate analysis, instead, indicates the moisture, ash, volatile matter and fixed carbon content. The ash is usually expressed in weight % on dry bases or in weight % as received material, the water in weight % on wet bases and the total amount of volatile is expressed in weight % on dry material or as received material or on dry and ash free material. The fixed carbon is calculated as the remaining part.

The evaluation of biomass chemical properties is fundamental for the utilization of the resource itself, since they highly affect the kind of conversion process to be used. The conversion processes can be grouped as [21]:

- mechanical/physical (drying and dewatering);
- biochemical (microbial conversion, biochemical liquefaction);
- thermochemical (combustion, pyrolysis and gasification).

Generally, oleaginous crops are more suitable for mechanical and physical conversion processes. Regarding the other two groups, the choice between them is influenced mostly

by two fundamental biomass parameters: moisture and carbon to nitrogen ratio (C/N). Indeed, biomasses with moisture content larger than 30% and C/N lower than 30 are more suitable for biochemical conversion, while in the opposite situation thermochemical conversion is the preferable choice. Moreover, alcoholigen crops are proper biomass for the former conversion process, while lignocellulosic crops for the latter.

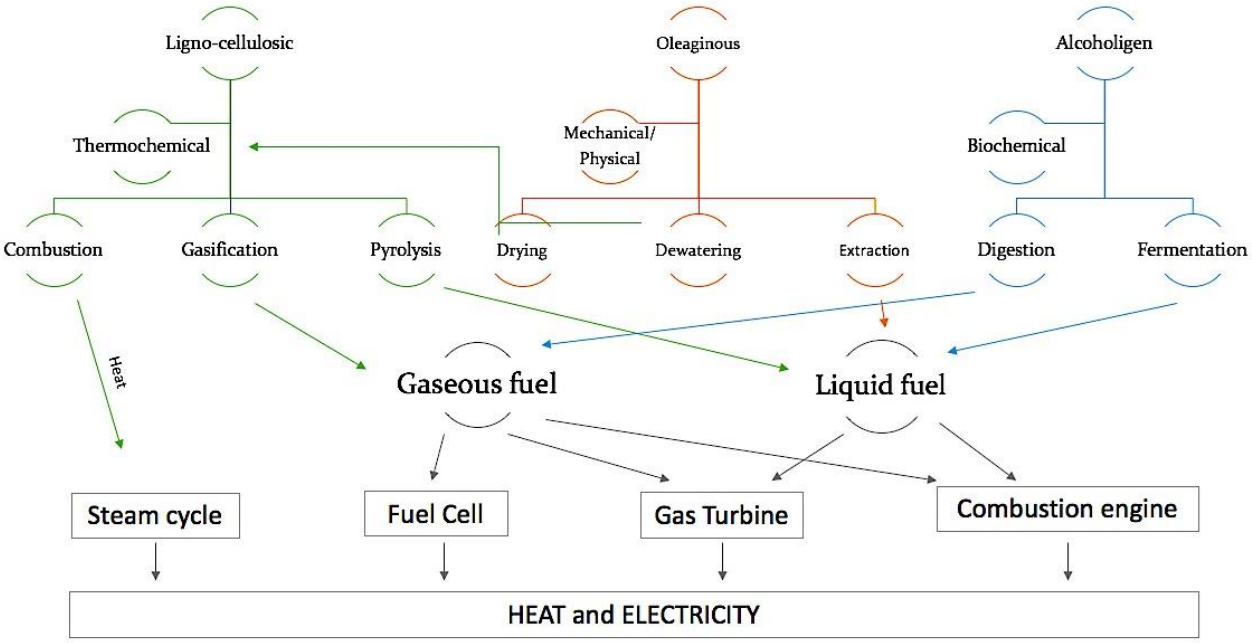

Figure 1. Biomass conversion processes and possible end-use applications

Among thermochemical process, the main used are the simple direct combustion, the pyrolysis, that is a conversion at 400-800 °C in totally absence of oxidizing agent, and gasification, that is a partial oxidization at temperature higher than 800 °C.

In this work, we focused the attention in lignocellulosic biomasses, because the cheapest, most abundant, fastest growing and with less moisture and higher energetic content, and their consequent thermal conversion, in particular by means of gasification [16,22].

Gasification for biomass conversion

Gasification is a thermochemical conversion process of biomass to a gaseous fuel by heating by means of a gasifying medium such as air, oxygen or steam. Unlike combustion where chemical bonds are broken to release energy, gasification packs energy into chemical bonds in the product gas. The great attraction of gasification is that it can convert waste or

low-priced fuels, such as biomass, into a high-value product gas. In addition, the gas produced is easier to be handled, stored or transported than the original biomass. Gasification provides higher efficiency and residence time respect to other conversion processes [20,23,24].

The gasification reaction is generally defined as:

$$CH_{\alpha}O_{\beta}+H_2O \rightarrow aC+bH_2+cCO+dH_20+eCO_2+fCH_4+gCH_xO_y \quad \textbf{(1.1)}$$

The gasification process can be divided in four steps [25–27]:

- Drying: dehydratation at 100-150 °C of biomass with steam release useful for successive gasification step;
- Pyrolysis: termochemical decomposition of biomass between 200 and 650 °C and in totally absence of oxidizing agents, producing gas, solid residue (charcoal) and tars (heavy condensable hydrocarbons);
- Combustion: oxidization of charcoal, some gases and vapours between 700 and 1200 °C;
- Gasification: reduction of pyrolysis products and residual charcoal between 800 and 100 °C.

The gasification step involves a number of endothermic reactions, whose heat requirement could be provided either by indirect or external heat source (indirect gasification) or directly by combustion of the fuel (direct gasification).

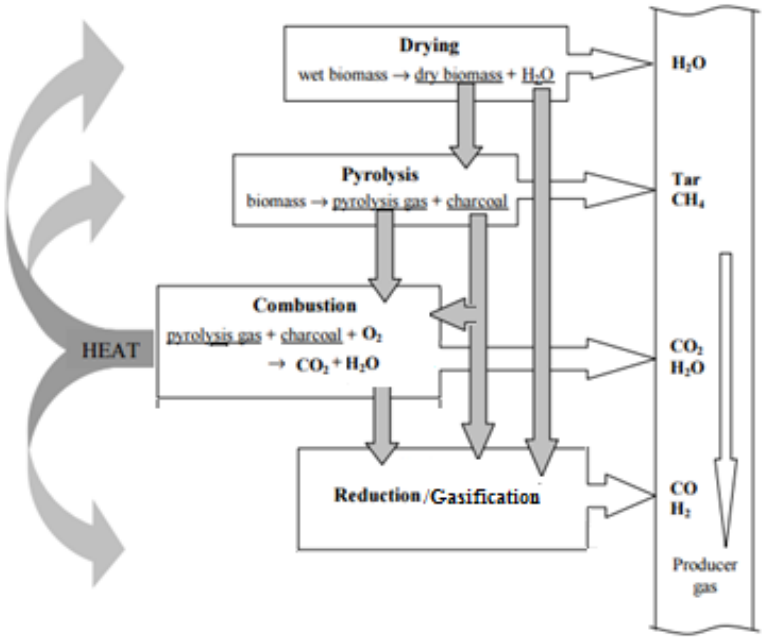

Figure 2. Scheme of reaction and heat flow in gasification process (adapted from [28]*)*

Reactions involved in the entire process are summarized in *Table 1*. The last two reactions are the principal ones that provide the necessary heat for the maintenance of a direct gasification process.

Water gas equilibrium reaction	$C + H_2O + 122.6\ kJ/mol \rightarrow CO + H_2$
Boudouard reaction	$C + CO_2 + 164.9\ kJ/mol \rightarrow 2CO$
Hydrogasification	$C + 2H_2 \rightarrow CH_4 + 74.9\ kJ/mol$
Methane Steam reforming	$CH_4 + H_2O + 206\ kJ/mol \rightarrow CO + 3H_2$
Water gas shift	$CO + H_2O \rightarrow CO_2 + H_2 + 41\ kJ/mol$
Tar steam reforming	$CH_xO_y + H_2O \rightarrow CO + H_2$
Char combustion	$C + O_2 \rightarrow CO_2 + 394\ kJ/mol$
Char partial oxidation	$C + 0.5O_2 \rightarrow CO + 111\ kJ/mol$

Table 1. Reactions involved in biomass gasification process

In any case, the product gas obtained from the entire process is a gas mixture mainly composed by H_2, CO, N_2, CO_2, CH_4, H_2O and other hydrocarbons, named syngas. It could be then used in those numerous industrial applications which need of both heat and electrical energy, such as gas turbine [29,30], internal combustion engine (ICE) [31–33], fuel cells (FC) and production of liquid or gaseous biofuels, like hydrogen or biodiesel [34–37]. However, in

syngas stream also some impurities and undesired components are present, such as sulphur and nitrogen compounds, chlorine, tars, particulate, volatile inorganics, ashes and trace elements. Of course, syngas needs to be treated, conditioned and cleaned from these impurities prior to be used in the final utilization systems, in order to prevent severe damage of them [38–40]. More details on this issue are provided in the next paragraph.

A crucial element for gasification process is the gasifying agent, which reacts with solid carbon and heavier hydrocarbon to convert them into low-molecular-weight gases like CO and H2. The possible gasifying agents are oxygen, air, steam or a mix of them [41]. The kind of gasifying agent used highly influence the energetic content of syngas obtainable, besides the complexity and cost of the system. The lower heating value (LHV), indeed, can range between the minimum of 4-7 MJ/Nm^3, typical of syngas produced with air, and the maximum of 10-18 MJ/Nm^3, typical of syngas produced with oxygen. Gasification with steam provides syngas with intermediate energetic values, but at the same time allows to quite reduce costs of biomass conversion respect to the oxygen configuration, whose production is pretty expensive [42,43]. The differences in energetic values are strictly dependent from the nitrogen content: high dilution in N_2 leads to lower LHV, as in the case of gasification with air. The quantities of gasyfing agents respect to biomass amounts, together with operating temperatures and biomass used, strongly influence the process outputs. In particular, steam to biomass ratio (SB) is the ratio between the mass flow of steam and the mass flow of biomass sent to the reactor. Equivalence ratio (ER), moreover, is the ratio between the oxygen sent to the reactor and the quantity of stoichiometric oxygen needed for the complete combustion of biomass. Generally SB ranges between 0 and 2, and ER has its theoretical optimal value in 0.25-0.3 [20]. Higher values of ER generate lower tar concentration in the product gas, but it also reduces the quality of the gas, as decreases its heating value. Increasing SB ratio also reduced tar content, by promoting the steam reforming reactions, however it cannot be higher than 2 for reasons of energy balance of the overall plant.

Different kinds of reactor are currently available for biomass gasification [22,24,38,44]. They may be classified in three main groups, based on the gas-solid contacting mode: fixed or moving bed, fluidized bed and entrained flow gasifiers, which are in turn subdivided into different types. In the last two cases, the biomass particles are conveyed through the

reactor by the gasifying medium, while in the fixed bed gasifiers the fuel is supported on a grate. Each kind of gasifier, however, has its own appropriate range of application: moving bed reactors are suitable for smaller units as 0.01-10 MW_{th}, while the entrained flow type is appropriate for capacity higher than 50 MW_{th}; fluidized bed gasifiers, instead, are used for intermediate units like 5-100 MW_{th}. These and characteristics proper of the different gasifiers are summarized in *Table 2.*

	Fixed/Moving Bed	***Fluidized Bed***	***Entrained Bed***
Feed size	<51 mm	<6 mm	<0.15 mm
Steam requirement	high	moderate	low
Exit gas temperature	450-650 °C	800-1000 °C	>1260 °C
Reaction zone temperature	1090 °C	800-1000 °C	1990 °C
Cold-gas efficiency	80%	89%	80%
Application	small capacities	medium-size units	large capacities
Problem areas	tar production and utilization of fines	carbon conversion	raw-gas cooling

Table 2. Comparison of some commercial gasifiers [20]

The main attraction of fixed bed gasifiers is the possibility to be built inexpensively in small size. On the contrary, they are characterized by poor mixing and heat transfer, complicating the uniformity of fuel distribution, temperature and gas composition. Two kind of fixed bed reactor are currently available: downdraft and updraft gasifier. In the former, particularly suitable for the smallest units (10 kW_{th}-1 MW_{th}), both solid fuel and gasifying medium flow from the top to the bottom of the reactor (*Figure 3.a*). The biomass is inserted from the top where is dried by means of the heat developed by other processes. Subsequently, biomass is thermal decomposed in the pyrolysis zone, where tar and charcoal are produced. In the central zone, reactor shows a restriction where the oxidizing agent (air) is inserted and suitable for tar cracking and charcoal combustion. Finally, in the gasification zone reduction and production of syngas are reached. This kind of gasifier is characterized by high biomass residence time and thus high conversion rate. Moreover, concentration of tars produced is minimized (0.015-3 g/Nm^3), thanks to the cracking in the restriction. On the contrary, the gas exit temperature is relatively high (700 °C) and the suitable biomass needs to have a low moisture wet basis. In the updraft gasifier, instead, the solid fuel is inserted from the top of the reactor and flows in the opposite sense of the gasyfing medium, generally air and steam, which is inserted from the bottom (*Figure 3.b*). Biomass is dried by hot product gas

generated in the bottom combustion and gasification zone of pyrolysis products as charcoal and tar. Even in this configuration, biomass residence time and heat velocity of the reactor are quite high, but tar content are surely higher than the previous one, being in the range of 30-150 g/Nm^3. Gas exit temperatures are lower (200-400 °C) and the moisture wet basis of biomass could be even higher than 25%.

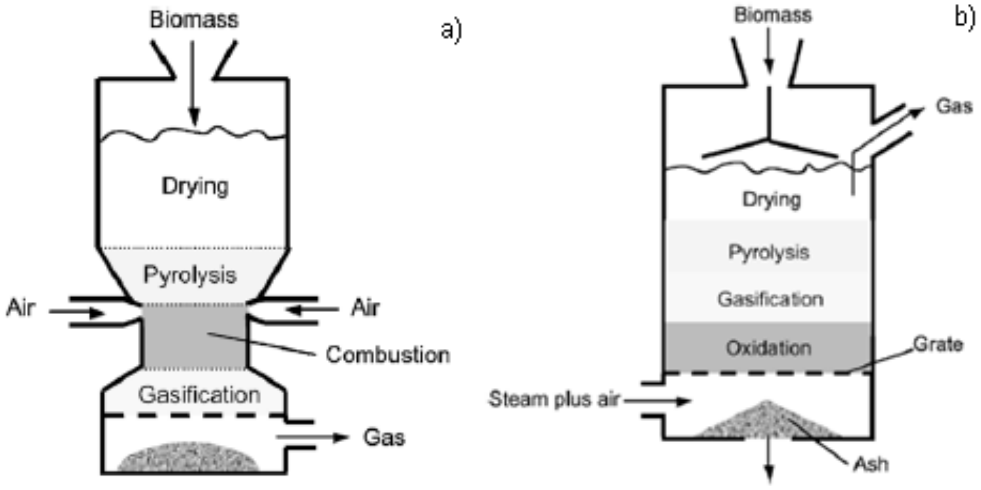

Figure 3. Downdraft (a) and updraft (b) fixed bed gasifier [20]

Entrained flow gasifiers are the best choice for large scale gasification of coal, coke and refinery residues, but not so appropriate for biomass since its large moisture content. They operate at very high temperature and with only pure oxygen or steam as medium. However, content of tars in product gas is almost absent.

The fluidized bed gasifiers are characterized by their excellent mixing and temperature uniformity. This is indeed possible for the presence of a bed of granular solid particles, named “bed materials”, kept in a semi-suspended condition, which is exactly the fluidization state, by means of the gasifying medium passage at proper velocity. The presence of the bed material provides good thermal inertia and helps to uniform distribution of fuel, temperature and conversions inside the whole reactor, improving thus the overall conversion efficiency. In some cases, this could be a catalytic compound which enhances the gasification reactions development. Solid fuel needs to feed the reactor in very small particles, in order to support the fluidization. Differently from the fixed bed gasifiers, in the fluidized ones is not possible to distinguish between all the conversion phases. Its tar

production lies between that for updraft and downdraft gasifiers, with an average value of around 10 g/Nm^3 [45]. The higher uniformity of temperature in the reactor helps to avoid ashes fusion and the very high residence time leads to lower pollutants and higher efficiency. Since these considerations, they are particularly advantageous for gasification of biomass, even if their higher technical complexity. Fluidized bed (FB) can be classified in two principal groups: bubbling (BFB) and circulating (CFB). In the former (*Figure 4.a*), the gasifying agents' velocity is around the minimum fluidization point where frictional forces between solid particles and gas are the same of particles weight, so that bubbles of reaction gas are generated, which guarantee a continuous mixing of the solid phase. It is possible to identify two zone of reaction: one dense bed at the bottom and one dilute and larger zone at the top, named freeboard. This type of reactors offers several advantages, such as a very uniform gas and temperature distribution, larger range of granulometry accepted and a better volumetric compactness. Unfortunately, syngas produced drags higher amounts of particulate and so high efficiency cleaning steps are necessaries. In the circulating fluidized bed gasifier (*Figure 4.b*), instead, the gasifying agents' velocity is high enough to drag the solid particles outside the reactor together with the product gas. A cyclone is then used for the separation and then the solid particles are re-inserted inside the reactor. In this configuration, the separation between freeboard and bed zone is less clear. There is the necessity of higher height of the reactor for maintaining same residence times of the bubbling gasifier, dimension of fuel particles very small and higher complexity of the system.

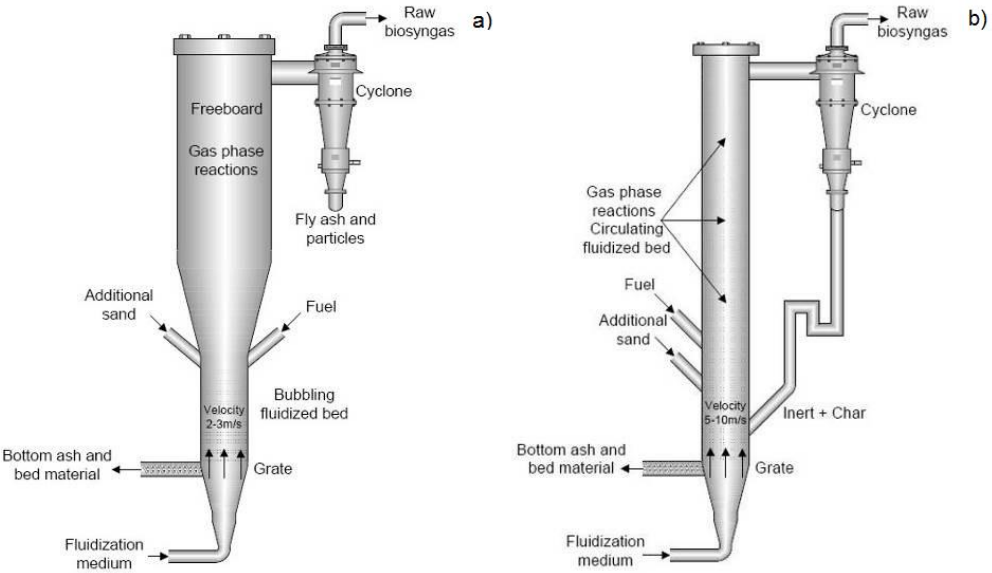

Figure 4. Bubbling (a) and circulating (b) fluidized bed gasifier [46]

Fluidized bed reactors offer the possibility to have an additional system configuration: the twin bed gasifier [47–50]. In this kind of reactor, the fluidized bed is divided in two zones or chambers, one designated for gasification and one for combustion reactions (*Figure 5.a*). Circulation of bed material between the two chambers occurs, providing the heat transport from the combustion to the gasification zone. Fuel is inserted in the gasification zone together with steam as gasifying agent: in absence of oxygen, biomass is pyrolysed and generate the desired product gas with the aim of steam, but carbon is not completely converted generating charcoal. This last one circulates to the combustion zone, where it is oxidized with air and burned, releasing heat to the bed material that re-circulates back to the gasifier providing the heat necessary for the endothermic gasification reactions. Flue gas from combustion are released outside separately and do not enter in the gasification chamber. A typical scheme of a dual fluidized bed gasifier is shown in *Figure 5.b*. Thank to this technology it is possible to obtain a very high value syngas (>15 MJ/Nm^3), since it contains only the nitrogen of the fuel and not that coming from the air, and greater H_2 content. Moreover, it is characterized by low contents of tars, since the use of steam and their burn out in the combustion zone. Since these numerous advantages, in this work attention was focused on this type of gasification reactor, specifically on a dual bubbling fluidized bed gasifier (DBFB) with a catalytic bed material of olivine sand, having the additional advantage of operating at ambient pressure, simplifying the technical complexity of the system.

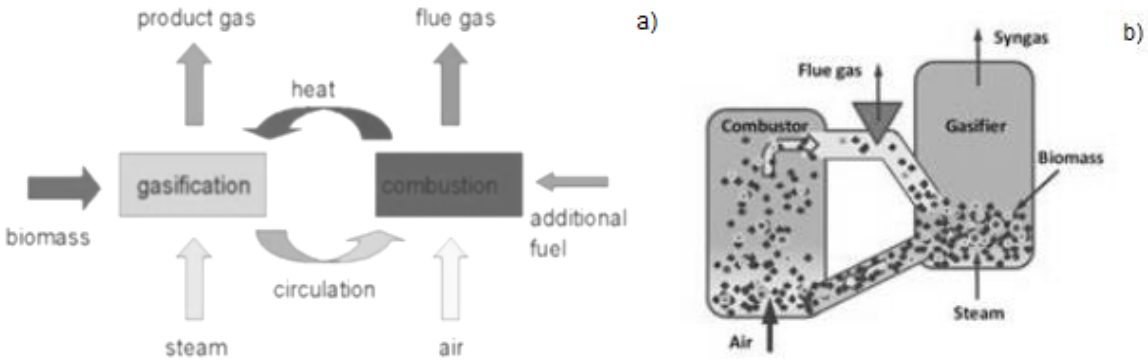

Figure 5. Process (a) and scheme (b) of a dual fluidized bed gasifier

The interest of the research field towards the dual fluidized bed gasifier is relatively recent. First studies were conducted by Battelle in 1970 [51], together with U.S. Department of Energy (DoE), which developed a wood gasification plant of 50 MW_e. Since that, several other biomass gasification plants based on twin bed fluidized bed or simple fluidized bed gasifier were developed, either in large either in small-pilot scale. *Figure 6* shows their distribution all over Europe [52]. Regarding large scale plants, they were divided in two groups: the successfully experiences (black point in *Figure 6.a*), meaning that they are operative under commercial conditions and for more than 6000 hours (or for 2000 hours per year), and other operative remarkable plants with less than 2000 hours of operation (red point in *Figure 6.a*). The only large scale based on the twin fluidized bed technology is that operative in Gussing in Austria since 2002 (number 1 in the figure). It is a CHP plant at demonstrative scale with 8 MW_{th} of capacity, using steam as gasifying agent. Thanks to this plant, the whole city is supplied with green electricity and heat from biomass [49]. The other successful plants, are all based on fixed bed gasifiers (the ones in Denmark) and simple fluidized bed reactors, bubbling or circulating. All of them use air as gasifying medium, except the plant of Varnamo in Sweden (number 25 in the figure), that is a pressurized CFB gasification plant that, after an upgrading in 2007, works also with steam or oxygen [53]. In Italy, only two large scale gasification plants are present: the one in Grevè di Chianti, a successful experience of an air fluidized gasifier with an electric power output of 6.7 MW_e [54], and the one in ENEA research centre of Trisaia, a 1 MW_{th} gasification plant based on an internal circulating bubbling fluidized bed (ICBFB) fed with steam and oxygen [55]. Regarding the small and pilot scale, around 50% of the total number of plants considered adopt a fluidized bed configuration. The gasifying agent mainly used is air or a mixture of air and steam, while the less used is pure oxygen, even if it produces a gas with higher heating value. The use of oxygen, in fact, implies its purchase, a safe storage place and safety measures to handle it. In Italy there are one small scale gasification plant [56], based on a fixed bed reactor gasified with steam, and two lab-scale gasifier, one in L'Aquila [41], fluidized bed with steam, and one in Trento [57], fixed bed with inert gas and air.

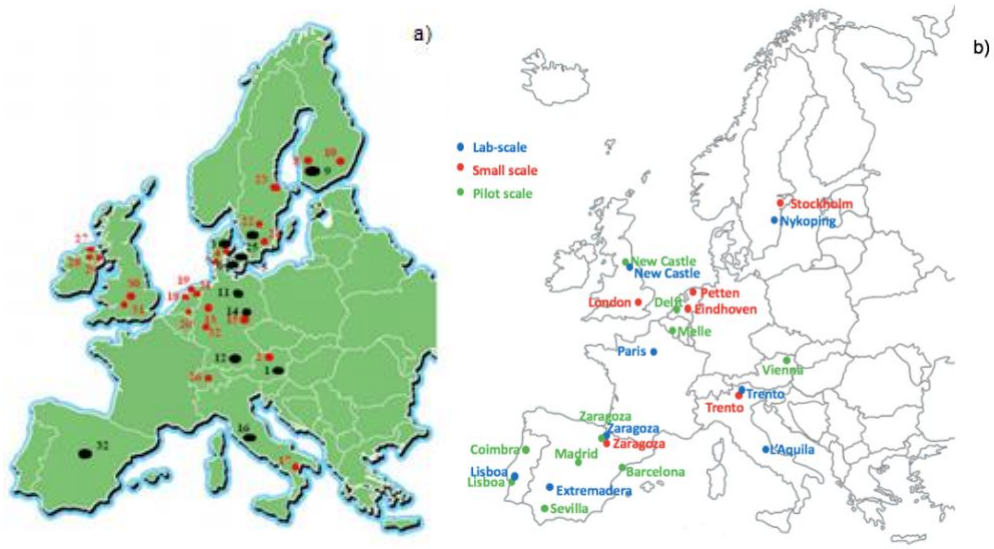

Figure 6. Operative gasification plant in Europe: (a) large scale (b) small and pilot scale [52]

Medium-large (1-50 MW_{th}) coal and biomass gasification power plants are in a more commercial stage, but these power plants can effort, owing to the size, advanced pre-processing, gasification and gas conditioning technologies. Regarding the small power plants, instead, the technology development issues still remain. Nevertheless, to really exploit the biomass energy potential, reliable, high efficiency and low environmental impacts, small scale power plants have to be developed, to follow the low energy density and perishability of this fuel. Indeed, one of the major limitations associated with the use of the large bioenergy potential (e.g. the Italian territory amounted to about 30 million metric tons/year [58,59]) is the biomass dispersion. Actually, a small biomass power plant can have annual operating hours lower than 7000, efficiency lower than 25%, high local and environmental impacts and a capital cost greater than 10.000 €/kWh_e [60].

Gas cleaning and conditioning

As previously reported, products of biomass gasification are not only composed by the producer syngas, but also by some impurities and pollutants detrimental either for environmental and human health either for downstream components. Among them, condensable tars are one of the most harmful components and their removal is necessary and essential. Tars are defined as the condensable heavier hydrocarbons generated from the pyrolysis and gasification reactions. According to the National Renewable Energy Laboratory (NREL) of the U.S. DoE, tars are all those hydrocarbons with a molecular weight

higher than that of benzene. Benzene, thus, is not considered a tar but, since it is produced in large amounts and since it can cause severe problems when condensed, it is anyway taken into account [45,61]. At ambient temperature, they are a thick, black, highly viscous liquid that can condense in the low-temperature zones of a gasifier, clogging the gas passage and leading to system disruptions. Tars are produced primarily through depolymerisation. During the pyrolysis phase, lignin, cellulose and hemicelluloses of biomass are break down and produce oxygenate condensable molecules, named as primary tars, such as acids, sugars and alcohols. Increasing the temperature (>500°C), these substances are converted in a gaseous phase and transformed in other molecules like phenols, alkenes and ethyl hydrocarbons, defined as secondary tars. Finally, at the highest process temperatures (750-850 °C) when the primary tars are completely decomposed, the secondary tars are transformed in gaseous products and other molecules, classifiable in alkyl compounds (methyl-naphthalene, toluene and indene) and polycyclic aromatic hydrocarbons (PAH, benzene, naphthalene, acenaphthylene, anthracene and pyrene). Tar production is highly undesirable, as it can create a number of problems such as condensation and subsequent plugging of downstream equipment, formation of tar aerosols and polymerization into more complex structures [62]. In *Table 3* are listed the limits of tar for the different application of the product gas. As it is possible to note, fuel cells and gas turbine involve higher restriction level respect to ICE.

	Tar (g/Nm^3)
Direct combustion	no limit specified
Syngas production	0.1
Gas turbine	0.05-5
IC engine	50-100
Pipeline transport	50-500 for compressor
Fuel cells	<1.0

Table 3. Upper limits of tars in different application [45]

Several methods for tar removal are currently available [63,64], classifiable in two groups: in-situ or primary reduction and post-gasification or secondary reduction. The formers are carried out either by adjust gasifier operating condition (gasifying agent, reactor temperature, reactor pressure, residence time, oxygen to carbon ratio) or its design, so that

tar formation is reduced, either by conversion into other products by means of catalysts addition in the bed material. The aim is to lessen generation of tar directly inside the gasifier, influencing also the product gas quality. Primary methods allow to obtain tar reduction quite high, but the complete removal is achievable only with the additional use of the secondary methods [65]. These methods are carried out downstream the gasifier and can be based on chemical or physical technology, usually at high or low temperature respectively.

Other classifications of tar removal techniques are based on their operating temperature, distinguishing between hot and cold methods. The formers avoid the cooling down of the product gas and mainly consist in tar destruction by means of catalytic and thermal actions. Other hot cleaning system are available, mainly physical such as cyclones and ceramic filter candles, but these are more appropriate for char and particulate removal. The main reactions responsible for tar destruction are wet or dry reforming, which convert tars in hydrogen and carbon monoxide with steam or CO_2 respectively, and catalytic cracking, where in presence of specific catalysts tars are decomposed producing carbon, hydrogen and lighter hydrocarbons, or thermal cracking, that is a cracking at very high temperatures (900-1200 °C) but without catalysts [66]. Reduction of the gravimetric tar mass is 78% in the case of the thermal cracking, whereas it is in the range of 77–92% in the case of the steam reforming [67]. Several catalysts are used for these purposes, such as the silicate mineral olivine, generally used as part or total of fluidized bed, alkali metals, premixed with biomass, dolomite ($MgCo_3$, $CaCo_3$), appropriate for tar removal but not that of methane, and finally nickel, optimal for tar and methane reduction [68–71]. The hot tar removal methods could be used both inside the reactor or downstream it, as primary or secondary method. The cold tar removal methods, instead, needs to be used necessarily downstream the gasifier, since they all involve the cooling down of the product gas, using materials not resistant at high temperature. Among these techniques, wet scrubbers are at the moment the most used technique in many gasification plants to remove contaminants and tars, mainly based on water [72–74]. In the scrubbing process, or gas absorption process, product gas is cooled down to 25-50 °C and the contaminants of gas stream are absorbed into an absorbent media. In order to have an efficient absorption the contaminant in the gas phase must have some solubility in the scrubbing liquid [75]. Tar is a mixture of several organic compounds having low or no water-solubility characteristics (hydrophobic substances): water is thus not

appropriate to be used as a scrubbing medium for tar removal in efficient way. Therefore, use of other kinds of absorbents, especially hydrophobic absorbents, should be more effective for tar absorption. Performance of hydrophobic absorbent as a scrubbing liquid in biomass gasification, such as water, diesel fuel, engine oil biodiesel fuel and vegetable oil, can be hardly found in open literatures [76–78]. The results showed that only 31.8% of gravimetric tar was removed by the water scrubber, whereas the highest removal of gravimetric tar was obtained by a vegetable oil scrubber with a removal efficiency of 60% while for lighter PAH efficiency was higher than 90%. These results were obtained for 100 min of operation. Further research are thus necessaries in order to evaluate performances of a such system for a longer period of operation.

In any case, the wet scrubbing technique is aimed just to remove tars from the product gas stream, without improving its energetic content, dealing with *gas cleaning* systems in this case. Thermal or catalytic steam reforming/cracking of tar at high temperature, instead, eliminate tar compounds converting these into syngas and thus recovering their energy content whilst reducing pollution: they are thus generally defined as *conditioning systems*. An effective catalyst for this scope is nickel, but further works are necessary in the medium-long period to reduce their production and management costs (deactivation, sulphur poisoning, etc.). A low cost and available catalyst would be preferable at the moment for this reason, like natural catalyst as calcined dolomite. Different works showed that calcined dolomite is an efficient and cheap natural catalyst at least to reduce tar before any further treatments [79–81].

In this work, therefore, a deep investigation on a combined gas cleaning and conditioning system is carried out, based on an exhaust vegetable oil scrubber coupled with a dolomite secondary guard bed, evaluating its tar removal efficiency for several hours of operation (chapter 3). However, a such tar removal apparatus is suitable for further application of product gas in system like ICE, since the cooling down of product gas is required and the conventional gas inlet temperature in an ICE is surely lower than 100 °C. For other gasification application, instead, such as production of pure hydrogen, hot gas cleaning and conditioning methods are more appropriate, particularly catalytic cracking and steam reforming of low and high molecular weight hydrocarbons, mostly based on nickel catalysts, since they offer several advantages such as thermal integration with gasification reactor, high tar conversion and hydrogen rich syngas production [82–86]. This was confirmed also

by the results of the UNIQUE concept [87], which integrates both the fluidized bed and the hot gas cleaning system into a single and compact gasifier. It has been possible by virtue of a bundle of ceramic filter candles operating at high temperature directly in the gasifier freeboard, producing a syngas free of tars and allowing remarkable plant simplifications and reduction of costs [87–89]. This technology was taken into account in the global simulation of a biomass gasification plant for hydrogen production reported in chapter 3.

2. Flow and Sensors

Background

Reliability and efficiency of biomass gasification systems are extremely dependent by product gas quality and purity in the various gas streams. The numerous devices downstream the gasifier, indeed, are highly affected by product gas composition and contaminant content. These characteristics can several damage their operation, besides influencing the overall performances of the system and even its environmental impact. The continuous monitoring of syngas composition and trace contaminants is thus evidently crucial in biomass gasification systems, either for health, optimization and efficiency of components and overall system either for environmental and safety considerations. There is the necessity of an adequate process control system based on on-line and real time measurements of the gas flows, in order to quickly detect variations in composition and, thanks to suitable control apparatus, simultaneously adjust the system operating conditions, as recognized even by the US Department of Energy [90].

Conventional measurement systems, such as chromatography and mass spectrometry, are not appropriate for these purposes, since they require gas extraction and preconditioning (cooling, dehumidification, depressurisation...) before the analysis, involving possible gas alteration and significant time lag. In addition, these devices still suffer from miniaturization problems and are often very expensive instrumentations. Even if highly reliable and sensitive, they are not able to provide continuous and real time measurements [13,14]. On the other hand, gas-sensing devices allow fast, direct and in-situ monitoring and are characterized by small size and low cost, due to their simplicity in design, fabrication and function. Moreover, since their output consists in electrical resistance values, they are extremely suitable for coupling with control circuits [91–93]. In addition, using chemoresistive gas sensors based on perovskite oxides, the additional advantage of high temperature operating arises, allowing measurements directly on gas streams. Since these numerous advantages, they are always more under the attention of the scientific research field and they are gradually substituting the conventional analytic methods, also thanks to the miniaturization and technology progresses. Nevertheless, much micro gas-sensing equipment have not yet reached a commercial stage, even less in the

application field of the biomass gasification systems: more studies are then needed on suitable materials with the required and proper characteristic.

Gas sensors can have different applications in biomass gasification systems and the relative coupled devices for heat or electricity production. First of all, in dual fluidized bed gasifiers, the combustor operates at temperatures of 900-1050 °C and the flue gas composition needs to be measured and controlled, both for environmental and energy optimization reasons [94]: CO emissions, in fact, are limited from national and international normative and the limits for a biomass combustion system are around 100-400 ppm depending on various parameters, like the size of the plant [95,96]. In addition, it is useful to measure hydrogen content in the flue gas in order to evaluate presence of some unburned hydrocarbons and, thus, the combustion efficiency. On the other side, syngas from the gasifier (at 700-900 °C) is mainly composed by H_2, CO, CH_4 and CO_2 and by some organic (tar) and inorganic contaminants (H_2S, HCl, NH_3), as showed in the previous chapter. Syngas composition is a crucial parameter for the system efficiency, since it highly affects the gas quality and its heating value: it is evident the importance to monitor continuously the syngas produced. Moreover, in the case of usage of syngas from a biomass conversion process in an internal combustion engine, could be useful to measure carbon monoxide and hydrogen contents in its flue gas, for the same reasons previously reported for the combustor. On the contrary, in the case of a biomass gasification system for hydrogen production to be fed an integrated fuel cell system, limits on syngas quality are even stricter. The coupling of biomass gasification systems with fuel cells, indeed, is effectively advantageous, since it can provide higher electrical efficiency and negligible emissions in comparison with the conventional ICE [97–99]. Furthermore, the gasification systems well thermal integrate with the high temperature fuel cells (such as SOFC-Solid Oxide Fuel Cells and MCFC-Molten Carbonate Fuel Cells). Nevertheless, FC present lower tolerance thresholds than ICE on detrimental trace elements compounds, like sulphur compounds [100–102]. The cleaning and purification of the syngas produced and the composition control of the various streams are thus essential to avoid damages to the various system components and to reduce the environmental impact. In particular, in this case is fundamental the presence of secondary fixed bed reactors of catalysts properly developed for the water gas shift (WGS) reaction, in order to increase the hydrogen content by means

of the carbon monoxide presents in the syngas. Low temperature water gas shift reactors work at an operating temperature around 300 °C and accept only low concentration of H_2S, otherwise the copper catalysts of WGS reactor will deactivate after the irreversible reaction with sulphur. For this reason, a sulphur guard bed based on ZnO is necessary before the WGS reactor, in order to reduce the hydrogen sulphide content in the syngas below 1 ppm, and the measuring and control of H_2S content in the syngas entering in the WGS reactor is extremely important for its preservation [103–105]. It is important also to measure the content of carbon monoxide at WGS reactor exit, in order to evaluate its efficient operation. Fuel cells can be then directly fed by the conditioned and hydrogen rich syngas produced or by pure hydrogen proper separated from product gas. Using a low temperature fuel cell like PEMFC (Proton Exchange Membrane Fuel Cell), H_2S needs to be completely removed from the syngas, while CO content has to be lower than 10 ppm. Using high temperature fuel cells, instead, no limitations are required for carbon monoxide, while the limits on the H_2S content are around 0.5-1 ppm [106–109]. Monitoring of syngas composition is thus necessary for the preservation of the FC. Moreover, for a system safety operation, is also extremely important to measure possible H_2 leakages, considering that the lower flammable limit of hydrogen is around 4%$_{vol}$ [110–112]. A scheme of the crucial application of gas sensors devices in biomass gasification systems is reported in *Figure 7*.

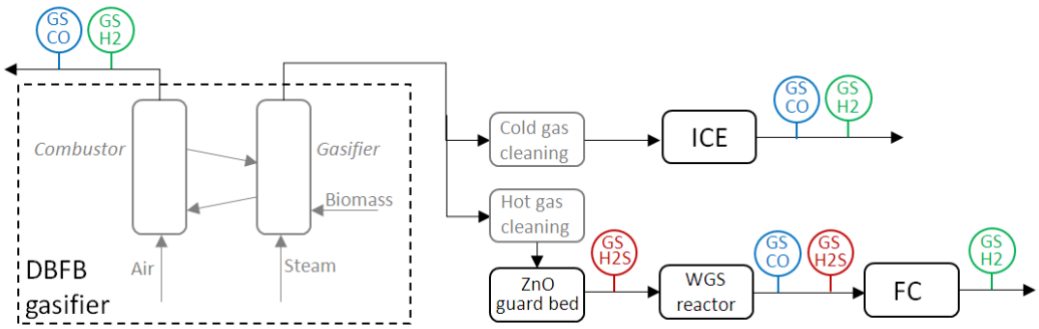

Figure 7. Crucial role of gas sensors in biomass gasification technology

Gas sensors

According to the International Union of Pure and Applied Chemistry (IUPAC) *"a chemical sensor is a device that transforms chemical information, ranging from the concentration of a specific sample component to total composition analysis, into an analytically useful signal. The chemical information, mentioned above, may originate from a chemical reaction of the*

analyte or from a physical property of the system investigated" [113]. A sensor is, hence, constituted by two principal components: a *receptor*, sensitive to the unit to be measured, defined also as the exact sensor, which recognizes the input information and transforms it into an energy form measurable by the second component, the *transducer*, which converts this energy into a useful, typically electrical, analytical signal.

Sensors can be classified according to a number of different rules, based on the operating principle of the receptor or the transducer. Regarding the first classification, it is possible to distinguish between [113,114]:

- physical sensors, where the measure results by a physical process like mass, absorbance, refractive index, temperature, or conductivity change;
- chemical sensors, which are based on the chemical reaction that take place between analyte's molecules and the receptor;
- biochemical sensors, which are a subclass of the previous ones, but with a biochemical reaction, e.g. microbial potentiometric sensors or immune-sensors.

This classification, however, it is not always clear, since the discrimination between chemical and physical sensors is not always possible, as in the case of a gas sensor where the response signal is a consequence of a gas adsorption. For these reasons, the classification based on the transducer is sometimes preferable. An exhaustive summary about this is reported in *Table 4* [115–118]. Other typical classification can be based on type of sensing material used (metal-oxide, polymeric and inorganic), fabrication technology (screen-printed and vapour deposited), field of application and some others.

Transducer	***Measured properties***	***Source of signal***
Optic	Absorbance	Analyte itself or due to reaction with certain indicator
	Fluorescence	Changes in fluorescence properties
	Luminescence	Emission caused by chemical reaction
	Refractive index	For example caused by change in solution composition
	Scattering	Caused by particles of definite size present in the sample

Electrochemical	Voltammetric	Change of current is measured
	Potentiometric	Change of electrode potential is measured against a reference electrode
Electrical	Resistive	Change of resistivity dependent on analyte's amount adsorbed
Mass	Piezoelectric	Changes of resonant frequency of quartz oscillator plate due to adsorption of analyte on its chemically modified surface
	Acoustic wave	Changes of propagation velocity of acoustic wave
Magnetic	Paramagnetic	For example, oxygen monitors
Thermometric	Heat effects	Changes of temperature due to heat effects of reaction or adsorption

Table 4. Classification of chemical sensors by transducer operating principle

The application of gas sensors is widespread in numerous sectors, from the automotive to the environmental, and also in the food and health areas [119–121]. In particular, in the automotive they are used for filter and ventilation control, besides the alcohol tests and gasoline vapour detection. In the food and industrial sector, sensors are useful for quality and process control, while in medicine they are able to carry out the breath analysis and disease detection. One of the most important applications of chemical sensors is in the environmental control, placed in the weather and pollution monitoring station. Also the safety application is very crucial, where sensors are able to detect fire and leaks, besides toxic and flammable gas. In any case, the most important application fields for gas sensors are those of combustion control and environmental pollutants monitoring, showing the two crucial function of a chemical sensor: the gas concentration reception and the information sending to the control system. It is important to stress here that there are two kind of configuration for gas sensors: the *single gas sensors*, used for the detection of only one analyte, such as fire and leakages detector or the alarm devices warning the overcoming of threshold concentration values of hazardous gases in the work places, and multisensor systems, note also as *electronic nose*. These devices are composed by several sensors, each of them sensitive to a certain chemical specie; they are typically used for the Volatile

Organic Compounds (VOCs) detection or for odours recognition from foods and indoor air [122–124].

For the evaluation of gas sensor performances, it is necessary to refer to specific factors which allow to totally characterize the component. The most important parameters are those named as *3S* [125,126]:

- *Sensitivity*: the measured signal variation per analyte concentration unit; it corresponds to the slope of a calibration curve;
- *Selectivity*: the ability of the sensor to detect changes of a specific or more analytes;
- *Stability*: the ability to maintain their performances and characteristics during the time e for high temperatures, in order to permit the reproducibility of the measures.

In addition to these, other characteristics typical of all measurement instruments are:

- detection limit: the minimum analyte's concentration that can be measured by the sensor under given conditions, especially at a specific temperature;
- linearity: the relative deviation of a certain calibration curve from an ideal straight line;
- resolution: the lowest concentration difference that can be distinguished by the sensor;
- response time: time requested by the sensor to respond to a variation from the zero to a certain concentration level;
- recovery time: time requested by the sensor to return to its initial value after the variation;
- working temperature: temperature at which the sensor shows its maximum sensitivity;
- hysteresis: maximum difference in output signal when the value is approached with an increasing and a decreasing analyte concentration range.
- dynamic range: analyte's concentration range between detection limit and highest limiting concentration;
- life cycle: period in which sensor can operate continuously.

These parameters allow to enough characterize a specific device. An ideal chemical sensor should have high sensitivity, selectivity and stability, low detection limit, hysteresis and response time, good linearity and life cycle long as much as possible [115]. A sensor with all of these characteristic is, besides very difficult, quite worthless. Indeed, it has always to be considered the application of a determined gas sensor, since that not all of these conditions simultaneously need to be verified. In *Table 5* a schematic comparison of different gas sensors is proposed [127].

Parameters	***Resistive***	***Electrochemical***	***Thermal conductive***	***Optic***
Sensitivity	e	g	b	e
Selectivity	p	g	b	e
Stability	g	b	g	g
Accuracy	g	g	g	e
Response time	e	p	g	p
Life cycle	g	p	g	e
Maintenance	e	g	g	p
Cost	e	g	g	p
Portable device	e	p	g	b

Table 5. Comparison of different gas sensors (e: excellent; g: good; p: poor; b: bad) [127]

As it is possible to note from *Table 5*, resistive (or conductometric) sensors, mainly based on semiconductor metal oxides (MOS), are one of the most promising type, since their numerous qualities. In fact, they provide very high sensitivity and optimal response time, besides long life time and elevated simplicity in function and fabrication, which leads to low cost of production and maintenance. In addition, their possibility to integrate in the same device both the sensing element and the signal converter for electronic control allows to extremely simplify their design. These several qualities and attractions of resistive sensors demonstrate their advantageous application in various fields. In addition, if based on chemical material particularly suitable for high temperature application, such as perovskites oxide, they offer the additional possibility to operate at high temperature. All these features highlight the great opportunity of their application in biomass gasification systems. Nevertheless, resistive sensors are characterized also by leaks of selectivity, instability (especially in the long periods) and low reproducibility. These drawbacks can be overcome by means of thermal treatment or catalysts addition or coupling with filters or chromatograph columns for selectivity improvement and mostly through carrying out research activities in the field.

Analysing also the commercial gas sensors attractiveness, it is highlighted the increasingly development of this kind of device in global market and research. The work of Gopel et al. [128] showed that gas sensors market is increasing since 1993, reaching a value of 542 M$ in the 1998. More recent reports [129,130], moreover, estimated a value of 1700 M$ in 2012, so that in 14 years market has become more than three times larger, with a linear trend from 1988 to 2012 having a slope of +89.6 M$/year. *Figure 8* shows the distribution of gas sensors market relative to 2012, classifying by gas sensor type and world spreading, calculated by overlapping data from different sources [129–131]. Among the global sensor market, biosensors and chemical sensors covered about 13 B$, being the 21% of the global market. Chemical sensors, then, represented the 13% of this part and sensors based on MOS were 221 M$ in 2012 (1% of chemical sensors). Finally, in 2012 market of gas sensors was mainly present in Europe, Asia and North-America, with 29%, 29% and 27% respectively. These data highlight the crucial role of chemical sensors all over the world, representing a widespread and increasing technology in the global market of measurement instruments. In addition, influence of MOS chemical sensors seems to be here very low, being only 1% of all chemical sensors, since this analysis focused on already marketable devices; considering, instead, also patents and researches on MOS sensors, it is evident that they are one of the most attractive technology for sensing purposes. Patents on MOS in 2012, in fact, were 26% of total ones on gas sensors, with an increasing trend in the next years; total research works in the same year all over the world were 312 and 499 in 2016, showing the increasing interest in the field (data extrapolated by Scopus and Web of Science).

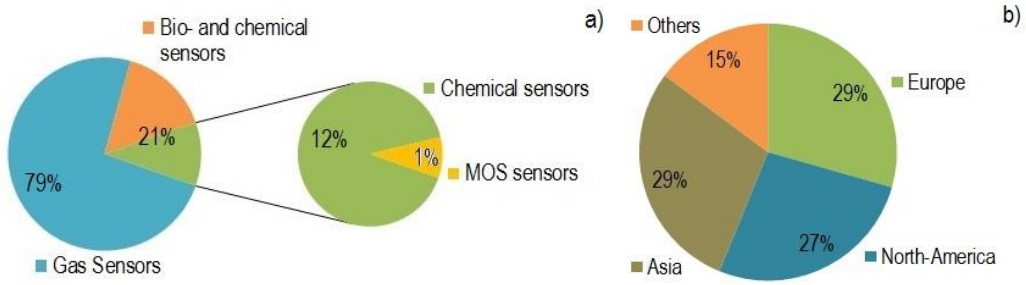

Figure 8. Typology (a) and world (b) distribution of gas sensors market

Chemoresistive gas sensors

Chemoresistive gas sensors are one of the most attractive type of electrical sensors. These devices operate due to a surface interaction with target gas and cover a large group of gas sensors: polymer, metal, metal oxide, or semiconductor conductometric sensors, capacitance sensors, work–function-type and Schottky barrier-, MOS-, and FET-based sensors [132]. Chemoresistive sensors are in the group of conductometric (or resistive) sensors and are characterized by a simple structure and an operating principle based on the modulation of their electrical conductivity by the presence or absence of some chemical species that comes in contact with the device [133]. In particular, in presence of specific compounds the conductometric sensors changes its resistance as an effect of reactions (adsorption, chemical reactions, diffusion, catalysis, swelling) that take place on the surface or in the bulk of the sensing material. The electrical conductivity is then modulated by the chemical species and these variations can be measured as changes in the current.

The basic scheme of a chemoresistive sensor is constituted by different components [134,135]:

- layer of sensing material, deposited as compressed powders or thick or thin film;
- substrate, for the sensing layer deposition;
- electrodes, for electric characteristics measuring;
- heater, for the independent device heating and operation at its optimal temperature: it is generally separated from the sensing material and electrodes by means of an insulator layer.

A graphical representation of such a configuration is reported in *Figure 9.a*, where a scheme of the Taguchi sensor is presented, since it is the first resistive sensor produced, exact by Taguchi around the end of 60s of the last century, and the most representative one. The current chemical resistive sensors can have some structural differences, such as a plane alumina support with interdigitated gold sensing electrodes, that maximize electrical responses, on which a thin film of sensing material is sprinkled, as it is possible to see in *Figure 9.b*. In the case of their usage in gasification systems, then, it is possible to operate without the heater, if the sensor is installed in gas streams with temperatures equal to those characterizing the operating condition of the measurement device.

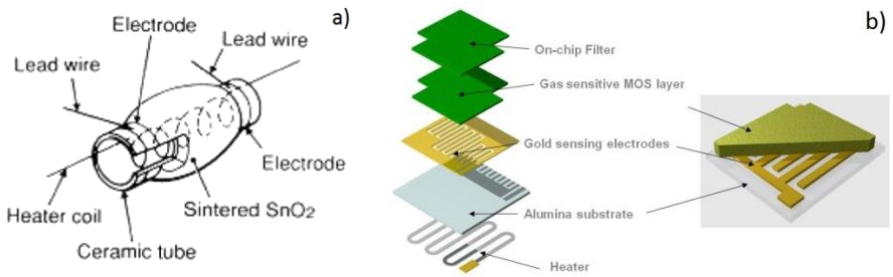

Figure 9. Chemical sensor structure: a)Taguchi sensor [136] *b)current configuration* [137]

Sensing layer of resistive sensors could be constituted by different kind of materials: organic, such as polymers, porphyrins and phthalocyanines, or inorganic. These latter are the most widely used, since their higher stability [138]. Among them, *metal oxides semiconductors* (MOS) are a very attractive solution as gas sensors receptors [139]. They are, in fact, very economic materials, even thanks to the possibility to be produced by a number of different simple methods. Moreover, they have an elevate thermal and temporal stability and can provide very advantageous sensing properties [140–145]. Semiconductivity of the materials is highly dependent on its electronic band structure. In every crystalline material, indeed, electrons are able to occupy only determined bands, defined as a range of allowed or prohibited energies to an electron. Three different bands are then possible [137,146]:

- valence band (E_v), the highest energy band totally filled with electrons;
- conduction band (E_c), the lowest normally empty energy band where electrons are free to move;
- band gap (E_g), the energy range between the other two bands where no electron states can exist due to the quantization of energy.

In addition, it should be considered the Fermi energy, E_f, referring to the energy for which an allowed level at that energy has an equal chance of being found occupied or empty by electrons. Materials, thus, can be classified by the wideness of band gap and the Fermi energy's position (*Figure 10*): conductors have no band gap and the energy level is inside one band; insulators have a wide band gap with the Fermi energy in its centre; semiconductors, finally, have intermediate conditions of small band gap and Fermi energy anyway placed in its centre, but with a higher probability for electrons to pass in the conduction band.

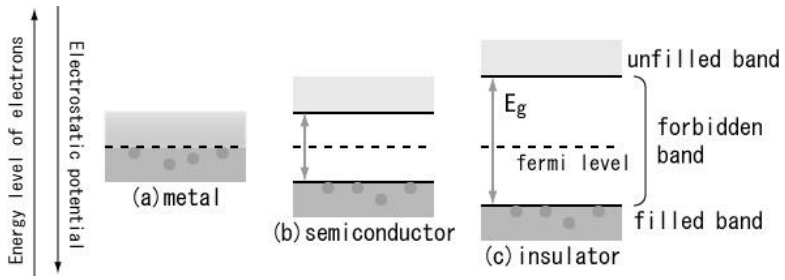

Figure 10. Energy bands and Fermi energy

Semiconductors, then, can be n-type or p-type: the former has donor impurities in the crystal structure, namely impurities that provide additional free electrons to the semiconductor, which tend to occupy the conduction band and can conduct electricity under the application of an electric field (the majority charge carriers are electrons); the latter, instead, has acceptor impurities that can generate unsatisfied chemical bonds naturally fulfilled by valence band electrons, which in turn create “holes” in the valence band (conduction is regulated by positive holes being the majority charge carriers).

Several semiconductors metal oxides have been considered suitable for application in chemoresistive sensors, both simple and mixed oxides, and in different structural phases, such as amorphous, nanocrystalline, poli-crystalline and the mono-dimensional crystalline. Each phase has its unique characteristics which can influence, positively or negatively, sensors performances [147–152]. Nano- and poli-crystalline materials are the best and the most used, thanks to their optimal combination of all critical properties of sensing applications: high specific surface area, due to the small dimensions of crystallites, economic technologic design and structural and electrical stability. Amorphous materials, instead, have very low stability, especially at high temperatures. Mono-dimensional crystalline materials, finally, have the maximum chemical properties but they require high costs and a complex fabrication technology. In addition, it is difficult to reproduce uniform mono-dimensional structures, influencing also reproducibility of gas sensors responses. Since these drawbacks, they are not yet ready for their large utilization, while nano- and poli-crystalline materials will be the preferable ones for gas sensors application.

Working principle of chemoresistive gas sensors is founded on conductivity changes in the semiconductor sensing material due to chemical interactions with target gas to be

detected [134,153]. There are different possible reactions at the basis of these interactions, even dependent on operating temperatures:

- bulk reactions, which involve stoichiometric changes or conversion of the material in a different compound, generally at high temperatures;
- gas adsorption (physical or chemical) on the semiconductor surface, causing fast conductivity changes, generally at lower temperatures.

Since gas adsorption reaction on the surface is faster than the other ones, is preferable to have materials with very high specific surface area, in order to enhance sensors performances: is also for this that nanomaterials are the best choice for sensing purposes. The exact fundamental mechanisms that cause a gas response are still controversial, but can be summarized as follow [153–157], limiting our discussion to surface adsorption reactions as main effects [158]. On the surface of the semiconductor oxide, will be established reaction with gas donors of electrons, such as reducing agents as hydrogen, or gas acceptor of electrons, such as oxidizing agents as oxygen, and electrons exchange with the material occur, generating a charged layer, so called space-charge layer, close to the surface. Donor gases will give electrons to this surface layer; on the contrary, acceptor gases will extract gases from the surface. In the first case, the space-charge layer will be an "accumulation layer", that is a layer with an excess of charge carriers; in the second case, instead, a "depletion layer" will occur, namely an insulating layer where no charge carriers are present but only ionized donor or acceptor impurities: changing surface concentration of donors/acceptors also resistivity of the charged surface layer is changed. The materials developed in this work were prepared in atmospheric conditions, under the exposure of air and, thus, oxygen during its synthesis and calcination. Therefore, it is considered now the case of an acceptor gases and thus an oxidizing gas as oxygen, in particular a n-type semiconductor: during the preparation of the materials, O_2 molecules are adsorbed on the surface of metal oxides and would extract electrons from the conduction band and trap the electrons at the surface in the form of ions, leading to a band bending and an electron-depleted region, whose thickness is the length of band bending region (λ_{air}). The result will be a decrease of the free charge carriers' concentration (electrons). A schematic representation of this is reported in *Figure 11.a*. Considering here for simplicity one-dimensional metal oxides, namely metal oxides with depletion layer thickness very smaller than grain size ($\lambda_{air} << D_g$), these phenomena will happen on the surface of each single grain

of the material. Conduction of charge carriers in gas sensors, hence, occurs between the two sensor electrodes and the numerous semiconductor material's grains constituent the sensing layer. Between grains there will be an electrical barrier, so called Schottky barrier, exactly composed by depletion layers of each grain surface, as it possible to observe in *Figure 11.b*: charge carriers have to overcome this electrical barrier in order to conduct current inside the material. After the exposure for example to a reducing gas, such as carbon monoxide or hydrogen, of the sensing material so structured, it is oxidized by O^- and releases electrons to the bulk of the material. This causes the decreasing of surface oxygen ions and also the reduction of the space-charge layer thickness: the Schottky barrier between two grains is thus lowered and conduction of charge carriers between them is obviously enhanced (while resistance is reduced). The case here presented, was specific for a n-type semiconductor. In the case of a p-type material, free charge carriers are holes and not electrons and change in conductivity will be the opposite: an increase of the free charge carriers' concentration (holes) will occur in the chemisorption of oxygen ions during the preparation of the material, while a reduction of conductivity (and so an increase of resistance) will be generated after the exposure to a reducing gas. In any case, since these phenomena, conductivity (or resistance) of materials is changed after being in contact with target gases.

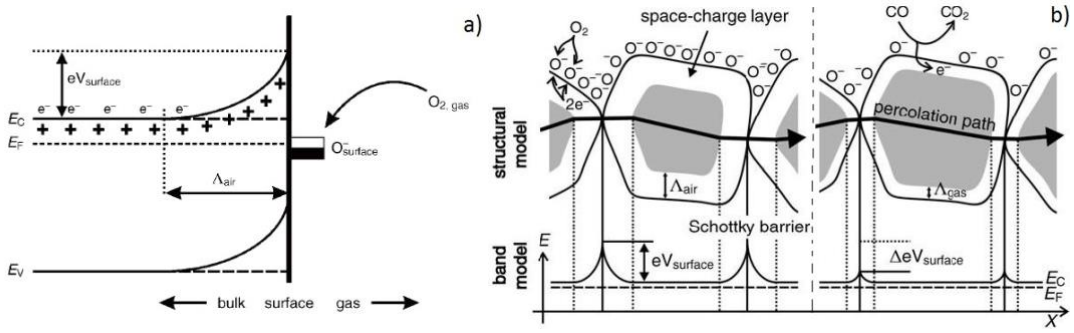

Figure 11. (a) Schematic diagram of band bending after chemisorption of charged species (b) Band and structural models of conductive mechanism before and after the exposure to a reducing gas [155]

Equivalent electrical model consists in a series of resistors, one for each grain, resulting from the parallel connection between the resistance of the surface space-charge layer and that of the bulk material. Conductance of the complete materials, then, is defined as

$$G = G_0 exp\left(\frac{-qV_s}{kT}\right)$$

where G_0 is a constant taking into account all other less sensitive factors, qV_s is the energy of Schottky barrier, k the Boltzmann constant and T is the temperature. Grains dimension highly influences conductivity of sensing materials, since the crucial role of Schottky barrier in conduction of charge carriers: sensors response increases with grains diameter decreasing, since thickness of barrier tends to disappear. This confirms what said previously about the importance to have nanomaterials in order to enhance sensors performances.

Since having deeply discussed functional principle of chemoresistive gas sensors based on semiconductor metal oxides, it is easier to individuate also some possible techniques for the improvement of their complete operation, trying to limit also the drawbacks correlated to them, such as lack of selectivity, reproducibility and stability [134]. Concerning the improvement of sensitivity, it could be achieved by means of dispersion on oxides surface or inside its volume a low concentration of additives, by doping. This method can lead to new electrons donors or acceptors formation or can influence growth and dimension of crystalline grains. Possible elements used for doping are a very large number. This technique can be useful also for the improvement of selectivity of the materials, preparing compounds specifically sensitive to one target gas and almost indifferent to other gases present in the mixture. However, this is a very difficult goal to be achieved. A different approach, then, can be the preparation of an array of different sensors sensitive to different analytes, such as the electronic noses. Finally, nanostructured metal oxides generally suffer of degradation due to their large reactivity. Different methods are available for increasing their stability: calcination, annealing, lower operating temperature. Nevertheless, the most promising solutions are the doping of metal oxides with metal particles or the use of mixed oxides. It is for these reasons that in this work the attention was focused on mixed oxides perovskite type and their possible doping for the enhancement of sensing properties.

Perovskites

Among semiconductor metal oxides, particular attention is addressed to perovskites [159–165]. The first perovskite discovered was $CaTiO_3$, whose name was used as general to indicate that group of compounds. They are mixed metal oxides with general formula ABO_3,

where A and B are metal cations with the particular requirement that A needs to be the larger cation. Hence, A cation can be an alkaline earth metal, an alkaline ion or a rare earth metal; B cation, instead, should be a transition metal. In this structure, A cations have 12 coordination with oxygen atoms while the smaller cations B have 6 coordination with oxygen anions. *Figure 12* depicts the corner sharing octahedra that form the skeleton of the structure, in which the centre position is occupied by the A cation. Alternatively, this structure can be viewed with the B cation placed in the centre of the octahedron and the A cation is in the centre of the cube. Perovskite structure is, thus, a superstructure with a ReO_3-type framework formed by the introduction of A cations into the BO_6 octahedra [166].

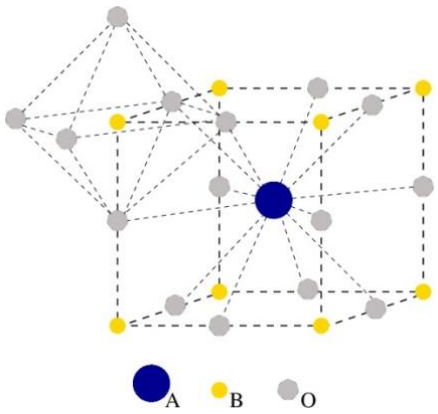

Figure 12. Crystalline structure of a perovskite [167]

Perovskite structure needs also ionic radii requirements to exist in oxides, considering the Goldschmidt tolerance factor [168]:

$$t = \frac{r_A + r_O}{\sqrt{2}(r_B + r_O)} \qquad \textbf{(2.1)}$$

The lower limits for cationic radii are r_A>0.09 nm and r_B>0.051 nm in the case of oxides. Perovskite structure, then, exist only with tolerance factor in the range of 0.75<*t*<1.0. The most recurring cases have *t* between 0.8 and 0.9, while the ideal perovskite structure occurs with *t* very close to 1 and at high temperatures and it is cubic. In all the other cases, distorted structures appear, with orthorhombic, rhombohedral, tetragonal, monoclinic and triclinic symmetries, where the first three type are frequent.

The main attractive of perovskite oxides is their flexibility and ample diversity of properties that they report, thanks to the possibility to use over than 90% of natural metallic

elements of the periodic table for their preparation, being these very stable in a perovskite oxide structure. In addition, the possibility to prepare several multicomponent perovskites by means of partial substitution of cations in positions A and B, leading to compounds of formula $(A_xA'_{1-x})(B_yB'_{1-y})O_3$, is very advantageous. These characteristics account for the variety of reactions in which they are used as catalysts. Adding to this the remarkable thermal, chemical, structural and morphological stability which characterizes them, it is evident their crucial role in all chemical devices. Use of perovskite in chemoresistive gas sensors is widely applied [169–172]. In the cases of purposes of this work, moreover, their usage is extremely important, since perovskites can allow to operate sensors at relatively high temperatures, typical of biomass gasification systems, exactly the application scope of this work.

A number of methods are used in the synthesis of perovskites, highly influencing textural, structural and morphological characteristics of these oxides [173–176]. In particular, applications of perovskites in the field of catalysts and sensing element require solids with a pretty porous network and high volume ratio and with nanodimensional grains, as previously discussed. It is possible to distinguish between two groups of synthesis methods: those based on solid-solid reaction and those based on liquid-solid reactions. The former generally generate perovskites with small surface area, due to high temperatures involved that promote sintering processes. Methods based on liquid-solid reaction, instead, are developed in order to synthesize homogeneous perovskites of pure single-phase with nanostructured crystallites and high specific surface area, and so are the preferable ones. In this work, nanopowders of perovskite oxides for sensing purposes are prepared by means of auto-combustion synthesis technique, which is based on liquid-solid reactions and have the additional advantage of being a simple, fast and efficient method, involving relatively low temperatures.

Besides the ionic radii requirements, another condition to be fulfilled in perovskites is electroneutrality, namely the sum of charges of A and B equals the total charge of oxygen anions. Appropriate charge distribution is then necessary in perovskites structure, such as $A^{1+}B^{5+}O_3$, $A^{2+}B^{4+}O_3$ or $A^{3+}B^{3+}O_3$. A suitable perovskite oxide, hence, is the lanthanum ferrite oxide, which has attracted considerable attention thanks to its great electrochemical properties, such as high ionic and electronic conductivity, and since its being economic and

not health dangerous material. These characteristics promoted its widespread utilization in many advanced technologies like SOFC (Solid Oxide Fuel Cell), oxygen membranes, catalysts and chemical gas sensors [177–181]. In addition, CO adsorption on $LaBO_3$ perovskites at ambient temperature is assumed to be dependent on the electron configuration of B^{3+} cation and Fe^{3+} cation resulted to generate the maximum carbon monoxide adsorption [182,183]. However, partial substitution of A and/or B cations is highly encouraged since it increases the oxygen non-stoichiometry and thus the electrical and magnetic properties [159,184]. In addition, gas sensing performances of $LaBO_3$ perovskites are strongly influenced by the B-site cation, which directly implicates morphological, structural, chemical and electronic properties [185–188]. On the other side, titanium perovskites exhibit high thermal stability in reducing atmosphere and at high temperatures [160,189,190]. However, very few studies deals with B-site substitution with Ti ions: Phokha et al. [191] evaluated magnetic properties of $LaTi_xFe_{1-x}O_3$ but have not analysed its sensing performances and characteristics. In addition, cobalt ions are supposed to create very active sites for reducing gas interaction [159,160] and could be useful to evaluate the different influence of divalent ions (Co^{2+}) and tetravalent ions (Ti^{4+}). Since this, in this work has been carried out an evaluation of Ti-dopant and Co-dopant influences on $LaFeO_3$ perovskite performances in the sensing of typical gases and contaminants of fuel cells and gasification systems.

3. Experimental Activity on Biomass Gasification

Several biomass gasification systems are commercially available or under development, characterized by different working principles and different scopes, as showed in chapter 1. Different configurations may be characterized by different biomasses, flows, compositions, and contaminants of the gas and even different performances and technical requirements of the system. In order to have an extended knowledge of the gasification systems and their components, operating parameters and gas flows, experimental activities on biomass gasification systems at different scale and for different configuration have been carried out. In particular, a bench-scale and an innovative 100 kW_{th} Dual Bubbling Fluidized Bed (DBFB) pilot gasifier were studied, analysing the different outputs, processes and possible innovative gas cleaning and conditioning devices. Finally, a global simulation of a complete 1 MW_{th} power plant was also performed by means of a simulation study with ChemCAD® software, to evaluate the integration of the innovative DBFB gasifier in a real application and to identify which are the streams and their main features (in term of composition and operating conditions) where apply the sensor investigations (see chapter 2).

Experimental gasification systems

First gasification tests have been carried out on a bench-scale system, since the easier and better control and management, which allow to simplify and speed up the experimental campaign. This system was used to perform simple biomass gasification tests and experimental study on tar removal devices. The test-rig used is showed in *Figure 13*.

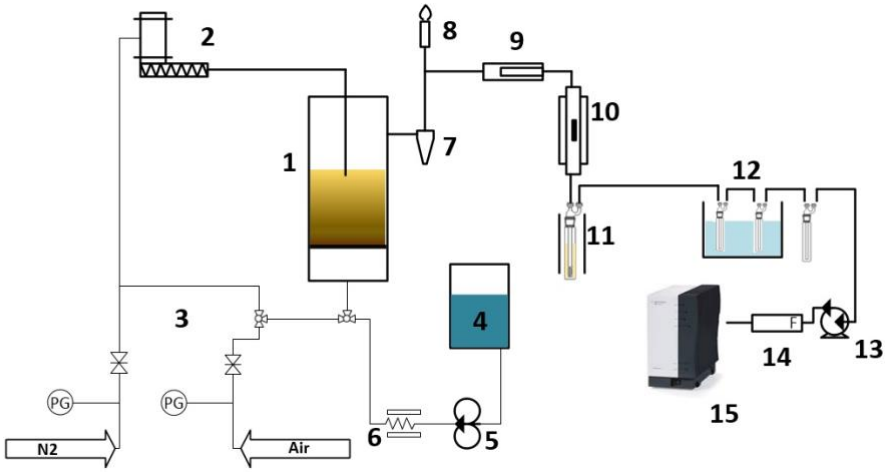

Figure 13. Scheme of the bench-scale gasification system

The fuel gas production is ensured by the cylindrical bubbling fluidized bed (BFB) gasifier, continuously fed with fuel (biomass) and gasification agents. The fluidized bed gasifier (*1*) consists of an austenitic stainless steel (AISI 310) cylindrical vessel of 80 mm internal diameter and 860 mm height. It contains a sintered stainless steel (AISI 310) porous distribution plate, which provides pressure drops higher than 40% of those through the fluidized bed yet at ambient temperature: this characteristic and the reactor design guarantee a uniform gas distribution at every temperature. The bed inventory of the gasifier was olivine sand with Sauter diameter of 350 μm and a density of 3300 kg/m^3. The whole reactor is heated by a cylindrical electric furnace, equipped with two thermocouples, one immersed in the bed and the other located under the distributor, used for temperature and heating rate control. The electric furnace is used to maintain the temperature of the bed at the desired value of 800 °C, permitting in this way to operate the reactor as a steam gasifier similarly in the dual fluidized bed gasifier operating system. The biomass feeding (*2*) is set at the top of the reactor and is ensured by an endless screw system powered by an electric motor. The fuel feeding is supported by a constant nitrogen flow, continuously sent to the biomass inlet pipe in order to avoid problems of agglomeration and choking. The fluidization of the bed material inside the gasifier is guaranteed by right amounts of air, nitrogen, steam or their mixes (*3*) feeding the reactor at a temperature of 450 °C. Steam is generated by an electrically heated boiler (*6*) fed by means of a dosing pump (*5*), which takes distilled water from a tank (*4*) at a constant flow rate. During the start-up, air is injected in the gasifier in order to enhance the fluidization and the heating of the bed material. During this phase the total amount of gas produced by gasification is completely burned in a torch (*8*). When steady state condition is established, steam is used as gasifying agent, in proper amounts depending on the steam to biomass ratio (SB). Since steam flow could not be sufficient to activate and support fluidization, nitrogen also is injected as inert in the reactor. During the gasification at steady state condition, only a part of the total produced gas feeds the torch and is burned, since the remaining quantity is sucked up by a vacuum pump (*13*) and used for the analysis. Gas produced by gasification has to pass through a primary gas cleaning section, consisting in a cyclone (*7*) and in a heated ceramic filter at 250 °C (*9*) in series, having the aim of remove ashes and fine particles.

The tar removal section of the system consists in two components: dolomite bed and oil scrubber for gas conditioning and cleaning respectively. The stainless steel secondary

reactor with an internal diameter of 7.5 mm (*10*) contains an upstream guard bed of calcined dolomite and is located in an electrical furnace, having temperature and heating rate control systems based on the thermocouple sited inside the catalyst bed. The scrubber unit is, instead, simulated by an impinger bottle (*11*) filled with vegetable exhaust oil, inserted in a water bath and continuously heated by a hot plate and thermally controlled by means of a thermocouple. Only during the tar removal experimental campaign, the produced gas passes even through this additional section.

Syngas then passes through other different impingers (*12*), filled with 2-propanol and placed in a thermostatic bath maintained at -10 °C by a chiller-thermocouple system, in order to condensate the remaining tars and the excess water, according to the tar guideline provided by the European Committee for Standardization [192]. The vacuum pump (*13*) sucks up syngas, free from tars and water, which is then analysed using a volumetric gas-chromatograph (*15*) (VARIAN CP-4900 micro-GC, Varian Inc). A Bronkhorst-El flow regulator (*14*) (Bronkhorst High-Tech B.V.) controls the slipstream of the raw gas. The 2-propanol mixed with tars is collected at the end of each test and successively analysed by means of a gas-chromatograph with mass spectrometry (Agilent GC-MS 5975C, Agilent Technologies).

Second gasification tests have been carried out even on a small-scale pilot gasifier with an input of 100 kW_{th} (*Figure 14*). It is a dual bubbling fluidized bed gasifier containing olivine sand as bed material, which acts as catalyst for gasification reactions and as thermal carrier. In this kind of gasification system, in fact, combustion and gasification zone are located in two different reactors communicating each other with a bed material circulation, thanks to some orifices and to the fluidization state. The gasification zone, fed with steam and biomass, produces, besides the producer gas, some charcoal, which circulates to the exothermic combustion zone together with the olivine. In the combustor, fed with hot air, the charcoal is burned, heating up the bed material at a temperature higher than the entrance one. When the olivine circulates back to the gasification zone, provides the thermal energy necessary for endothermic gasification reactions. Both the chambers are under atmospheric pressure, with great simplification of the system management, control and costs. A such gasification system, based on the dual bubbling fluidized bed with two chambers, is extremely attractive since it allows a gasification process using steam as gasifying agent. This is very advantageous since it allows to obtain a high-quality gas, with a

reduced amount of nitrogen content even if air, and not pure oxygen, is used for the combustion.

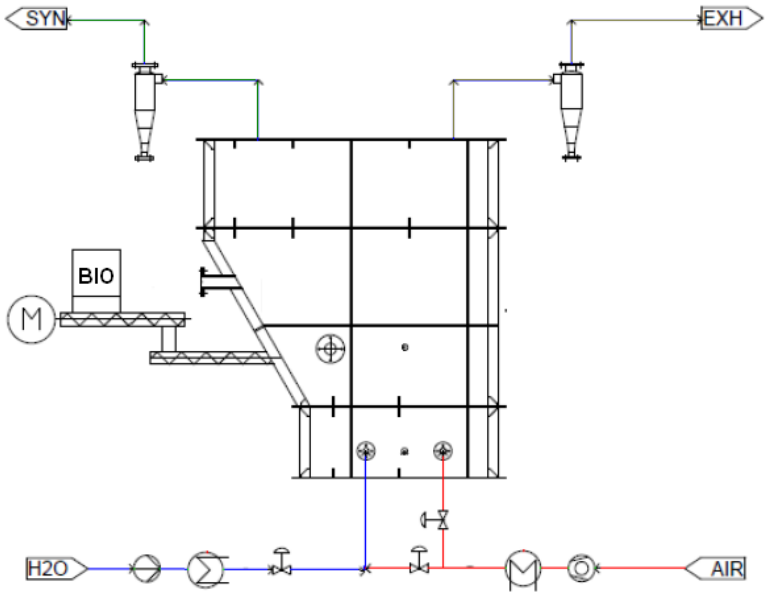

Figure 14. Scheme of the 100 kW_{th} pilot gasifier

An electrical resistance heats up the air for the combustion, while the steam is produced by a steam generator and superheated by an electrical resistance. Both gasification and combustion agents have an inlet temperature of 400 °C. Both the flue gas produced by the combustion and the gas produced by the gasification pass through a cyclone for particulate removal. Once reached steady state condition, a part (about 20 l/h) of the total producer gas is used for the analysis of gas quality and composition. It passes through the tar sampling system, consisting in a series of different impingers bottles with 2-propanol and placed in a thermostatic bath at -10 °C, similarly as in the previous bench-scale gasification system. A vacuum pump collects syngas free from tars and excess water and sends it to an online gas analyser (Advance Optima AO2020, ABB). The Agilent GC-MS 5975C gas-chromatograph with mass spectrometry was used for the evaluation of tar content in the 2-propanol mixture and thus in the syngas.

Gasification tests

Gasification tests with different input biomasses were carried out on the bench-scale apparatus (BFB gasifier) in the configuration without the tar removal section [193]. These

experimental activities were involved in the regional scientific projects “PSR-Utilizzo degli scarti di filiere agricole della Regione Lazio”. The aim of these projects was to evaluate the different biomasses availability of local agricultural food chains and simultaneously their thermal and electric needs to be satisfied by a proper biomass waste gasification system. Biomasses used as fuels are listed in *Table 6*, together with their preliminary and elemental analysis.

Pruning/ residues	***Moisture***	***Ash***	***Volatile matter***	***Fixed Carbon***	***LHV***	***C***	***H***	***N***	***O***
	Raw ($\%_{wt}$)				*(MJ/kg_{dry})*	*($\%_{wt}$)*			
Olive	21.4	3.2	64.0	11.3	19.2	48.0	6.1	0.6	45.3
Vine	34.9	3.6	52.3	9.2	18.6	56.8	6.8	0.7	35.8
Hazelnut	32.4	4.6	53.5	9.4	20.1	48.7	6.4	1.3	43.6
Kiwi	17.2	5.6	65.7	11.6	18.1	46.8	5.9	2.1	45.2
Oak	30.2	2.6	57.1	10.1	22.6	50.9	6.1	0.5	42.5
Beech	40.0	3.4	48.1	8.5	18.9	48.5	6.1	0.3	45.0
Pine	35.0	3.0	52.7	9.3	20.0	48.9	8.0	1.2	42.0
Hazelnut shells	6.4	1.7	78.1	13.8	18.8	51.1	5.8	0.4	42.6

Table 6. Preliminary and elemental analysis of biomass samples

Only residual biomasses were considered, since their higher sustainability: in particular, the ones resulting from the fruit trees pruning, the wood residues and fruits treatments like hazelnut shells. Moreover, only quite dry fuels with a high carbon/nitrogen ratio were tested, since the most suitable for biomass thermo-chemical conversions. Biomass samples as received were selected, dried, crushed and sieved, in order to reduce the moisture and the particles diameter (800-2000 μm) for the gasification process optimization. From *Table 6* it is evident that hazelnut shells resulted to have the best characteristics for gasification conversions. Moisture and ash contents are, indeed, very law while the lower heating value is at reasonable levels and the carbon content is one of the highest. These two latter represent the energetic content of the fuel and thus need to be as high as possible. The opposite necessity occurs for moisture and ashes, since the former is directly linked to thermal energy to be provided for drying and the latter are inorganic matter impossible to be gasified. Moreover, ashes generate fine particulate and, if present in elevated quantity, can melt and cause agglomeration with bed material besides some deposits on various parts

of the system: all of these substances have to be avoided or removed in order to prevent clogging and damage of all the various downstream components [194–196].

Biomass feeding rate was set at 300 g/h, while gasification temperature at 800 °C. Gasification tests were performed using steam as gasifying agent and pure nitrogen for supporting the fluidization. The duration of each test was of about 60 minutes. Producer gas compositions and characteristics are listed in *Table 7*.

Pruning/residues	***SB***	***H_2***	***CO***	***CO_2***	***CH_4***	***LHV***	***Gas yield***
			($\%_{vol}$)			*(MJ/Nm^3)*	*($Nm^3_{gas}/kg_{bio,daf}$)*
Olive	1	44.4	23.5	24.8	7.2	10.2	1.5
Vine	1	47.2	24.2	23.5	7.8	10.8	1.5
Hazelnut	1	46.8	21.6	22.3	7.2	10.2	1.4
Kiwi	1	48.6	20.2	24.3	7.0	10.2	1.3
Oak	0.6	39.2	26.1	21.3	9.9	10.8	1.2
Beech	0.6	38.0	21.9	24.8	10.0	10.1	1.1
Pine	0.5-1	45-49	23-20	20-25	10-9	11.1-10.8	1.5
Hazelnut shells	1	48.9	20.7	23.5	6.9	10.2	1.5

Table 7. Producer gas compositions and characteristics of different biomass samples

Differences in gas compositions resulting from different biomasses were not so relevant, since only hydrogen and methane contents showed the bigger variations, mostly due to the different steam to biomass ratio used in the tests: for higher SB, indeed, more steam is available in the gasification process and thus more hydrogen and, in turn, less methane are produced. The lower heating values of the different gases are hence quite similar each other. This is confirmed also by the gas yield, which is higher for gasification tests at higher steam to biomass ratio [197–199]. However, energetic value of the producer gas obtained from the bubbling fluidized bed gasifier of the bench-scale apparatus is quite relevant, since using steam as gasification medium leads to gases less diluted in nitrogen and thus with a higher LHV.

Also the tar content in the producer gases is quite constant for the different samples, having used olivine sand as catalytic bed material: averages of tar concentrations are listed in *Table 8*. Even if the heavier tar compounds are present only in a small amount, the dew point temperature of the producer gas, calculated by dew point model developed by the ECN - Energy research Centre of the Netherlands available online at [200], is around 90 °C. All the downstream components will have a temperature certainly lower than this: cooling

down the producer gas under its dew point temperature, tar compounds and especially the heavier ones will condensate and deposit, causing clogging and breakdown. Therefore, a tar removal and gas cleaning section is extremely important for the operation of a gasification system.

Compound	***Concentration (g/Nm^3)***
Benzene	12.6
Toluene	6.12
Xylene	0.85
Styrene	2.36
Phenol	2.61
Naphthalene	4.96
Fluorene	0.05
Acenaphthylene	0.23
Phenanthrene	0.04
Anthracene	0.04
Pyrene	0.01

Table 8. Average of tar concentration obtained by gasification of different samples

Several gasification tests at different operation parameters were performed also on the 100 kW_{th} pilot gasifier, in order to have information about a real gasification system. These research activities were involved in the Lazio Italian region scientific project "HyBioFlex-HBF" and in the European 7FP scientific project "UNIfHY (FCH JU 299732)". The aims of these two projects was to evaluate the possibility to integrate the innovative Dual Bubbling Fluidized Bed gasifier in two different plant configurations: the first to produce electric and thermal energy using an internal combustion engine; the second to produce pure hydrogen for fuel cell applications. Hazelnut shells ($CH_{1.4}O_{0.6}N_{0.01}$) were used as input biomass, with a constant flow rate of 20 kg/h. For the relative characterization see *Table 6*. Working parameters varied during the experimental campaign were the operating temperatures, the gasifying agents and their flow rates. In particular, both steam and air+steam gasification tests were carried out, with different steam to biomass ratio and equivalence ratio (*Table 9*),

in order to evaluate the advantages of steam gasification respect to the conventional air+steam. The duration of each test was of about 30 minutes.

	Test 1	***Test 2***	***Test 3***	***Test 4***
Gasifying agent	Air+steam	Air+steam	Air+steam	Steam
Steam (kg/h)	11	6	5	12
Air (kg/h)	39	31	31	70
SB	0.5	0.3	0.2	0.6
ER	0.3	0.2	0.2	-
Gasification T (°C)	783	850	835	730

Table 9. Working parameters of gasification tests on 100 kW_{th} prototype gasifier

Test results in terms of producer gas composition and tars content are showed in *Figure 15*. The tars chart displays only those compounds detected by the analysis instrument. It can be immediately noticed that N_2 content in steam gasification (Test 4) is obviously lower if compared with conventional air+steam gasification, leading to a producer gas less diluted and then with a higher energetic value. Lower heating value of producer gases generated from the latter were about 5 MJ/Nm^3, while that of the steam gasification resulted to be doubled with a value of about 10 MJ/ Nm^3. In addition, this value is perfectly in line with those obtained by steam gasification on the bench-scale apparatus. Lower dilution of the gas in nitrogen affects also the content of all the other compounds, which resulted in higher amount in the steam gasification test, even because of the higher steam to biomass. In any case, nitrogen amount in the producer gas from steam gasification test was around 23%$_{vol}$ and so not a negligible percentage: this should be due to some air leakage and to not adequate pressure equalization between the combustion and the gasification chamber. As regards conventional air+steam gasification tests, results from the different tests showed not so appreciable differences.

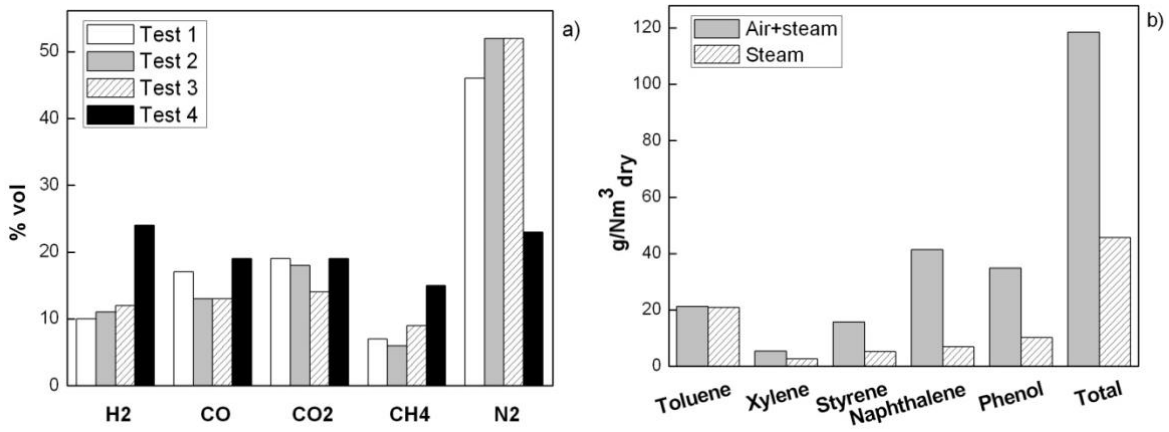

Figure 15. Producer gas composition (a) and tars content (b) of the 100 kW_{th} pilot gasifier

Concerning tar content, it is possible to note that also steam gasification generated too high amount, even if lower than in the case of air+steam. This was due to the low gasification temperature (730°C) and the difficulty to reach and maintain the desired value for all the experiments duration. Tar production, indeed, is favoured at low temperatures, which lead also to relevant concentration of phenolic compounds. The high tar content could be due also to the dimensions of the gasifier freeboard, which should be long enough to guarantee a good residence time of the producer gas and of the tars in the hot zone of the reactor in order to promote their conversion. Apparently, the shape of the gasifier seemed to be unsuitable for this.

An evaluation of the particulate matter was also conducted, by making the gas stream pass through a porous ceramic candle. After tests, the particulate trapped on the ceramic candle was collected for the analysis and burned in a muffle oven in order to evaluate its carbonaceous fraction and its ash content. The results obtained showed that the quantity of particulate generated by gasification was around 7.63 g/Nm^3. In addition, the carbonaceous fraction of the total particulate matter was the 57.3%, while the remaining 42.7% was supposed to be ashes.

The experimental campaign on the 100 KW_{th} prototype gasifier showed that the dual bubbling fluidized bed configuration could be extremely advantageous, since it allows a steam gasification process that leads to producer gas with higher quality in composition and higher energetic value respect to the conventional air+steam gasification process, but as showed further improvements are necessaries: some technical issues arose in the present system, affecting its optimum operation, such as the air leakages between the two

chambers and the dimension of the freeboard. Considering this, a new design of the DBFB pilot gasifier is under development with the aim of optimizing this innovative gasification system. Moreover, it has been noticed that the amount of tars in the producer gas from both analysed systems (the bench-scale and the pilot) resulted to be too high for operation and reliability of downstream components: a gas cleaning section is thus necessary for gasification systems.

Gas conditioning

It was previously stressed the importance of a tar removal section in a gasification system. Therefore, a gas cleaning and conditioning system for tar reduction in biomass gasification particularly suitable for the coupling with an ICE was studied, by means of experimental activities on a waste vegetable oil scrubber with or without an upstream guard bed of calcined dolomite [201]. The bench-scale steam gasifier was used for tests in the configuration showed in *Figure 13*. The aim of these studies, involved in the Lazio Italian region scientific project "HyBioFlex-HBF", was to verify the removal efficiency and to evaluate the stability of these two coupled gas cleaning and conditioning systems for several hours of operation. In particular, the gas cleaning section is related to the waste vegetable oil scrubber, which is based on gas adsorption process where the contaminant (tars) compounds are absorbed into the vegetable oil which acts as a very efficient absorbent media, thanks to its hydrophobic characteristics that enlarge tar solubility. On the other hand, the gas conditioning section is related to the upstream guard bed of calcined dolomite, which is a low cost and available catalyst for steam reforming/cracking of tars compounds, converting these into syngas, and thus recovering their energy content whilst reducing pollution (see chapter 1).

Biomass used as fuel was hazelnut shells, with a constant flow rate of 300 g/h. Preliminary and elemental analyses are showed in *Table 6*. The secondary fixed bed reactor of the bench scale apparatus, with an internal diameter of 7.5 mm, was filled with 9.8 g of calcined dolomite, resulting in 30 mm of guard bed height. The fresh dolomite used was kindly provided by Pilkington: its physical and chemical properties are listed in *Table 10*. The elemental analysis carried out on fresh dolomite reported that the mass fraction of Fe, CaO and MgO is respectively 0.01%, 30.39% and 20.56%.

Specific surface area of calcined dolomite (m^2/g)	15.20
Particle's diameter (μm)	400-600
Density (kg/m^3)	1850

Table 10. Physical properties of fresh dolomite

Before tests, dolomite was calcined at 850 °C overnight. In order to have a gas residence time in the catalyst of about 0.2 s, corresponding to about 80% of tar conversion [202], gas dry flow rate was set to 250 Nml/min by means of the Bronkhorst flow regulator. The temperature of the dolomite guard bed, continuously heated by the electrical furnace, was set at 800 °C [66,203]. The tests with exhausted vegetable oil were conducted in a impinger bottle (called as scrubber). The amount of oil used was 40 ml in order to have, with the flow of 250 Nml/min, an estimated residence time between 1 s to 10 s, in accordance with typical residence times for industrial cold cleaning systems in literature [61,204,205]. The vegetable oil has been maintained at a constant temperature of 50 °C, by means of a water bath: this temperature is in line with that obtained with a real scrubber [206] in a 8 MW scale gasification power plant and with the operation temperature declared in the work of Anis and Zainal [207]. In a real application, it can be convenient if the gas is cooling down prior to enter in the unit scrubber, in order to exploit the released heat for other thermal energy needs in the plant and increase in this way its overall efficiency. All the system's operating conditions are listed in *Table 11*.

Biomass feed rate (g/h)	300
Gasifier T (°C)	800
Steam (g/h)	378
SB	1.3
Gas Residence Time in dolomite (s)	0.2
Dolomite guard bed T (°C)	800
Gas Residence Time in oil (s)	1.00
Scrubber T (°C)	50

Table 11. Operating conditions of the gas cleaning and conditioning tests

The main fatty acids contained in the oil used are shown in *Table 12*. The composition was obtained by GC analysis of the derived methyl-esters.

	($\%_{wt}$)
Linoleic Acid	48.42
Oleic Acid	33.94
Palmitic Acid	7.21
Stearic Acid	4.13

Table 12. Fatty acids composition of the oil used

For each gasification test, both gas composition and its concentration of tars were analysed. Gas and tars have been collected before and after the tar removal section, in order to evaluate its efficiency. Tars were classified in 6 categories, lumping together the elements with similar chemical structure and ordered from lighter to heavier compounds [208]:

- benzene;
- one-ring compounds (excluding benzene): toluene, xylenes, styrene, indene, methyl-indene, indan, thiophene, ethyl-benzene, methyl-benzene;
- naphthalene;
- two-ring compounds (excluding naphthalene): methyl-naphthalenes, biphenyls, acenaphthene, acenaphthylene, fluorine, benzofurans, methyl-benzofurans;
- three and four-ring compounds: anthracene, phenanthrene, fluoranthene, pyrene, dibenzofuran;
- phenolic compounds: phenols, methyl-phenols.

In order to evaluate performances of oil scrubber for removal of tars impurities in producer gas flow, biomass gasification tests were performed using only oil scrubber in the gas cleaning section. The total experimental period was 2.5 hours. Tests results over the time are showed in *Figure 16*. Tars reduction is very high in the first hours of operation, almost 100% in the case of heavier aromatic hydrocarbons and around 90% for the others (except for benzene). These results are in line with literature, confirming that use of vegetable oil scrubber is effectively advantageous respect to other scrubbing media [78]. Literature results, however, regarded only the first 90 minutes of scrubbing media operating. Our results demonstrated that after 1.5 hours of operation the reduction abruptly decreases, reaching even values below 20% for lighter compounds. This is confirmed also by the gas dew point temperature calculated by [200], which is 0.9 °C and 77.3 °C after 1 and 1.5 hours of operation respectively. These values also demonstrate that,

after 1.5 hours, the reduction of tars is not more due to the oil scrubber cleaning activity but to the condensation of tars in a section at 50 °C, that is lower than the dew point temperature. These considerations demonstrate that exhaust vegetable oil was not more able to physically absorb tars present in the producer gas and it is possible to assume, then, that oil saturation occurred. The different reduction ability for different tars is due to their different physical properties: benzene and one ring compounds, in fact, are more volatile than the others and thus are more difficult to be trapped by the scrubbing media. In addition, a dew point temperature of 77.3 °C is not acceptable, since condensation of tars could seriously damage all the components downstream the gasification system.

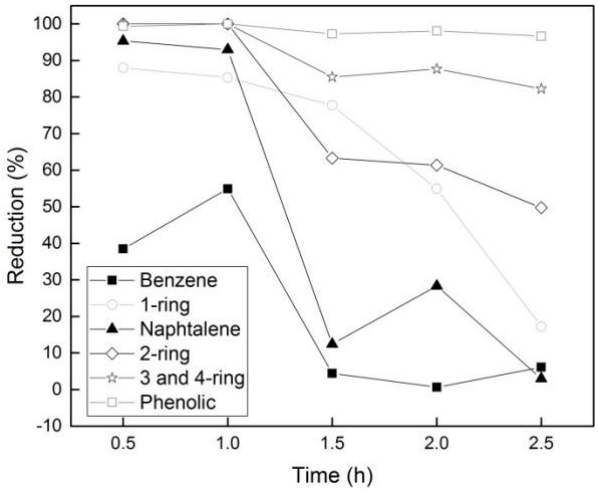

Figure 16. Reduction of tars by means of the scrubber oil

Therefore, using only oil scrubber in the gas cleaning unit is not suitable for efficiency and sustainability of the considered process: a rough estimation shows that, for a steam biomass gasification system, about 4 litres of oil for each kg of biomass would be necessary. Vegetable oil used as scrubbing media could be sent and burned into a combustion zone directly connected with the gasifier in order to provide the extra heat necessary for the endothermic gasification reactions. However, with a saturation limit of only 1.5 hour, the amount of exhausted oil available is higher than the reactor's needs.

Subsequently, performances of the complete conditioning system were analysed, conducting gasification tests with dolomite guard bed and oil scrubber. 8 gasification tests of 60-120 minutes have been performed, for a total amount of 12 hours of experimentations. *Figure 17* shows the time change in reduction of tars concentration by

means of the complete conditioning system. It is possible to note its effectiveness and the great reductions in tars concentration respect to those present in the reference gas. Heavier hydrocarbon in the conditioned gas are present always in very low concentrations, even lower than the detection limits of the analysis instrument, also after 12 hours of operation of the dolomite guard bed and the oil scrubber. As regards light aromatic hydrocarbons, that are benzene and the one-ring compounds, the conditioned gas has lower concentration respect the reference one, even if in moderate quantities. In any case, the conversions and reductions of tars thanks to dolomite and scrubber are quite high: reduction close to 80% are reachable for benzene and one-ring compounds, while heavier aromatic hydrocarbons could be reduced even at almost 100%.

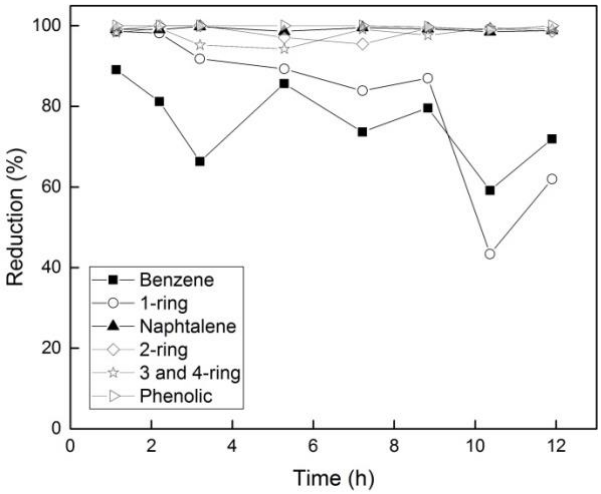

Figure 17. Reduction of tars by means of dolomite guard bed and oil scrubber

Although the results show that reduction of benzene and one ring compounds is the most difficult to achieve, it is known that for engine purposes only hydrocarbons with a dew point temperature higher than about 100 °C could cause fouling or blocking in downstream components [45]. Hence, presence of benzene and toluene in the gas stream does not cause any technical problems to the system [65] and, therefore, our analysis could be focused mainly on the heavier aromatic hydrocarbons. Literature is not clear on the tars concentration range admissible for ICE. Most of them say that it should be between 20 $mg \cdot m^{-3}$ and 500 $mg \cdot m^{-3}$ in standard conditions: it depends on the composition of heavier hydrocarbons. One of the most appropriate way to evaluate if concentration of tars is acceptable is the dew point calculation, as confirmed also by [45]. *Figure 18* shows

concentration of total tars presents in the gas stream (without considering benzene (C_6H_6) and toluene (C_7H_8)), analysed both at the inlet and exit of the conditioning system.

The reduction of total amount of hydrocarbons (except benzene) operated by conditioning system is very high, since the concentration passes from 6.01±1.79 g/Nm^3 in the reference gas to 2.46 g/Nm^3 in the conditioned gas after 12 hours of operation, and it has a further great decrease when only heavier hydrocarbons are considered (MW>C_7H_8). Indeed, taking into account only dangerous tars for engine equipment, its concentration in the gas stream is lowered to only 0.16 g/Nm^3, with a reduction of 97% of total tar concentration in the producer gas. The amount of tars absorbed by the exhaust vegetable oil was very small, equal to 0,77 mg/Nml, confirming the effectiveness of the dolomite guard bed to crack tars. Even the dew point temperature has a great decrease, from 84.2 °C at the inlet of the conditioning system to 16.7 °C at its outlet. This is a reasonable value, since all downstream components will be at a temperature certainly higher than 17 °C.

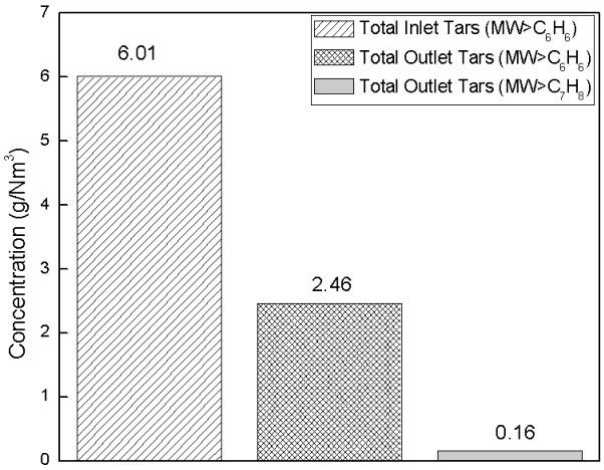

Figure 18. Total tar concentrations at the inlet and exit of the complete conditioning system

Finally, performances of dolomite guard bed have been investigated. Two additional hours of gasification tests were carried out, with a conditioning system in which the scrubber device was excluded and, thus, only the secondary reactor with previously used dolomite was included. *Figure 19* shows reduction of tars concentration by means of the dolomite bed. It is possible to note that reduction of each tar component is still quite high, even after 14 hours of dolomite's operation. In particular, heaviest hydrocarbon had a reduction in the range of 100-80%, while only the lighter benzene was reduced of only 54%.

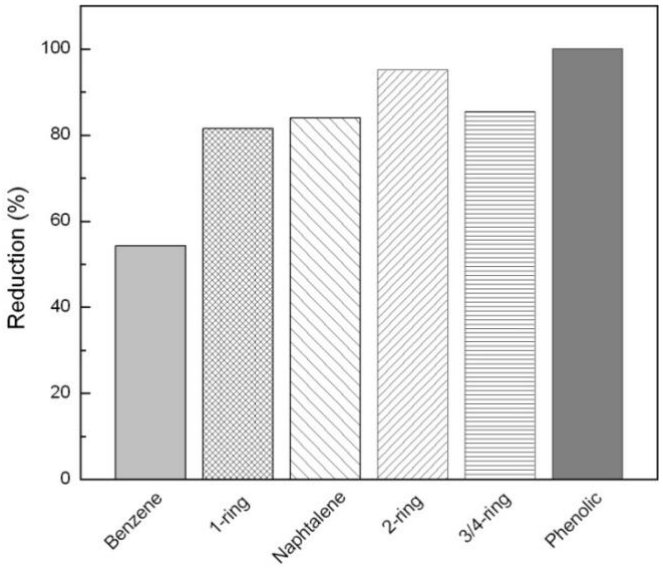

Figure 19. Reduction of tars by means of dolomite guard bed after 14 hours of operation

Since these results, it is possible to affirm that the tar removal action of the complete conditioning system (dolomite bed plus oil scrubber) in a long period of operation is almost entirely due to the dolomite's effects. However, oil scrubber downstream presence is anyway profitable and necessary. In fact, dew point temperature of tars mixture coming out from the conditioning system with only dolomite (used for 14 hours) is 56 °C, too high for components safety and operation and much higher than 17 °C obtained with both cleaning and conditioning systems. In addition, according to the work of Orìo et al. [202], use of only dolomite bed provides tar reduction of 80-90%; tar reduction resulted by the complete system analysed in this work, instead, was around 97%, confirming the necessity of the scrubber unit.

After test BET analysis was carried out on dolomite after its usage in the guard bed. Specific surface area obtained was 6 m^2/g, lower than that of fresh dolomite, probably due to sintering phenomena occurred since the high operating temperature. Dolomite, in addition, resulted to be of a black colour, indicating the formation of carbon on it. Further studies need to be developed in order to quantify this carbon deposit, especially for a longer operating time of the dolomite guard bed.

Hence, a proper tar removal action could be feasible only with the operation of the complete gas cleaning and conditioning system, characterized by great efficiency with reduction of 80-100%, in particular 97 % in the case of hydrocarbons with MW>C_7H_8.

The gas cleaning apparatus here analysed showed high efficiency in tar removal. However, it implicates cooling down of producer gas to around 50 °C. This is a drawback in the case of its utilization in devices such as high temperature fuel cell as SOFC or MCFC or in additional high temperature syngas treatment for biofuels production, as hydrogen production or Fisher Tropsch processes. In these cases, indeed, hot gas cleaning and conditioning methods are preferable. In particular, the production of pure hydrogen from biomass gasification was deeply investigated in the fields of European 7FP scientific project "UNIfHY (FCH JU 299732)". Studies about the global system with hot gas conditioning section have been carried out and are discussed in the following paragraph.

Global simulation

Experimental activity on gasification and gas conditioning tests revealed that system's performances are quite dependent from some fundamental parameters as steam to biomass ratio, gasification temperature and operation of other system's components such as the condition and cleaning section. It is evident, thus, that innovative devices for system's control like chemoresistive gas sensors are highly necessary. However, biomass conversion could have several scopes, for example production of syngas for ICE feeding or for production of hydrogen for fuel cells feeding. These different purposes implicate different configuration, which, in turn, are characterized by different operating parameters. In particular, biomass gasification systems for production of syngas to be used in an internal combustion engine involve relative low restrictions in terms of contaminants and impurities allowed in the gas streams. Moreover, as previously discussed, the gas cleaning section operates at low temperature (about 50 °C). The importance of chemoresistive gas sensors is then minimized in these kind of plants. The biomass gasification for hydrogen production, instead, involves the hot gas cleaning and conditioning and also higher impurities restrictions, as also showed in chapter 2. A global simulation of a hydrogen production plant from biomass gasification by means of the innovative DBFB has thus been carried out, with the aim of evaluate the integration of the innovative gasifier in a real application and to identify which are the streams and their main features where apply the gas sensors [209]. These activities are part of the simulations carried out in the European 7FP scientific project "UNIfHY (FCH JU 299732)". An innovative biomass to hydrogen system, based on steam gasification technology coupled with gas cleaning and purification components, was

simulated by means of the ChemCAD® flowchart. Simulation studies on the DBFB gasifier integrated in a complete biomass gasification plant for the production of pure hydrogen were carried out. In particular, the simulations were carried out on a specific small-scale plant (1 MW_{th} as biomass input) able to produce around 400 kg/day of hydrogen and operating at atmospheric pressure. The overall plant has been simulated by means of ChemCAD® software. The simplified ChemCAD® flowchart used for simulations is showed in *Figure 20.*

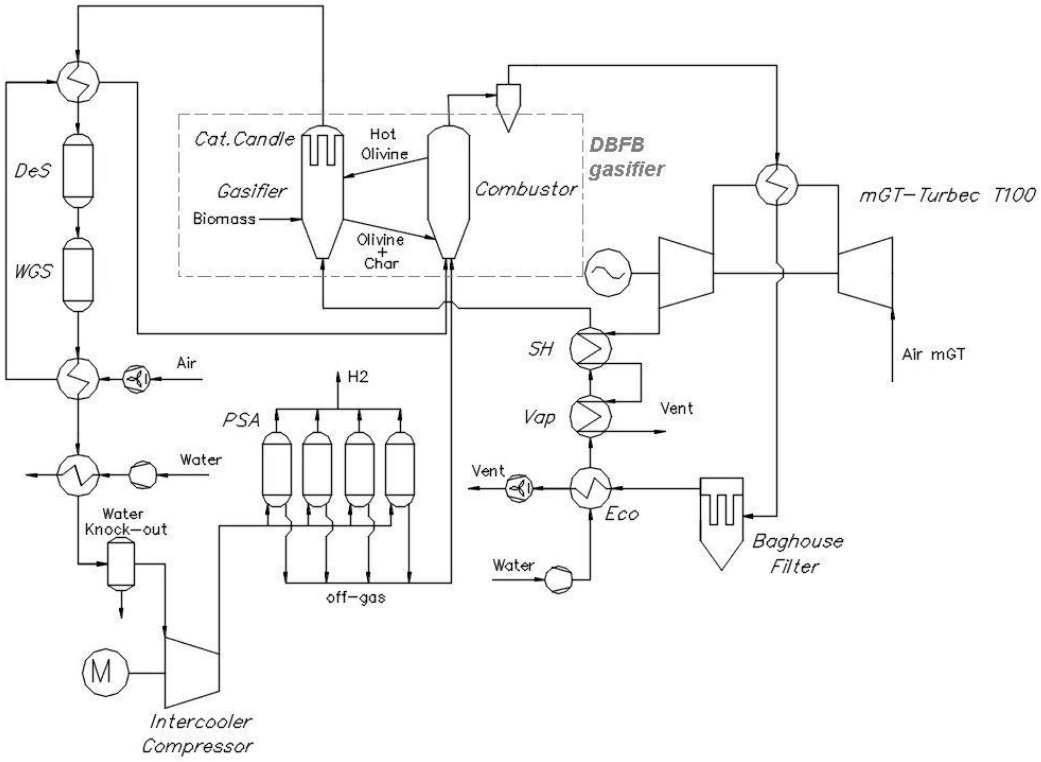

Figure 20. Flow sheet of the biomass to H2 gasification plant used for global simulations

The gasification section is bases on the dual bubbling fluidized bed gasifier previously showed: gasification zone fed with steam and combustion zone with air, with an exchange of olivine and charcoal between the two chambers for the thermal energy supply. In this case, however, the gas conditioning section for tar conversion is implemented inside the gasifier. In particular, a series of catalytic filter candles are used for the particulate removal and for the conversion of tars in additional syngas, being them a hot gas cleaning and conditioning method based on the catalytic cracking and steam reforming of low and high

molecular weight hydrocarbons. Indeed, they are ceramic and porous filter candles with some traces of nickel, whose catalytic action and steam presence lead to the conversion of tars compounds in additional H_2 and CO in the gas stream. They offer several advantages, such as high tar conversion, hydrogen rich syngas production and thermal integration with gasification reactor. Following the UNIQUE concept [87], in fact, they are installed directly in the freeboard of the fluidized bed gasifier, resulting in a compact configuration with consequent remarkable plant simplifications and reduction of costs. The so produced free from tars syngas is then sent to the low temperature Water Gas Shift reactor (WGS), where CO is converted in additional H_2 and CO_2 thanks to the reaction with steam. It is an innovative WGS system, consisting of ceramic foams impregnated of copper (Cu) catalyst, capable of increase the efficiency of the gas-solid contact (catalytic surface area): in this way, the WGS can operate at atmospheric pressure and can be coupled with atmospheric pressure gasification as the DBFB gasifier. The WGS reactor is equipped with a desulphurization reactor (DeS), fundamental for the removal of sulphur in the gas stream, which otherwise could seriously damage the activity of the catalytic foam. The gas from WGS is mainly composed of H_2, CO_2, residual steam and traces of CH_4 and CO. The gas first preheats the air for the dual fluidized bed gasifier, and then passes through a condenser where residual steam is removed. The dry gas is cooled to ambient temperature and compressed at relatively low pressure to feed the Pressure Swing Adsorber system (PSA), where H_2 is separated from residual gases. Off gas from PSA is burned in the combustion zone to supply extra heat required by the gasification process. Finally, the sensible heat of the flue gas from the combustor at 950 °C is used to supply energy to the micro gas turbine (mGT), where electrical power required for the plant is generated. Outgoing air from the turbine still at high temperature is used to generate superheated steam. The system for upgrading of raw syngas to pure hydrogen is a portable purification system and it is composed by DeS, WGS, intercooler compressor, PSA and auxiliaries.

A sensitivity study has been carried out, studying both chemical and energetic aspects, by varying three parameters:

- steam to biomass ratio from 1.0 to 2.0;
- operating temperature of the WGS reactor between 250-350 °C;
- residence time and, thus, WGS reactor length.

Regarding the system's modelling, the steam-gasifier was simulated by means of a purposely developed and experimentally validated MATLAB® model then interfaced in ChemCAD®. Details of that model are available in the work by Di Carlo et al. [101,102]. For the remaining components conventional ChemCAD® blocks were used.

The catalytic filter candles were simulated using a stoichiometric reactor. The most representative and abundant heavy aromatic hydrocarbons that compose tars were considered for simulation: benzene, toluene (1-ring representative excluding benzene) and naphthalene (2-rings representative). The reactions considered are water gas shift and steam reforming of methane and tars. In *Table 13* are listed the conversion rate of each component at different steam to biomass ratio, data taken from the work of Savuto et al. [210], experimentally validated.

	SB=1.0	***SB=1.5***	***SB=2.0***
c_{CH4} ***(%)***	-18.5	-31.4	-36.7
c_{CO} ***(%)***	15.7	18.8	20.2
c_{C6H6} ***(%)***	-49.3	-39.7	-36.1
c_{C7H8} ***(%)***	-72.3	-70.0	-69.4
c_{C10H8} ***(%)***	-88.7	-84.3	-82.0

Table 13. Conversion rate (c) of components in the stoichiometric reactor of catalytic candles [210]

The sulphur removal reactor (DeS) was simulated with a chemical equilibrium reactor based on ZnO, where the equilibrium constant of the desulphurization reaction has been used. Industrially and commercially, the accepted H_2S concentration with regards to the low temperature WGS must be lower than 1 ppm and preferable lower than 0.1 ppm [105,211,212]. The copper catalyst, otherwise, will deactivate due to its irreversible reaction with sulphur. Commercial ZnO had good potential for desulphurizing the gasifier gas and the optimal operating temperature is very similar to that of the low temperature WGS catalyst. It was assumed that the reaction of H_2S with ZnO could be considered at equilibrium. The K_{eq} for this reaction was obtained by thermodynamic data and is presented below:

$$\frac{p_{H_2O}}{p_{H_2S}} = K_{eq} = 0.8095 exp^{\frac{9128}{T}} \quad \textbf{(3.1)}$$

WGS reactor was simulated as a Plug Flow kinetic reactor, where the apparent reaction kinetic has been extrapolated from isothermal micro-reactor tests carried out in the UNIFHY

project with the Cu-impregnated ceramic foam utilised in the construction of the reactor for this project [213].

The Arrhenius parameter values obtained are shown in *Table 14*.

A (1/s)	66769.0
E (kJ/mol)	51.6

Table 14. Arrhenius parameter (A) and activation energy (E) for the WGS reaction rate

Activation energy is in line with literature data for similar Cu catalyst, which varies between 19 and 86 kJ/mol [211]. Foams have ceria loading of 8.8%$_{wt}$ and copper loadings of 5.0%$_{wt}$ and a porosity of 45 ppi. The cylindrical foams can be organized in stack to increase the height of the reactor and therefore the gas residence time in the reactor. The hypothesis of plug flow is, thus, fully justified being the reactor a packed bed effectively.

For the PSA unit a component separator with the specific separation efficiency was used, while conventional ChemCAD® blocks simulated compressor, turbine and heat exchanger related to micro gas-turbine system. In order to have realistic data, Turbec T100 was chosen as micro-turbine [214], whose compressor and turbine characteristic maps were calculated, in particular the pressure ratio and efficiency of the two machines at different rotational speed, different airflow and different temperatures. The analytical models developed by Zhang and Cai [215] were used, starting from the constant parameters given by [214], and implemented in the ChemCAD® blocks. Thanks to this model, it was possible to simulate the micro-turbogas at different operating conditions obtained by the simulations of the entire plant.

Simulations were carried out considering hazelnut shells as input biomass, whose constant flow rate (dry and ash free) was set to 200 kg/h (1000 kW$_{th}$). For the relative characterization see *Table 6*. The other main assumptions of the process are listed in *Table 15*. The air blower considered is an Elmo Rietschle GBH1, model 2BH1 910 [216], while the PSA intercooler compressor is a Mehrer dry cylinder compressors [217,218]. Main parameters assumed for PSA were taken from experimental results in [219].

Gasifier operating T (°C)	850
Burner operating T (°C)	950
Olivine sand circulated Burner-Gasifier (kg/h)	12000

Steam and Air T (°C)	600
Burner and Gasifier operating absolute P (bar_a)	1.1
Turbine inlet T (°C)	900
PSA separation efficiency (%)	70
PSA inlet absolute P (bar_a)	7
PSA Intercooler Compressor isentropic efficiency (%)	62
PSA Intercooler Compressor T (°C)	40
Intercooler Compressor stages	2
WGS gas inlet temperature (°C)	250;300;350
Air Blower pressure ratio	1.3
Air Blower isentropic efficiency (%)	40.0
Water pump pressure ratio	3.0
Water pump isentropic efficiency (%)	80

Table 15. Simulations system operating condition

The sensitivity study was carried out firstly by varying the steam to biomass ratio (SB) between 1.0 and 2.0. The WGS inlet gas was cooled down to 300 °C. The residence time of the gas in the WGS reactor was set at 0.5 s and the height of the catalyst packing in the WGS reactor was varied, accordingly, for each SB ratios considered. The off gas coming from the PSA system feeds the combustor to supply the extra heat for the gasification process. The off gas should be used completely to increase the overall efficiency. Each of these assumptions influences the heat and mass balances of the plant. The hydrogen chemical efficiency (η) has been calculated by the following equation (based on LHV or HHV):

$$\eta_{LHV(or\ HHV)}[\%] = \frac{\dot{m}_{H2} * LHV_{H2}(or\ HHV_{H2})}{\dot{m}_{bio,daf} * LHV_{bio,daf}(or\ HHV_{bio,daf})} \cdot 100 \qquad \textbf{(3.2)}$$

where $\dot{m}_{H2}$ is the mass flow rate of the produced hydrogen and $\dot{m}_{bio,daf}$ the mass flow rate of biomass feedstock, dry and ash free. *Table 16* shows composition of syngas produced from gasification at different steam to biomass ratio. It is possible to note that an increase in SB produces a decrease of carbon monoxide content, influencing thus the H_2 conversion by means of water gas shift reaction. Moreover, tar and methane amounts are always extremely low, thanks to the quite high conversion rate of the catalytic filter candles. As regards sulphur content in the syngas at the inlet of the water gas shift reactor, it is always less than the technical limit of 0.1 ppm, as the WGS reactor requires, showing the good operation of the DeS guard bed.

	SB=1.0	***SB=1.5***	***SB=2.0***

H_2 ($\%_{dry}$)	49.9	52.1	52.7
CO ($\%_{dry}$)	22.5	21.5	21.6
CO_2 ($\%_{dry}$)	20.1	20.3	20.1
CH_4 ($\%_{dry}$)	7.3	5.8	5.3
H_2O ($\%_{wet}$)	33.0	44.6	53.2
C_6H_6 (g/Nm^3_{dry})	5.7	7.1	7.9
C_7H_8 (g/Nm^3_{dry})	1.3	1.6	1.9
$C_{10}H_8$ (g/Nm^3_{dry})	0.3	0.8	1.2
H_2S (ppm)	4.9E-02	6.6E-02	7.9E-02

Table 16. Syngas composition at the outlet of gasifier with integrated CF

CO conversion in the WGS reactor slightly decreases with SB. An increase of steam in the gas has an "inertial" effect and mitigates the gas temperature, thus temperature is lower at higher SB. The hydrogen chemical efficiency of the whole plant is shown in *Figure 21* as a function of the steam to biomass ratio.

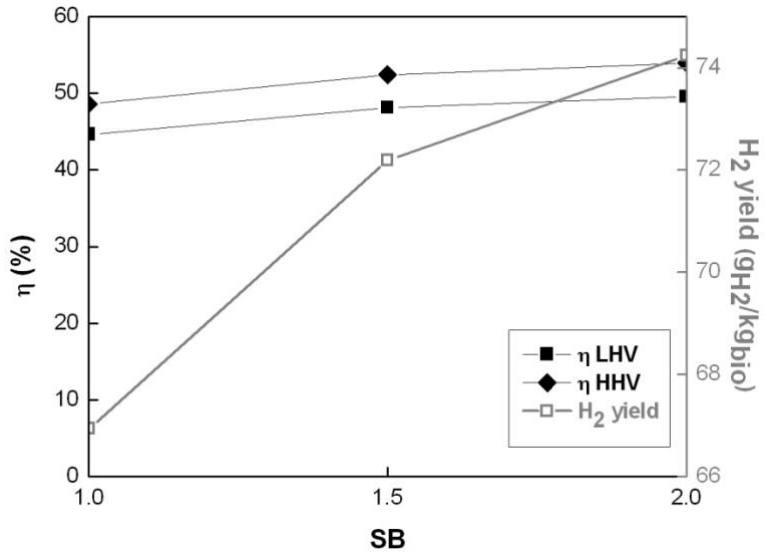

Figure 21. H_2 chemical efficiency, LHV and HHV based, and hydrogen yield

Thanks to the higher SB, more steam can react in the different reaction processes, producing more hydrogen. SB influences efficiency, showing asymptotic trend and quite considerable increase. Nevertheless, the maximum efficiency based on HHV obtained is 54.0%. This value is high but lower than the target of UNIfHY project 66% [220]. The main reason is probably due to the low CH_4 conversion in the catalytic filter candles far from equilibrium conditions. In fact, catalytic filter candles are developed mainly for tars conversion, which is quite high as shown previously in *Table 13*, and not for the direct

conversion of methane. The hydrogen yield varies between 66.9 and 74.2 g_{H2}/kg_{bio} for SB equal to 1.0 and 2.0 respectively then, at these ranges, H_2 yield is increasing function together of SB as observed by other researchers [221–225]. *Table 17* the electric consumption and production of the studied system at different steam to biomass ratio.

	SB=1.0	***SB=1.5***	***SB=2.0***
Water Pump power consumption (kW)	1.2E-02	1.9E-02	2.6E-02
Air Blower power consumption (kW)	26.2	25.8	25.6
Intercooler compressor power consumption (kW)	44.1	47.4	48.4
Gas Outlet T Eco (°C)	137.2	112.1	92.5
Air Outlet T Vap (°C)	416.3	272.5	123.8
mGT Total power production (kW)	70.7	70.2	69.9
Net Electric Power (kW)	0.4	-3.0	-4.1

Table 17. Energy balance of the system at different SB

Compressor and turbine efficiency and pressure ratio are constant for the different SB, since the mass airflow is quite the same in the different configurations. This leads to a quite constant electric energy production by the mGT for different steam to biomass ratio. On the other hand, an increase in SB produces an increase in the electric consumption of the system, since the syngas produced and compressed from the intercooler compressor is slightly increased. For these reasons, the energy consumptions of the entire system are covered only for SB lower than 1.0, being present an electric energy lack of about 3-4 kW for the remaining cases. Anyway, as it is possible to note from *Table 17*, the energy lack is very similar for SB of 1.5 and 2, while the chemical efficiency is a little bit higher in the second case (η=54.0%). For SB=2.0, it is possible to have also a better exploitation of the thermal energy available from the system, as shown by the decreases of the fluids outlet temperature both from economizer and vaporizer. SB equal to 2 is, thus, preferable among the three cases analysed.

To complete the sensitivity study, also WGS reactor temperature and residence time were varied at a fixed steam to biomass ratio. It was chosen to study the case with SB=2.0 that is the case that maximize the hydrogen production. *Figure 22* shows the chemical efficiency of the hydrogen production at different WGS reactor temperature, at the fixed residence time of 0.5 seconds. The hydrogen chemical efficiency has been calculated

considering both the lower heating value and the higher heating value for the inlet gas ranging between 250-350 °C.

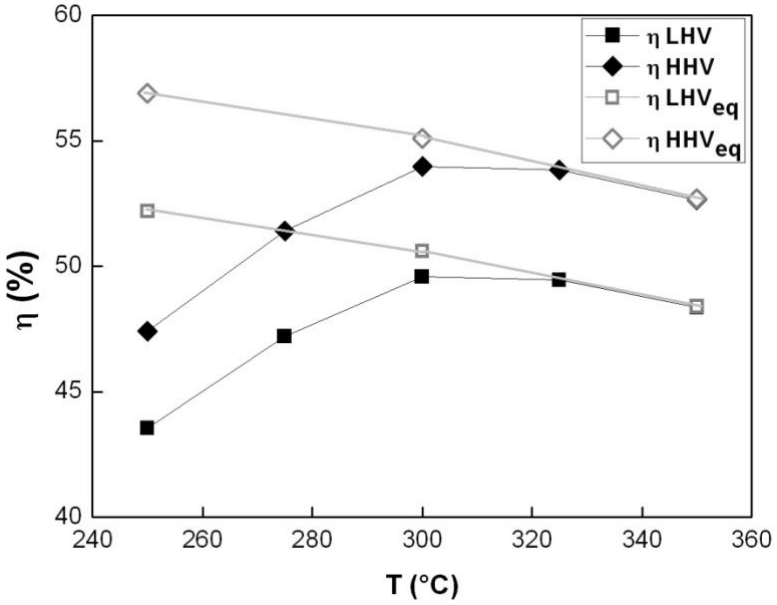

Figure 22. Chemical efficiency of hydrogen production at different WGS inlet gas temperature

The chemical efficiency increases with increasing inlet temperature. Considering the lower heating value, it varies between a minimum of 43.5% and a maximum of 49.6%, while, considering the higher heating value, its maximum is 54.0%. Both the maximum efficiencies are reached at a temperature of 300 °C and any higher values of the operating temperature are prohibitive for H_2 production. This is due to the kinetics of water gas shift reaction that is enhanced at high temperature, even if the thermodynamic equilibrium is not. Nevertheless, it is clear that the curves of chemical efficiency show a maximum above a certain inlet temperature level, around 300 °C. As shown in the figure, the thermodynamic equilibrium is reached with this catalyst at this temperature. A further increase of inlet temperature would reduce the equilibrium CO conversion and the hydrogen yield; therefore, it is not convenient to exceed 300 °C: any higher inlet temperature value will not provide better results in terms of chemical efficiency of the system.

	T=250 °C	***T=300 °C***
Water Pump power consumption (kW)	2.6E-02	2.6E-02
Air Blower power consumption (kW)	29.8	25.6
Intercooler compressor power consumption (kW)	45.1	48.4
mGT Total power production (kW)	85.7	69.9

Net Electric Power (kW)	10.8	-4.1

Table 18. Energy balance of the system at different WGS reactor operating temperature

Regarding the electric consumption (*Table 18*), at an operating temperature of 250 °C, relative to the minimum chemical efficiency, the energy balance of the system is positive, producing a surplus of electric energy of about 10.8 kW, which can be used for the remaining energy consumption of the system. Nevertheless, the minimum chemical efficiency reachable leads to assume that this operating temperature is not convenient.

The chemical efficiency of hydrogen production obtainable from such a system varies also with the residence time of syngas through the water gas shift reactor. To vary syngas residence time, it was varied the WGS reactor length, in order to enhance CO conversion, at the fixed inlet temperature of 300 °C. *Figure 23* provides the dependence of hydrogen chemical efficiency (η) on residence time, which varies between 0.3 and 1.1 seconds.

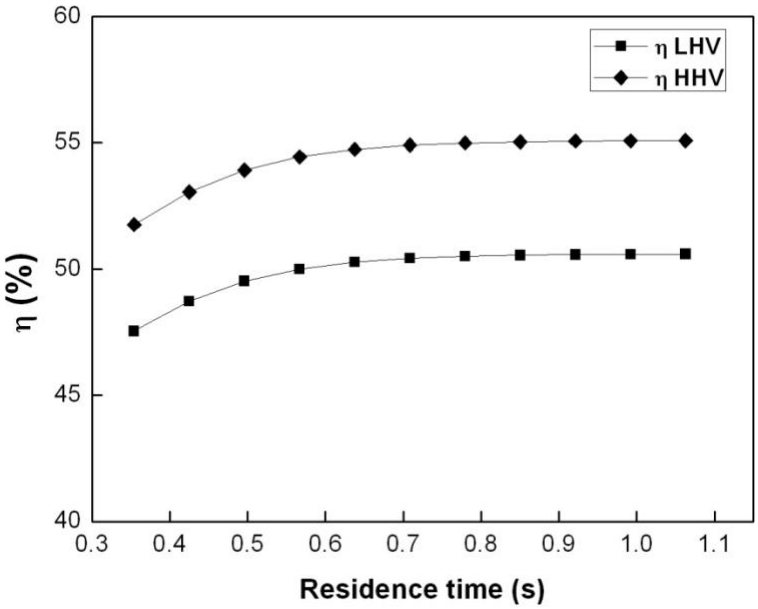

Figure 23. Chemical efficiency of hydrogen production at different residence time in the WGS reactor

The longer the residence time, the higher the chemical efficiency of hydrogen production, because more CO is converted in H_2. This allows obtaining slightly higher value of system's chemical efficiency at the same inlet temperature: 50.6% (LHV) and 55.1% (HHV) with a residence time of 1.1 and a hydrogen yield of 75.2 g_{H2}/kg_{bio}. However, as it is shown

in *Figure 23*, with residence time longer than a certain value, that in this case is 0.8 s, the curves show a plateau. Hence, exceeding this residence time, and thus increasing the height of reactor, it is not convenient neither for economic reasons nor for efficiency reasons. We can conclude that the optimum range of values for residence time is estimated to be 0.5-0.8 s.

In *Table 19* are listed summaries of the electric consumption and production of the studied system at different syngas residence time through water gas shift reactor. It was chosen to study two residence times, 0.3 s and 0.5 s, which represent, as it can be seen from the previous *Figure 23*, the worst and the best case respectively, from a chemical efficiency point of view. At lower residence time, the electric energy gap is lower but also the H_2 produced is lower. At the same time, a residence time of 0.8 s implies a more negative system energy balance, but slightly higher (less than 1 kW of difference) than the electric energy gap related to 0.5 s of residence time at the same temperature and steam to biomass, 4.1 kW as shown in *Table 17*. It is possible to assume, thus, that 0.8 s represents the best value for residence time of syngas in WGS reactor.

	Res. time=0.3	***Res. time=0.8***
Water Pump power consumption (kW)	2.6E-02	2.6E-02
Air Blower power consumption (kW)	27.0	24.9
Intercooler compressor power consumption (kW)	47.3	48.9
mGT Total power production (kW)	76.6	69.2
Net Electric Power (kW)	-2.3	-4.7

Table 19. Energy balance of the system at different syngas residence time through WGS reactor

It should be stressed here that any change in the gas stream inlet temperature to the WGS reactor and in the residence time modifies the temperature profile along the reactor, which is supposed to operate under adiabatic conditions, with consequences of opposite sign on the WGS equilibrium conversion and on the reaction kinetics. As a result, the above discussion about the influence of these parameters on the chemical efficiency reached for hydrogen production in each condition is not trivial nor leading to an outcome easily predictable.

4. Experimental Activity on Gas Sensors

On the basis of what discussed in the previous chapter, it is possible to note that reliability and efficiency of biomass gasification systems are strictly correlated to the setting of precise operating parameters and the good functionality of different components, in order to obtain an output gas with specific composition and quality. Proper monitoring and control devices are then very crucial, even for sustainability and safety reasons. Therefore, experimental studies on innovative chemical gas sensors have been carried out (see chapter 2). In particular, gas sensing properties of $LaFeO_3$-based perovskite materials were deeply investigated for typical gases involved in biomass gasification and different operating temperatures, including also investigations about the optimization of synthesis method. These activities were developed in the laboratories of ENEA Italian research centre.

Materials preparation

Perovskite materials tested for gas sensing properties evaluation were lanthanum ferrite perovskite, in the classical form ($LaFeO_3$) or with partial substitution of iron ions with other chemical elements with higher activity, such as titanium or cobalt ($LaTi_xFe_{1-x}O_3$, $LaCo_xFe_{1-x}O_3$ and $LaTi_xCo_zFe_{(1-z-x)}O_3$).

Different samples were prepared by means of auto-combustion synthesis technique, via citrate-nitrate method [226–229]. Perovskites, in fact, usually have small surface area because they are prepared by solid-solid reactions at high temperatures that promotes sintering processes. However, method based on liquid-solid reactions, such as the auto-combustion synthesis method, are developed in order to synthesize homogeneous perovskite of pure single-phase with nanostructured crystallites and high specific surface area. The sensor performances improvement, such as higher sensitivity, lower detection limit, lower operating temperature and faster response, can be obtained thanks to the usage of nanodimensional materials, because of the large specific surface areas, which increase the interaction between the sensor surface and the surrounding gases, the high porosity, which allows the gas target penetration inside the sensing layer, and the useful thickness of the depletion layer, which promote the detection of small resistance changes [138]. The auto-combustion synthesis process comprises three main steps: dissolution (*Figure 24.a*), desiccation (*Figure 24.b*) and combustion (*Figure 24.c*). During the first step,

aqueous solutions of metal precursors are prepared, by mixing nitrate salts of desired metals, such as lanthanum ($La(NO_3)_3 \cdot 6H_2O$), iron ($Fe(NO_3)_3 \cdot 9H_2O$) and cobalt ($Co(NO_3)_2 \cdot 6H_2O$), and titanium butoxide ($Ti(C_4H_9O)_4$) maintaining molar ratio at 1:1, according to the desired perovskite stoichiometry. Moreover, proper amounts of ammonium nitrate (NH_4NO_3), citric acid (CA) monohydrate ($C_6H_8O_7 \cdot H_20$) and ammonia are added to the solution:

- the former acts as oxidizer agent;
- the citric acid ions act as fuel, as well as the titanium butoxide ions, and as chelating agent for metal ions;
- the latter is used to adjust pH and solution acidity, and to promote the metal complexations by undissociated form of citric acid and to prevent the formation of metal hydroxides.

The second step is performed at low temperature of 100 °C and under stirring condition. It includes the evaporation of the solvent and the polymerization of the citrate ions, which are multifunctional crosslinking agents leading to a high viscous gel. During the condensation reaction between monomer units, the produced water is continuously removed in order to have a completely dried hyper-branched polymeric material. Increasing the temperature up to about 200 °C, the ignition points of the explosive mixtures are reached, developing the auto-combustion synthesis whose generated heat leads to formation of very porous nanopowders of LaFeO3 perovskites (*Figure 24.d*), since the combustion step takes few seconds preventing in this way the particle growth and the sintering process. The obtained powders were finally calcined at a temperature of 800 °C for 4 hours, in order to obtain very fine samples of perovskites.

Figure 24. Steps of the auto-combustion synthesis: a) initial solution; b) desiccated branched polymer; c) flame combustion; d) synthesized powder.

The different obtained powders were characterized by means of X-Ray Diffraction technique, in order to evaluate their phase, crystalline structure, crystallite's size and lattice parameter. The instrument used was a Rigaku Miniflex diffractometer with Cu-K_α radiation, scan rate of 0.1 °/min and scanning from 2θ=30 ° to 2θ=80°. Samples were also subjected to morphology characterization and determination of the average grain size, by means of Scanning Electron Microscope (SEM) analyses, using a Gemini LEO 1530, FEG type (Field Emission Gun), which has an acceleration voltage of 0.2-30 kV and a resolution of 1.0-5.0 nm. Even Energy Dispersive X-ray Spectroscopy (EDS) was performed in order to evaluate the effective composition of the materials.

The synthesized powders were then arranged as sensing materials for chemoresistive sensors. Appropriate pastes of synthesized samples were deposited on them, mainly prepared by mixing an organic vehicle and the inorganic perovskite in order to facilitate the dispersion of the functional material in the right viscosity, shape and strength. The presence of the organic vehicle does not affect sensor response, since it is successively removed with a burnout step [230,231]: it was prepared by mixing a solution of α-terpineol and 2-propanol with ethyl cellulose resins in the ratio of 12:1; afterward, it was mixed to the obtained powders in the ratio of 30:70, with a proper amount of 2-propanol in order to achieve a better dispersion of the active material. The obtained pastes were then calcined for 1 hour at 500 °C [232–234], in order to remove all the organic binders or polymeric viscosifier traces and to promote the particles electromechanical bonding.

The test-rig used for the evaluation of gas sensing performances of the synthesized samples is shown in *Figure 25*. It is composed by a furnace with temperature control containing a stainless steel or quartz cell fed with a constant gas flow controlled by proper mass flow controller (MFC). Gas sensors inside the cell were composed by Au interdigitated electrodes, sprinkled with the synthesized sensing materials (*Figure 25.b*) and linked by Au nanowires to a multimeter for the evaluation of the resistance changes. Au interdigitate electrodes on alumina supports were used for maximizing electrical responses. The entire apparatus is controlled by a measurement and automation system via LabVIEW® software, used for its regulation and the results collection. Tests were carried out at ambient pressure, with a constant flow of inert nitrogen and proper amount of the studied analyte. The flow rate in the chamber was of 100 Nml/min. The entire system is capable to operate at high

temperatures, up to about 1000 °C. This kind of test methodology can be defined as a “flow-through” method, not yet included in standard testing protocols, ISO 26142 and UL 2075 [235,236], which prefer large volume test chambers. However, feedback from stakeholders such as sensor manufacturers and end-users indicate that chamber test methods are often too slow and expensive for routine assessment. Flow-through test methods, instead, are an efficient, cost-effective alternative for sensors performance assessment, since it allows to test a large number of sensors simultaneously and with reduced time. In addition, researches from JRC and NREL laboratories demonstrated the validity of this kind of methodology [237,238]. Its utilization is, hence, perfectly justified.

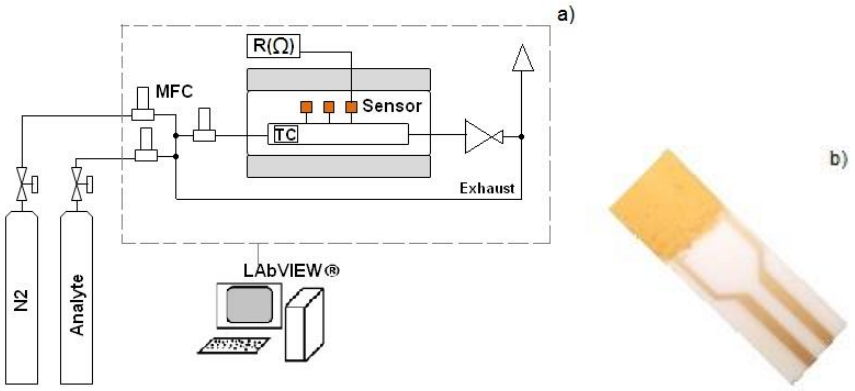

Figure 25. Experimental apparatus (a) for testing gas sensors (b)

For some studies, in particular the multivariate process, chemometric analysis was performed, since it is an useful science for studying multivariate systems and developing models with predictive ability [107,239,240]. Chemometrics involves two steps: experimental design and multivariate data analysis. The initial design of experiments (DoE) is used for the experimentation planning and for getting the maximum amount of information with the minimum number of experiments, basically by changing all relevant factors simultaneously over a set of planned experiments. With the successive multivariate data analysis step, the results are then connected and interpreted by means of the relative mathematical model: a polynomial function is used for the interpolation of the results and represents a good description of the relationship between the experimental variables and the responses within a limited experimental domain. More information on the specific multivariate analyses is reported in the following dedicated section.

Synthesis optimization

Three synthesis parameters were taken into account for materials preparation: is the pH level of the precursor mixture, the citric acid to metal ions ratio (CA/M) and the Φ parameter. The former is a crucial synthesis parameter, since it can affect the citric acid dissociation and the relative metal ions complexation, as well as the metal-hydroxide formation. Metal ions complexation is affected also by CA/M ratio and then it is also considered in the analysis. Finally, for the evaluation of the combustion stoichiometric condition, it is possible to refer to the Φ parameter. It is defined [241] as

$$\Phi = \frac{\varphi}{(1+\varphi)} \quad \textbf{(4.1)}$$

that is the normalization of the equivalence ratio ϕ, which is related to the fuel to oxidizer ratio (F/O) as

$$\varphi = \frac{{}^{fuel}/_{oxidizer}}{\left({}^{fuel}/_{oxidizer}\right)_{st}} \quad \textbf{(4.2)}$$

The normalized equivalence ratio Φ can assume values between 0 and 1: stoichiometric conditions occur for Φ=0.5 while lower and higher values represent respectively lean fuel and rich fuel conditions. The fuel to oxidizer ratio plays a crucial role in a combustion synthesis, since it highly affects the flame temperature and consequently the final product characteristics [127,242].

For the evaluation of Φ parameter values, the global synthesis reaction, where NO_x production is disregarded, was considered:

$$aLa^{3+}+bFe^{3+}+cTi^{4+}+dCo^{2+}+eC_4H_9O^{-}+fC_6H_5O_7^{3-}+gNO^{-} \rightarrow$$

$$hLaTi_xCo_zFe_{(1-z-x)}O_3+iH_20+lCO_2+mN_2 \quad \textbf{(4.3)}$$

Φ parameter values were then determined through the balancing of this redox reaction, by considering the electron transfer from the oxidizing species NO^{3-} to the reducing species $C_4H_9O^{-}$ and $C_6H_5O_7^{3-}$.

As regards the evaluation of the pH level of the mixture, instead, a preliminary analysis has been carried out. The main chemical species in the solutions at different pH values were

theoretically calculated, in order to quickly evaluate the best solution acidity. The dissociation of the citric acid was evaluated by considering aqueous solutions with only citric acid ions. Four different species are formed, H_4cit, H_3cit^-, H_2cit^{2-} and $Hcit^{3-}$, whose respectively relative concentrations α_0, α_1, α_2 and α_3 are defined as the species concentration amount respect to the total concentration of citric acid in the solution: the complete dissociation of citric acid occurs at pH higher than 7, since in these cases the citrate free $Hcit^{3-}$ is the predominant form, and in the same range metal-hydroxide formation is prevented [243]. The determination of citric acid dissociation was also useful for the calculation of the metal-citrate and metal-hydroxide complexes, carried out by considering aqueous solutions of citric acid with only La ions or Fe ions respectively. *Table 20* summarizes all the complexes considered on the basis of the work of Martell and Smith [244,245] and Lee and Fang [246], together with their relative concentrations α_i and reaction equilibrium constants $k_{\alpha i}$.

Reaction	Relative Concentration	Equilibrium constant	Absolute Concentration
-	$\alpha_4=[La^{3+}]/C_{t,La}$	-	$[La^{3+}]$
$La^{3+}+Hcit^{3-}\rightarrow La(Hcit)$	$\alpha_5=[La(Hcit)]/C_{t,La}$	$k_{\alpha5}=4.3\cdot10^{7}$ [244]	$[La(Hcit)]=[La^{3+}]k_{\alpha5}\alpha_3C_{t,CA}$
$La^{3+}+2Hcit^{3-}\rightarrow[La(Hcit)_2]^{3-}$	$\alpha_6=[[La(Hcit)_2]^{3-}]/C_{t,La}$	$k_{\alpha6}=1.6\cdot10^{10}$ [244]	$[[La(Hcit)_2]^{3-}]=[La^{3+}]k_{\alpha6}(\alpha_3C_{t,CA})^2$
$La(Hcit)+H_2cit^{2-}\rightarrow[LaH(cit)_2]^{2-}$	$\alpha_7=[[LaH(cit)_2]^{2-}]/C_{t,La}$	$k_{\alpha7}=1.6\cdot10^{2}$ [244]	$[[LaH(cit)_2]^{2-}]=[La^{3+}]k_{\alpha5}k_{\alpha7}\alpha_3\alpha_2(C_{t,CA})^2$
$La^{3+}+OH^-\rightarrow[La(OH)]^{2+}$	$\alpha_8=[[La(OH)]^{2+}]/C_{t,La}$	$k_{\alpha8}=3.2\cdot10^{5}$ [245]	$[[La(OH)]^{2+}]=[La^{3+}]k_{\alpha8}[OH^-]$
$2La^{3+}+OH^-\rightarrow[La_2(OH)]^{5+}$	$\alpha_9=2[[La_2(OH)]^{5+}]/C_{t,La}$	$k_{\alpha9}=1.6\cdot10^{4}$ [245]	$[[La_2(OH)]^{5+}]=[La^{3+}]^2k_{\alpha9}[OH^-]$
$5La^{3+}+9OH^-\rightarrow[La_5(OH)_9]^{6+}$	$\alpha_{10}=5[[La_5(OH)_9]^{6+}]/C_{t,La}$	$k_{\alpha10}=6.3\cdot10^{54}$ [245]	$[[La_5(OH)_9]^{6+}]=[La^{3+}]^5k_{\alpha10}[OH^-]^9$
-	$\alpha_{11}=[Fe^{3+}]/C_{t,Fe}$	-	$[Fe^{3+}]$
$Fe^{3+}+Hcit^{3-}\rightarrow Fe(Hcit)$	$\alpha_{12}=[Fe(Hcit)]/C_{t,Fe}$	$k_{\alpha12}=3.2\cdot10^{11}$ [244]	$[Fe(Hcit)]=[Fe^{3+}]k_{\alpha12}\alpha_3C_{t,CA}$
$Fe^{3+}+H_2cit^{2-}\rightarrow[Fe(H_2cit)]^{+}$	$\alpha_{13}=[[Fe(H_2cit)]^{+}]/C_{t,Fe}$	$k_{\alpha13}=5.0\cdot10^{6}$ [246]	$[[Fe(H_2cit)]^{+}]=[Fe^{3+}]k_{\alpha13}\alpha_2C_{t,CA}$
$Fe^{3+}+OH^-\rightarrow[Fe(OH)]^{2+}$	$\alpha_{14}=[[Fe(OH)]^{2+}]/C_{t,Fe}$	$k_{\alpha14}=6.5\cdot10^{11}$ [245]	$[[Fe(OH)]^{2+}]=[Fe^{3+}]k_{\alpha14}[OH^-]$
$Fe^{3+}+2OH^-\rightarrow[Fe(OH)_2]^{+}$	$\alpha_{15}=[[Fe(OH)_2]^{+}]/C_{t,Fe}$	$k_{\alpha15}=2.0\cdot10^{22}$ [245]	$[[Fe(OH)_2]^{+}]=[Fe^{3+}]k_{\alpha15}[OH^-]^2$
$Fe^{3+}+4OH^-\rightarrow[Fe(OH)_4]^{-}$	$\alpha_{16}=[[Fe(OH)_4]^{-}]/C_{t,Fe}$	$k_{\alpha16}=2.5\cdot10^{34}$ [245]	$[[Fe(OH)_4]^{-}]=[Fe^{3+}]k_{\alpha16}[OH^-]^4$
$2Fe^{3+}+2OH^-\rightarrow[Fe_2(OH)_2]^{4+}$	$\alpha_{17}=2[[Fe_2(OH)_2]^{4+}]/C_{t,Fe}$	$k_{\alpha17}=1.3\cdot10^{25}$ [245]	$[[Fe_2(OH)_2]^{4+}]=[Fe^{3+}]^2k_{\alpha17}[OH^-]^2$
$3Fe^{3+}+4OH^-\rightarrow[Fe_3(OH)_4]^{5+}$	$\alpha_{18}=3[[Fe_3(OH)_4]^{5+}]/C_{t,Fe}$	$k_{\alpha18}=5.0\cdot10^{49}$	$[[Fe_3(OH)_4]^{5+}]=[Fe^{3+}]^3k_{\alpha18}[OH^-]^4$

Table 20. Metal-citrate and -hydroxide complexes of La^{3+} and Fe^{3+}

For the total concentrations of citric acid, lanthanum and iron, values close to the real operating conditions are assumed:

$$1.0M=C_{t,CA}=[H_4cit]+[H_3cit^{-}]+[H_2cit^{2-}]+[Hcit^{3-}] \quad \textbf{(4.4)}$$

$$0.1M=C_{t,La}=[La^{3+}]+[La(Hcit)]+[[La(Hcit)_2]^{3-}]+[[LaH(cit)_2]^{2-}]+$$
$$[[La(OH)]^{2+}]+[[La_2(OH)]^{5+}]+[[La_5(OH)_9]^{6+}] \quad \textbf{(4.5)}$$

$$0.1M=C_{t,Fe}=[Fe^{3+}]+[Fe(Hcit)]+[[Fe(H_2cit)]^{+}]+[[Fe(OH)]^{2+}]+$$
$$[[Fe(OH)_2]^{+}]+[[Fe(OH)_4]^{-}]+ [[Fe_2(OH)_2]^{4+}]+[[Fe_3(OH)_4]^{5+}] \quad \textbf{(4.6)}$$

As showed by *Figure 26.a*, La^{3+} ions [247] are completely converted in metal-citrate complexes for pH>3 and no La-hydroxides are formed in the entire pH range considered. As regards Fe^{3+} ions [229], instead, the complete complexation occurs with pH=4-8, where the only complex present is $[Fe(H_2cit)]^{+}$, but in the same time the hydroxides $[Fe(OH)_2]^{+}$ and $[Fe(OH)_4]^{-}$ are generated when the solution pH level overcomes 8 (*Figure 26.b*). In the case of $LaTi_xFe_{1-x}O_3$, the results of the work by Collins et al. [248] reveals that the fully deprotonated form $[Ti(cit)_3]^{8-}$ reaches its maximum value at pH=7, where even the mixed species $[Ti(OH)_2(cit)_2]^{6-}$ starts to appear, being the predominant complex as the solution becomes more basic (pH>8).

The determination of the appropriate pH is also useful for the evaluation of the citric acid to metal ions ratio CA/M. In fact, at pH=7 the metal citrate complexes are $[La(Hcit)_2]^{3-}$ and $[LaH(cit)_2]^{2-}$, which have both citrate/metal ratio of 2:1, and $Fe(Hcit)$, with ratio 1:1. Analysing the case of $LaTi_xFe_{1-x}O_3$, also $[Ti(cit)_3]^{8-}$ and $[Ti(OH)_2(cit)_2]^{6-}$ have to be considered, whose citrate/metal ratio is 3:1 and 2:1 respectively. Hence, in this case, the CA/M stoichiometric ratio can vary from 1.5 to 2.5, depending on the $LaTi_xFe_{1-x}O_3$ stoichiometry and the complexes considered. In fact, since the perovskite stoichiometry, the mole of all metal ions is $n_M=n_{La}+n_{Ti}+n_{Fe}=n+xn+(1-x)n=2n$, where $n_{La}=n$, $n_{Fe}=xn$, $n_{Ti}=(1-x)n$ and thus the mole of total citric acid necessary for complexing the metal ions is

$$n_{t,CA1}=2n_{La}+2n_{Ti}+n_{Fe}=n_M+xn_M+0.5(1-x)n_M=(1.5+0.5x)n_M \quad \textbf{(4.7)}$$

$$n_{t,CA2}=2n_{La}+3n_{Ti}+n_{Fe}=n_M+1.5xn_M+0.5(1-x)n_M=(1.5+x)n_M \quad \textbf{(4.8)}$$

Hence, for *x* that varies between 0 and 1, $n_{t,CA1}/n_M$=1.5-2 and $n_{t,CA2}/n_M$=1.5-2.5.

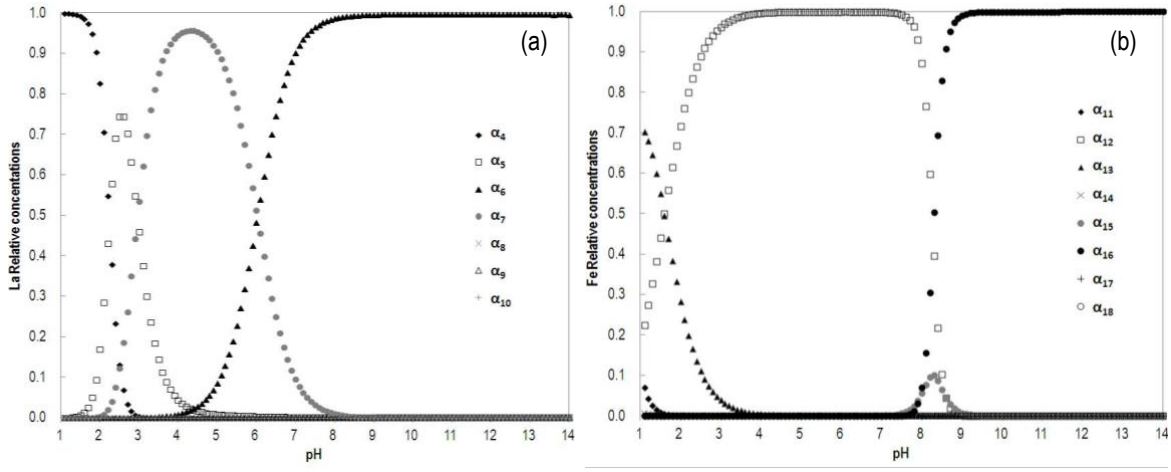

Figure 26. Relative concentrations of lanthanum (a) and iron (b) metal-citrate and -hydroxide complexes as a function of pH

The working principle of materials gas sensing is based on the interaction (electrons exchange) between the gas target and the sensing material, which consequently changes its resistance. Sensors quality is, thus, strongly influenced by materials properties, in terms of porosity, specific surface area and electrical characteristics. These characteristics are, in turn, strongly influenced by materials preparation method and conditions [249]. Therefore, in order to investigate how synthesis conditions affect powders properties and quality, a chemometric analysis was carried out on $LaFeO_3$ perovskite material [250]. A full factorial experimental design with two factors and three levels was used, addressing the Central Composite Design: the relative experimental design is thus composed by ten experiments (the central experiment was carried out twice to minimize the statistical error of the model), arranged geometrically as a body-centred square (*Figure 27*).

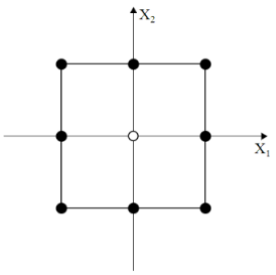

Figure 27. Geometrical representation of DoE for synthesis optimization

Ten different sample of $LaFeO_3$ perovskite were then synthesized, by varying the synthesis condition according to the specific Design of Experiments (DoE). The independent synthesis parameters considered were CA/M and Φ parameter. It was chosen to study CA/M ratios between 1 and 2 and Φ values from 0.25 to 0.75. As regards solution acidity, instead, it was chosen to fix pH=4 for all the sample, since both needs of metal complexation and avoiding metal hydroxides formations are satisfied at this level, as previously showed: Fe^{3+} reaches complete complexation with citrate pH higher than 4 and no hydroxides precipitation occurs with pH<8; La^{3+} is fully complexed at a pH value higher than 3. Multivariate data analysis based on a non-linear multiple regression was also performed. Equation 4.9 shows the corresponding polynomial function.

$$Y = b_0 + b_1X_1 + b_2X_2 + b_{12}X_1X_2 + b_{11}{X_1}^2 + b_{22}{X_2}^2 \qquad \textbf{(4.9)}$$

Y is the response related to the obtained powders properties and X_1 and X_2 are surrogate variables, relative to the real experimental variables considered, that is CA/M and Φ respectively: the surrogate variables were normalized from -1 to +1, corresponding respectively to the lowest and highest value of the experimental variables. The influence of synthesis parameters on powders properties is connected with b_{ij} coefficients; in particular, b_0 is a constant, b_1 and b_2 represent the main direct effects of variable X_1 and X_2, b_{11} and b_{22} show the non-linear relationship between the responses and the experimental variables and, finally, the indirect effects produced by cross-interaction between X_1 and X_2 are represented by b_{12} coefficient. The powders properties chosen for the study were crystallites size (D_c) and average grain size (D_g). Summary of different synthesis conditions for the different experiments carried out are listed in *Table 21*, which reports real experimental variables and relative values (experimental matrix), surrogated variables (model matrix) and also measured and calculated values of the responses. The central experiment was carried out twice, in order to minimize statistical errors of the chemometric model.

	Model Matrix		*Experimental Matrix*		*Responses*	
	X_1	***X_2***	***CA/M***	***Φ***	***D_c (nm)***	***D_g (nm)***
exp 1	-1	-1	1.00	0.25	-	-
exp 2	1	-1	2.00	0.25	39.39	55

exp 3	-1	1	1.00	0.75	30.85	70
exp 4	1	1	2.00	0.75	19.69	60
exp 5	-1	0	1.00	0.50	45.51	155
exp 6	1	0	2.00	0.50	44.70	205
exp 7	0	-1	1.50	0.25	38.46	60
exp 8	0	1	1.50	0.75	30.51	65
exp 9	0	0	1.50	0.50	46.19	170
exp 10	0	0	1.50	0.50	47.52	170

Table 21. Chemometric analysis for synthesis optimization

Some differences occurred during the various synthesis conductions. In particular, for different Φ parameter, different temperature and type of combustion were involved: lean or rich fuel combustion conditions lead to smouldering propagation, while for stoichiometric combustions flame propagation occurs; the former involves relatively lower combustion temperature and higher reaction rate respect to the latter case.

Also the characterization analysis revealed the differences between the various obtained samples. *Figure 28* shows XRD patterns of the different powders (prepared eliminating the final step of calcination), after being subjected to redefining processes, such as pattern's smoothing with Savitzky method, background optimization with Sonnevelt method and $K_{\alpha 2}$ radiation effects elimination with Rachinger method. All the obtained sample are single-component material of $LaFeO_3$ perovskite oxides, except experiment 1, whose spectra is not comparable with the reference pattern and which reported amorphous phase. Crystalline structured powders, on the contrary, have crystal's primitive lattice of orthorhombic system belonging to Pbnm space group, and a tolerance factor *t* of 0.83, where the Goldschmidt factor *t* [168] is defined as

$$t = \frac{R_{La3+} + R_{O2-}}{(R_{Fe3+} + R_{O2-})\sqrt{2}} \qquad \textbf{(4.10)}$$

and the ionic radii R_{La3+}, R_{Fe3+} and R_{O2-} are 1.36Å, 0.55Å and 1.4Å respectively. In particular, perovskites with tolerance factors close to 1 are supposed to have an ideal cubic structure, otherwise the cubic system distorts towards orthorhombic, rhombohedral and tetragonal structures; for $0.7<t<1.1$, instead, perovskites have no more stable structure.

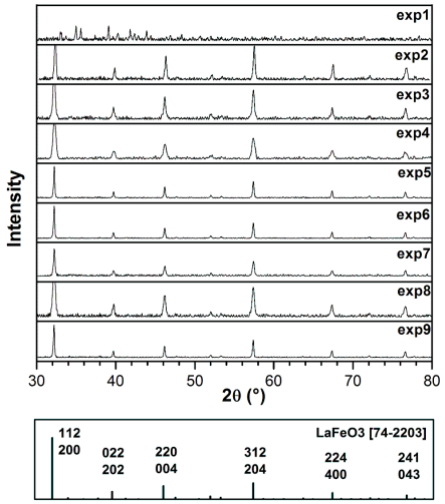

Figure 28. XRD patterns of the obtained powders and reference pattern of $LaFeO_3$

X-ray diffraction patterns were useful also to evaluate crystallite's diameter. Indeed, the full width at half maximum (FWHM) of every peak of the spectra is affected by crystallite size broadening (β_{hkl}[size]), as well as by lattice strain broadening (β_{hkl}[strain]). Nevertheless, it is possible to assume the lattice strain effects on peak broadening very negligible [228] and, thus ascribe it only to crystallite size effects. Hence, crystallite sizes were estimated with Scherrer equation [251]:

$$\beta_{hkl}[size] = \frac{K\lambda}{D_{hkl}cos\theta_{hkl}} \quad \textbf{(4.11)}$$

where D_{hkl} is the average crystallites size in nanometers along the direction normal to the diffraction plane (hkl), K is the shape factor equal to 0.9, λ is the x-ray wavelength of Cu-K_α equal to 0.1540593 nm and ϑ_{hkl} is the Bragg angle in radians for the crystallographic plane (hkl).

Average crystallites sizes of all obtained sample are listed in *Table 21*: note that the experiment 1 reports no value for crystallites diameter, since the relative sample have not a crystalline structure. It is possible to assume, in a first approximation, that lean fuel combustion synthesis combined with a not in excess concentration of citric acid respect to the one of metal ions should be avoided. For the same reasons, experiment 1 has not been taken into account for the multivariate data analysis, which was carried out considering always all factor, all cross-terms and all square terms, according to equation 4.9. The influence of all factors on powders crystallites size is demonstrated in *Figure 29.a*, where every b_i coefficient is displayed as a bar correlated with its relative statistical significance,

which is defined by the *p* parameter, whose limit was set to 0.1: it was assumed that only coefficients with $p<0.1$ are statistically significant.

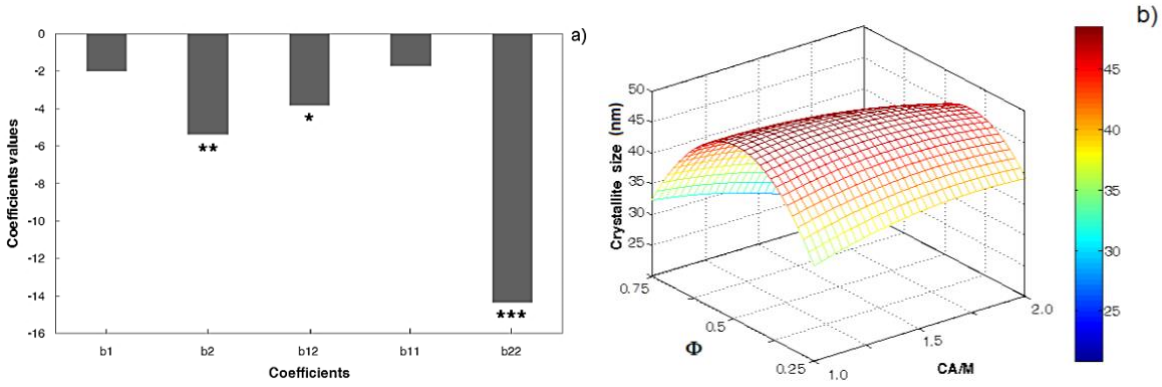

Figure 29. a) Coefficients of the mathematical model from multiple regression analysis and relative statistical significance levels: "no star" indicates no statistically significance, "one star" p < 0.1, "two stars" p < 0.05, "three stars" p < 0.005

b) Response surface for the effect of CA/M ratio and Φ parameter on average crystallites size

Figure 29.a shows that neither b_1 nor b_{11} are statistically significant and, thus, it can be assumed that crystallites size is not affected by CA/M ratio, neither with a linear nor with a quadratic correlation. On the contrary, b_2 and b_{22} coefficients have $p=0.02$ and $p=0.003$ respectively, which states that Φ is the only parameter who influences crystallites dimension and mostly by a quadratic relationship. In particular, in this case the influence of citric acid to metal ions ratio on the crystallization phase is minimized by more affecting synthesis conditions, even if it is crucial for the metal complexation and, thus, for the perovskite formation. Nevertheless, the significance of the cross-term b_{12} demonstrates that the two considered factors are correlated each other, being the amount of citric acid affected both from CA/M and fuel to oxidizer ratio and, thus, from Φ parameter. All of these considerations are confirmed by the response surface plot of *Figure 29.b*, where the crystallites size trend depending on CA/M ratio variations is quite constant, while the relationship between D_c and Φ is quadratic and bell-shaped. Indeed, crystallites growth is highly affected by reaction temperature, which is in turn correlated by Φ parameter, as observed previously: the carried out combustion synthesis with Φ=0.25 and Φ=0.75 developed smouldering propagation and lower combustion temperature, while flame propagation occurred for synthesis with Φ=0.5, which showed higher flame temperature.

SEM analysis for the morphology phase determination is showed in *Figure 30*. Also SEM images confirm that experiment 1 has no crystalline structure but an amorphous phase, while all the other samples are crystalline structured perovskites, even if not all of them have homogenous morphology, such as experiment 2, 3 and 7. Average grain sizes of obtained sample evaluated from SEM images are listed in *Table 21*: even for D_g of sample 1 there are no values, due to its amorphous phase, and even for the relative multivariate data analysis experiment 1 has not been taken into account.

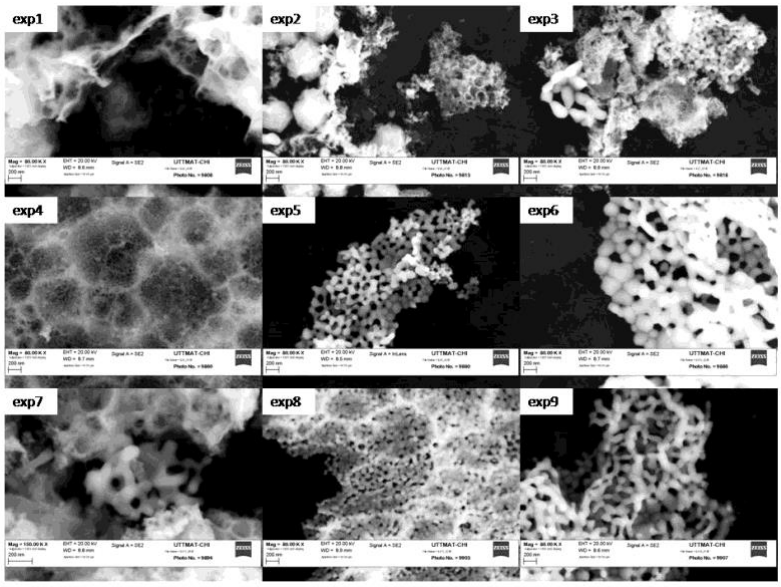

Figure 30. SEM images of different obtained powders of $LaFeO_3$

The bar chart of b_i coefficient related to D_g is displayed in *Figure 31.a*: just like the one related to D_c, the statistical significance limit was set to p<0.005. The only statistically significant coefficient is b_{22}, with p=0.003. Hence, CA/M effects on average grain size of the obtained powders are very negligible and the only parameter who has influence is Φ, by a quadratic relationship. Indeed, grains growth processes are mostly regulated by reaction temperature and, consequently, by Φ parameter: in particular, high combustion temperatures lead to sintering processes and, thus, to bigger grains. The relative response surface plot confirms these evaluations, showing a bell-shaped relationship between D_g and Φ and, on the contrary, a quite constant correlation with CA/M. Therefore, synthesis with flame propagation and stoichiometric conditions generate powders composed by larger particles.

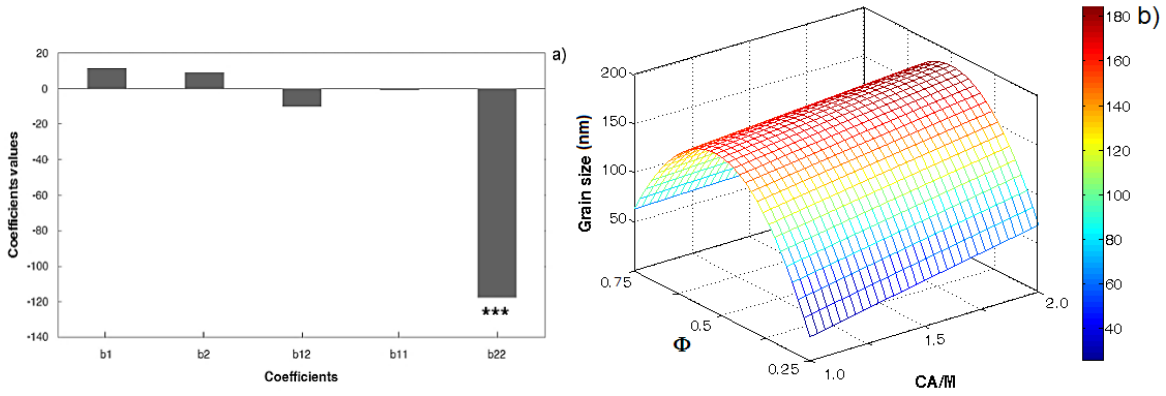

Figure 31. a) Coefficients of the mathematical model from multiple regression analysis and relative statistical significance levels: "no star" indicates no statistically significance, "three stars" p < 0.005

b) Response surface for the effect of CA/M ratio and Φ parameter on average grain size

Summarizing, it was obtained that citric acid to metal ions molar ratio have no influence on the average crystallites and grains size, even if it is important for the metal complexation and, thus, for the perovskite formation, since its effect is minimized respect to the other parameters. The combination of CA/M ratio with the fuel to oxidizer ratio could be, instead, quite relevant, mostly for values as CA/M≤1, which could generate amorphous materials if combined with lean fuel conditions. The Φ parameter, on the contrary, that is an index of the fuel to oxidizer ratio, highly affects crystallites and grains size, and both with a bell-shaped relationship. Therefore, approaching the stoichiometric conditions, flame propagation and greater reaction temperature occur, promoting crystallites growth and sintering of the grains, affecting in turn powders porosity.

Gas sensing tests

Once having deeply analysing the materials preparation method and its best conditions and parameters, evaluation of gas sensing performances of $LaFeO_3$ based perovskites have been carried out. In particular, two perovskite materials were synthesized: $LaTi_{0.4}Fe_{0.6}O_3$ and $LaFeO_3$. The aim was to evaluate performances in the sensing of typical gases and contaminants of fuel cells and gasification systems of lanthanum ferrite oxide with partial substitution on B cations, specifically with titanium ions, which are supposed to increase the thermal stability in reducing atmosphere and at high temperatures [252].

Perovskites of $LaTi_xFe_{1-x}O_3$ (x=0 and 0.4) were, thus, prepared as sensing materials for chemoresistive sensors by means of auto-combustion synthesis technique, via citrate-nitrate method. Synthesis conditions were determined on the basis of considerations previously presented. As regards Φ parameters, stoichiometric conditions have to be avoided since they promote high flame temperatures that lead to crystallites growth and grain sintering, both affecting material properties; moreover, the suitable perovskite formation occurs in the range of $0.4<\Phi<0.6$ [243]. Therefore, solutions with $\Phi=0.45$ were prepared, in order to assure the right perovskite formation and to develop surely complete and safer combustions (rich-fuel combustion), thanks to the further advantage provided by the excess of oxidizer. On the other hand, solution acidity was set at pH=7, since it is the most suitable for enhancing citric acid dissociation and metal complexation and avoiding metal-hydroxides formation. Finally, in order to assure the complete metal complexation, CA/M ratio was set at 2.5, working with a slight excess of citric acid respect to the stoichiometric conditions, since in this case $n_{t,CA1}/n_M$=1.5-1.7 and $n_{t,CA2}/n_M$=1.5-1.9. X-Ray Diffraction analysis conducted on the synthesized powders, confirmed the effectiveness of the auto-combustion synthesis method and conditions. The XRD spectra shown in *Figure 32* demonstrate that all the samples were successfully very fine powders of $LaTi_xFe_{1-x}O_3$ perovskite-type oxides, being effectively single-component materials with no impurity phases generation. Moreover, *Figure 32.b* shows that titanium ions were successfully integrated into the perovskite structure without introducing any stress or deformation to the crystalline lattice.

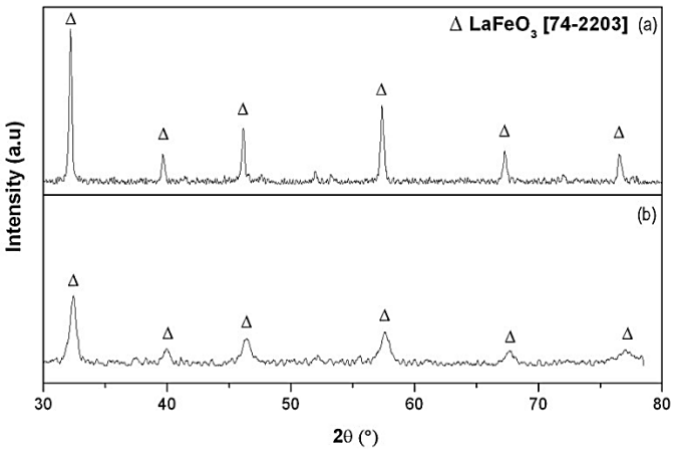

Figure 32. XRD patterns of $LaFeO_3$ (a) and $LaTi_{0.4}Fe_{0.6}O_3$ (b)

Obtained perovskites of $LaTi_xFe_{1-x}O_3$ were tested in a temperature range of 400-600 °C for three different analytes and with different concentrations (see *Table 22*). The experimental apparatus used was that showed in "*Materials preparation"* paragraph, without the measurement and automation system via LabVIEW®. It was chosen to investigate these ranges of concentration level in order to have primary information on the materials responses to the target analyte, trying to avoid at the same time possible materials damaging due to high concentration level. Furthermore, these concentration levels are in the range of those tolerated by some of the devices or permitted as environmental emissions for the power systems investigated in the previous analyses.

Analyte	***Concentration X_i (ppm)***				
CO	20	50	100	150	
H_2	1000	2000	3000	4000	5000
H_2S	1	2	3	4	5

Table 22. Analytes concentrations used in gas sensing tests

The sensors responses to the presence of target analytes were evaluated by means of its sensitivity (*S*), defined as:

$$S = \frac{|R_0 - R_a|}{R_0} \quad \textbf{(4.12)}$$

where R_0 is the sensor response baseline to pure N_2 and R_a is that to analytes flow. Sensors responses were estimated as changes in resistance of the perovskite sensing materials.

The gas sensing properties of $LaTi_{0.4}Fe_{0.6}O_3$ (LTFO) sensor to CO, H_2 and H_2S were evaluated at different concentrations and different temperatures. The influence of iron partial substitution with titanium ions in the sensing material structure was also investigated, by the comparison of $LaTi_{0.4}Fe_{0.6}O_3$ and $LaFeO_3$ (LFO) sensing properties. *Figure 33* shows the resistance response to successive and increasing CO exposures for both the sensing materials considered.

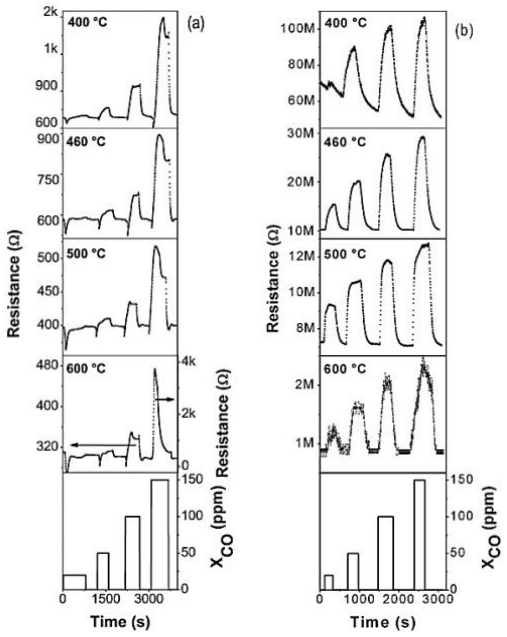

Figure 33. Resistance measurements on $LaFeO_3$ (a) and $LaTi_{0.4}Fe_{0.6}O_3$ (b) sensors at different temperatures for successive CO exposures

LTFO sensor provided a stable and clear response signal in all cases, revealing pure p-type behaviour: the reducing action of carbon monoxide produced an increase of the resistance level up to a maximum and constant value for all the temperatures and concentrations considered. In the case of p-type semiconductor, in fact, exposures to reducing gases as CO and H_2 cause the increasing of resistance, while the inverse effect is generated in presence of oxidizing analytes, as explained in the previous chapter. Moreover, the reversibility properties of the sensor were very high: materials electrical characteristics were recovered after each test and even the resistance baseline, which reported a slight drift only at 400 °C when the experimental procedure was affected by some test problems. Even the LFO sensor displayed an almost absent drift, and, consequently a quite high chemical stability and reproducibility [115,253]. On the contrary, the LFO response signal resulted to be more intricate than that of LTFO, since, in all cases, the resistance had an initial decrease as the CO was injected on the perovskite oxide before rising up and, in addition, pure p-type behaviour was not occurred. With concentrations of 100-150 ppm, in fact, the material's resistance had an initial rise up to a maximum and then a fast decrease until the final stabilization while carbon monoxide is still present.

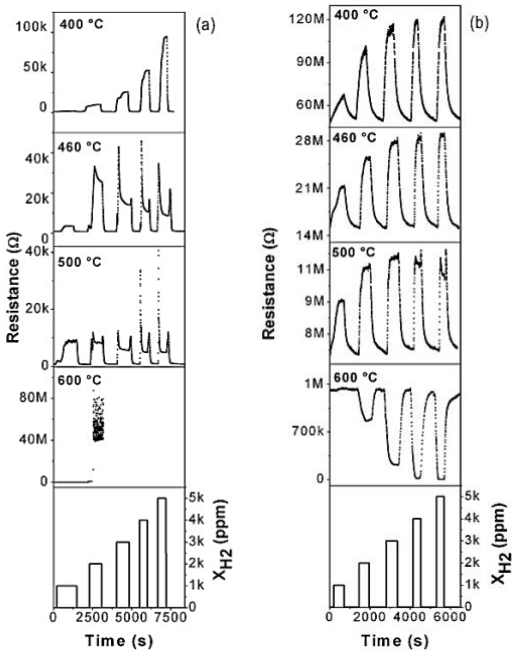

Figure 34. Resistance measurements on $LaFeO_3$ (a) and $LaTi_{0.4}Fe_{0.6}O_3$ (b) sensors at different temperatures for successive H_2 exposures

Similar trends were registered even with exposures to H_2, as shown in *Figure 34*. In addition, in presence of hydrogen also LTFO sensor revealed different behaviour at different temperatures and concentrations. In particular, $LaTi_{0.4}Fe_{0.6}O_3$ operated as a pure p-type semiconductor only at 400-460 °C, while at 600 °C the n-type behaviour occurred since the hydrogen reducing action generated a clear resistance decrease; at 500 °C, instead, higher concentrations of H_2 resulted in the ambiguous behaviour of a first growth and a successive reduction of the material resistance.

These evaluations revealed that $LaFeO_3$, as other semiconducting oxide, cannot be classified merely as n- or p-type, but is characterized by a dual behaviour which causes a transition of its conductive properties [254–256], clearly demonstrated by LTFO sensor exposed to hydrogen atmosphere (*Figure 35*). At 500 °C, for $p_{H2}<10^{-0.5}$, the material is p-type since holes and cation vacancies are the dominating charge carriers and defects; the n-type region occurs for $p_{H2}>10^{-0.5}$, when electrons and oxygen vacancies become predominant. In fact, in the cases of interaction between the material and the reducing gases, the latter are oxidized by surface oxygen ions, addressing the reaction

$$R+O_o^x \rightarrow RO+V_o^{\cdot\cdot}+2e^- \qquad \textbf{(4.13)}$$

where *R* is the reducing gas, O_o^x is oxygen with neutral charge sitting on the perovskite lattice site, $V_o^{\cdot\cdot}$ is oxygen vacancy with double positive charge. As soon as gases interact with samples in "low concentration", start to generate free electrons that can return to the valence band, decreasing progressively the holes' concentration: the dominant free charge carriers are still holes and it is possible to note a decrease of conductivity with increasing of gas concentration. This phenomenon persists as long as the decrease in holes' concentration remains more important than the increase in electrons concentration. Nevertheless, when the concentration of reducing gases becomes "high", this situation is overturned and the electrons starts to become the dominant surface charge carriers, displaying an increase of the conductivity as the concentration is increased [257,258]. It is possible to note that, being in the range of partial pressure close to minima in total conductivity, the slopes of p-type and n-type conductivity are around ±1/4, while the ionic conductivity σ_i is independent of the partial pressure variations [259]. The ambiguous behaviours, occurred even for $LaFeO_3$, results from the operation around the minimum in the conductivity trend and a low diffusion coefficient, which reduces the diffusion rate of the reducing gases into the material and extends the response times.

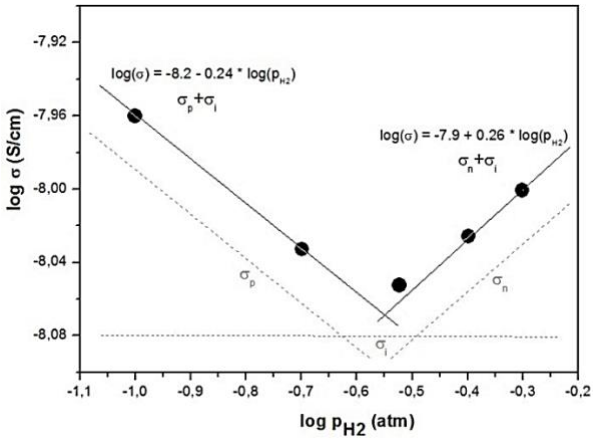

Figure 35. Transition from p- to n-type conductivity of LTFO sensor for increasing H_2 exposure at 500 °C

This transition is strongly influenced by experimental conditions, as the analyte partial pressure, the operating temperature and even the structural composition of the material [260,261], as demonstrated by *Figure 33* and *Figure 34.* In the case of carbon monoxide, LTFO conductivity was only p-type while that of LFO showed also a slight inversion to n-type region: the presence of titanium ions moves the transition to higher pressure for each

temperature considered. The same behaviour occurred also in presence of hydrogen, but only for 400-500 °C, while at 600 °C the titanium doping shifted the minimum in the conductivity to lower hydrogen partial pressure enhancing the n-type semiconductivity. The influence of temperature is even noticeable, since the transition occurs at lower pressure with increasing temperature and showing progressively broader n-type region. Hence, the partial substitution of Fe^{3+} for Ti^{4+} was effectively advantageous: it allows to operate better in the range of concentrations and temperatures considered and adds chemical and thermal stability to $LaFeO_3$ perovskite, which indeed degraded to H_2 exposure at 600 °C unlike $LaTi_{0.4}Fe_{0.6}O_3$ (*Figure 34*). Finally, Ti^{4+} ions serve as donor centres occupying Fe^{3+} sites introducing excess oxygen and consequently reducing oxygen vacancies and holes concentration, resulting in a decrease of the material's conductivity in the p-type region [191,262,263]. The comparison of the sensors, in fact, confirms a lower baseline resistance of $LaFeO_3$, being 400-1300 Ω instead of 1-50 MΩ of $LaTi_{0.4}Fe_{0.6}O_3$.

As regards the sensors response to H_2S exposure, it was not possible to test LFO sensor, since the sensing material has degraded during the test with H_2, as previously demonstrated. In the case of LTFO (*Figure 36*), pure n-type behaviour of the material was registered at these concentrations of H_2S, revealing that the minimum in the conductivity trend is shifted to lower critical partial pressure of H_2S.

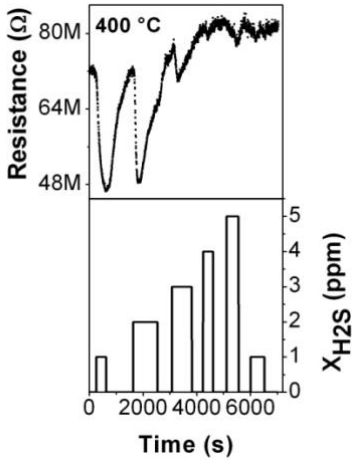

Figure 36. Resistance measurements on $LaTi_{0.4}Fe_{0.6}O_3$ sensors at 400 °C for successive H_2S exposure

In addition, sensing responses occurred, but unfortunately only for the first H_2S exposures: the sensing material has evidently degraded as the H_2S concentration level increased.

Indeed, the reversibility properties gradually disappeared and no resistance response was registered for concentration of 4 and 5 ppm: the degradation of the material was confirmed by the absent sensor response even during the repeated test with 1 ppm of H_2S. This was probably due to a chemical irreversible reaction occurring between $LaTi_{0.4}Fe_{0.6}O_3$ and H_2S, which leads to a substitution of oxygen ions with sulphur ions and consequently modifies material characteristics [264,265]. Characterization after test of the material was performed, in order to verify this consideration, in addition to that of $LaFeO_3$. Post-mortem analysis of the two samples is shown in *Figure 37*. LFO exposed to hydrogen atmosphere at 600 °C effectively degraded, since it was reduced and partially transformed in simple oxides like La_2O_3 and FeO and in metallic elements as Fe. The perovskite material reduction is ascribed to that of Fe^{3+} cations, which in fact is reducible to Fe^{2+} or metallic iron around a temperature of 600-700 °C, as stated form previous Temperature Programmed Reduction analyses on $LaFeO_3$ [266–268].

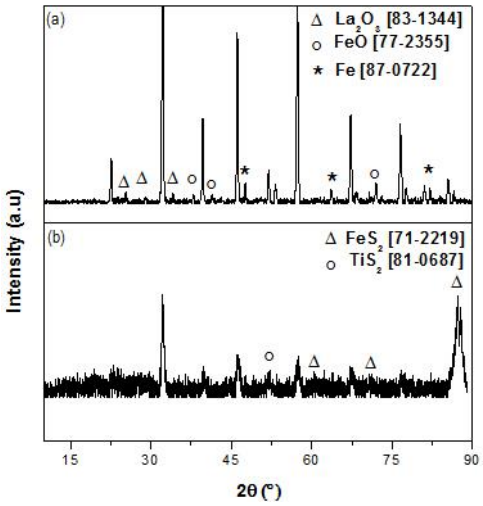

Figure 37. After tests XRD patterns of $LaFeO_3$ (a) and $LaTi_{0.4}Fe_{0.6}O_3$ (b)

The after tests XRD analysis on LTFO demonstrates that besides original perovskite structure even other sulphur compounds such as FeS_2 and TiS_2 are present, confirming that the degradation of LTFO after H_2S exposures actually results from the substitution of oxygen ions with sulphur ions. This was confirmed even by the Energy Dispersive Spectroscopy (EDS) analysis, which displayed an amount of around 2% of oxygen substituted with sulphur leading to a modified material of $La(Fe_{0.6}Ti_{0.4})(O_{2.94}S_{0.06})$.

The sensitivity of the materials to the different analytes was also analysed. The temperature and concentration dependence of the sensors sensitivity to CO presence are shown in *Figure 38*. It is evident that $LaTi_{0.4}Fe_{0.6}O_3$ material provides higher sensitivity in all cases. Its maximum sensitivity value, in fact, was 1.9, while that of $LaFeO_3$ was 0.9. In particular, it occurred at 460 °C for LTFO sensor, displaying a pure bell-shaped trend centred at this temperature for all the concentration levels considered. For lower or higher temperature, sensitivity gradually decreased, becoming almost zero at 600 °C: moreover, for temperature higher than 460°C, it is possible to note a decrease in the effect of the analyte concentration on the response, while at lower temperature this influence is noticeable. Indeed, *Figure 38.b* demonstrates that in general sensitivity is improved as concentration increases, but at 400 and 460 °C the gain is more evident, being the slopes of their trends visibly higher than that of 500 and 600 °C. Regarding LFO sensor, instead, its maximum sensitivity occurred at 400 °C, with a decreasing linear trend for all concentration considered, except for 150 ppm, where a new sensitivity peak appeared at the temperature of 600 °C, due to the transition of the material conductive properties. The effect of the analyte concentration on the response is mitigated around the temperature of 460 and 500 °C, as showed also by the concentration dependence chart, where the slopes of the relative trends are very low. Hence, the iron partial substitution with titanium ions is effectively profitable for CO sensing properties at these conditions of temperature and concentration, since higher sensitivity is obtainable and even at higher temperature. Moreover, it has been found that the maximum absolute values of sensing response *S* to 100 ppm of CO is about 0.8 at 80 °C and 0.7 at 325 °C for $La_{0.68}Pb_{0.32}FeO_3$ [269]: the B-site substitution with Ti ions has, thus, higher effect on sensitivity and even for higher operating temperatures compared by the A-site substitution. The works of Zhang et al. [269] confirms also the lower sensitivity of $LaFeO_3$ respect to the substituted materials.

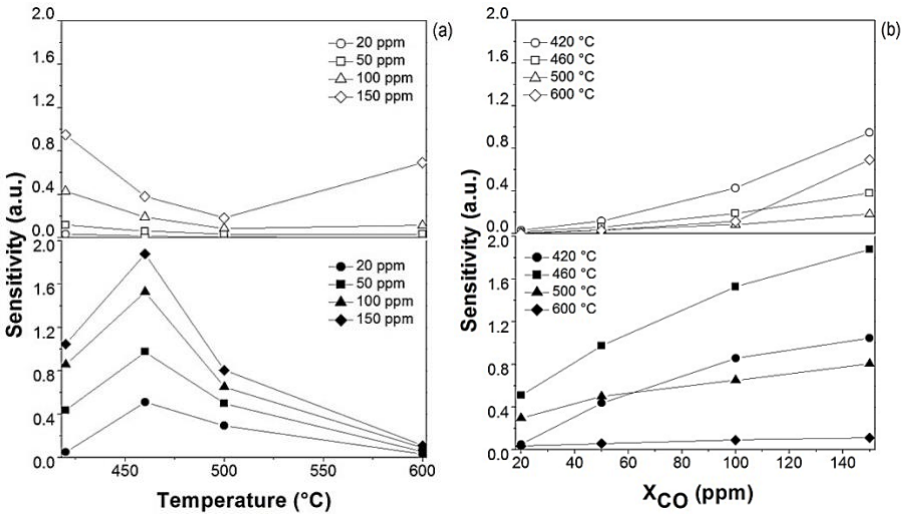

Figure 38. Temperature (a) and concentration (b) dependence of LFO (empty points) and LTFO (filled points) sensitivity to CO exposure

Sensors sensitivities to H_2 exposures (*Figure 39*) displayed different trends. In this case, indeed, was LFO to register higher sensitivity: 67.6 respect to the maximum value of LTFO of 1.4. LFO reached its maximum for the lower temperature and the higher concentration considered, noting that lower H_2 concentrations shift the sensitivity peak to higher temperature. Even LTFO showed the sensitivity maximum at the same concentration and temperature, even if for concentration higher than 3000 ppm the growth is almost negligible and the concentration dependence trends come closer to the asymptotic region (*Figure 39.b*). The same range of concentrations reported a minimum in the temperature dependence of the LTFO sensitivity for 500 °C and a successive increasing for higher temperature, due to the transition of the material conductive properties. Nevertheless, despite the higher sensitivity, LFO sensor showed serious difficulties in the operation at high temperature, since at 600 °C degraded to H_2 exposure. Hence, the presence of titanium ions is effectively advantageous for the improving of the thermal and chemical stability of the material.

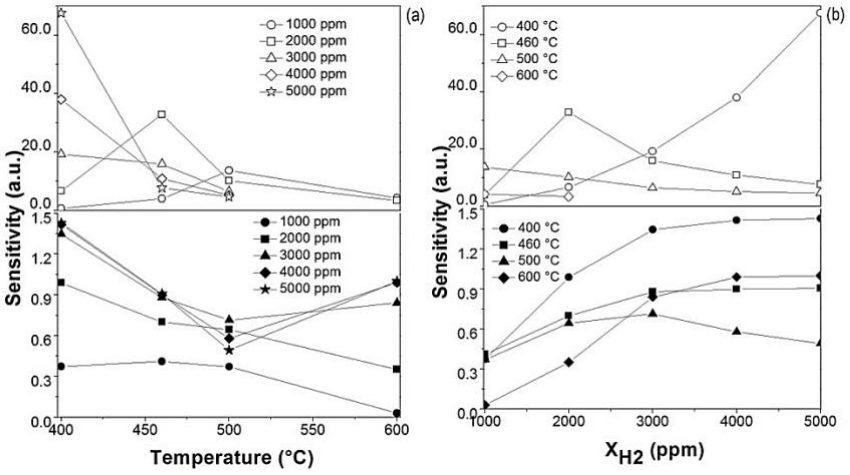

Figure 39. Temperature (a) and concentration (b) dependence of LFO (empty points) and LTFO (filled points) sensitivity to H_2 exposure

Summarizing, partial substitution of B-site perovskite with titanium ions is effectively profitable. Indeed, LTFO sensitivity to CO exposures is higher than that of LFO sensor and occurs at higher temperatures. The same results are obtained even with the comparison with A-site substitution. Moreover, the titanium presence increases the chemical and thermal stability of the $LaFeO_3$ based material in a reducing atmosphere. This is even more evident in the case of H_2 exposures, when degradation of the unsubstituted material occurs at 600 °C. Nevertheless, sensitivity of LTFO sensor to hydrogen was lower than that of LFO. In addition, the titanium substitution rises up the characteristic resistance of the material, which could be then of difficult evaluation. Finally, LTFO resulted unsuitable for H_2S measuring, since the material degraded after the chemical irreversible reaction.

Carbon monoxide tests

$LaFeO_3$ perovskite partially substituted with titanium ions is an attractive material for gas sensing purposes, as previously demonstrated. However, it shows good characteristics mostly in the carbon monoxide sensing, rather than hydrogen and hydrogen sulfide sensing. Hence, a deeper analysis on partial substitution with titanium focused on CO sensing was carried out. In particular, five different $LaTi_xFe_{1-x}O_3$ materials were synthesized via auto-combustion method, listed in *Table 23* together with the relative sample's name, in order to evaluate the optimum chemical material and titanium content for maximizing sensor response to carbon monoxide presence. Synthesis parameters were set as in the previous analysis on $LaTi_{0.4}Fe_{0.6}O_3$: CA/M=2.5, pH=7, Φ=0.45.

$LaTi_xFe_{1-x}O_3$	Sample
$LaFeO_3$	Ti00
$LaTi_{0.2}Fe_{0.8}O_3$	Ti20
$LaTi_{0.4}Fe_{0.6}O_3$	Ti40
$LaTi_{0.6}Fe_{0.4}O_3$	Ti60
$LaTi_{0.8}Fe_{0.6}O_3$	Ti80

Table 23. Synthesized $LaTi_xFe_{1-x}O_3$ material and samples name

Structural and morphological characteristics of synthesized materials were firstly evaluated by means of characterization analysis. *Figure 40* displays XRD spectra of the samples, compared with the reference one. It is evident how successfully syntheses were conducted, providing very fine powders of $LaTi_xFe_{1-x}O_3$ perovskite oxide and showing a good integration of titanium ions in the crystal structure.

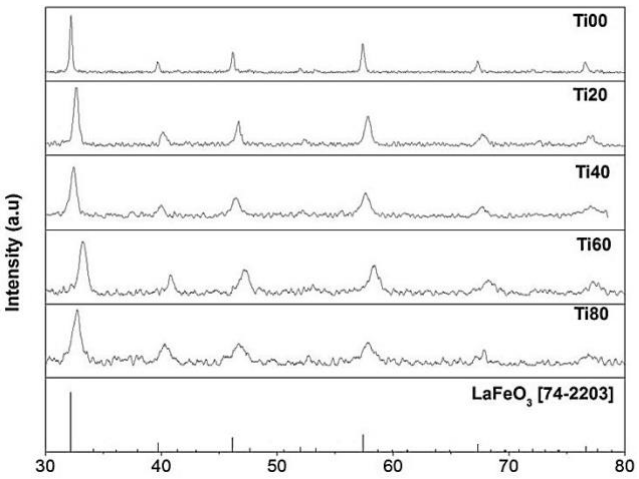

Figure 40. XRD spectra of the synthesized $LaTi_xFe_{1-x}O_3$ samples and the reference one

This is confirmed by the Goldshmidt tolerance factor *t*, calculated for a perovskite oxide with the general formula $AB'_xB_{1-x}O_3$ as [270]

$$t = \frac{r_A + r_O}{\sqrt{2}(x r_{B'} + (1-x) r_B + r_O)} \quad \textbf{(4.14)}$$

where the ionic radii of La^{3+}, Fe^{3+}, Ti^{4+} and $O^{2-}$are R_A=1.36Å, R_B=0.55Å, $R_{B'}$=0.61Å and R_O=1.4Å respectively [271]. Tolerance factors of the synthesized samples ranges between 1.00 and 0.97 (*Table 24*), revealing that titanium ions fit well the perovskite structure avoiding the distortion of the cubic system. However, it is possible to note that tolerance factors gradually decrease as the titanium amount increases, generating slight deformation

of the materials structure, and even XRD spectra start to show slight imperfections, which anyway do not compromise crystal structure and perovskite phase. Titanium content had influence even on the average crystallites dimensions, calculated by Scherrer equation as shown before (equation 4.11). In *Table 24*, it is possible to note that the crystallites size is decreasing as the titanium content is increased, affecting the sensing performances of the material, which require no grain sintering and high crystallinity [243].

Sample	***t***	***D_c (nm)***
Ti00	1.00	32
Ti20	0.99	17
Ti40	0.99	13
Ti60	0.98	11
Ti80	0.98	10

Table 24. Tolerance factor and average crystallites sizes of $LaTi_xFe_{1-x}O_3$ samples

The effectiveness of the synthesis method was confirmed even by SEM analysis, reported in *Figure 41*. Note that all the materials resulted to have high crystallinity with no generation of amorphous phases. The good morphological characteristics are confirmed even by the grain size evaluation, which revealed that average particles' dimensions range between 50 and 100 nm, showing effectively nanostructured perovskites. Since grains are made by several crystallites, former's sizes are larger than latter's dimensions obtained by XRD analysis. Finally, by means of the EDS analysis was possible to demonstrate that samples had a homogeneous chemical distribution and a proper chemical composition, also regarding the titanium content and dispersion.

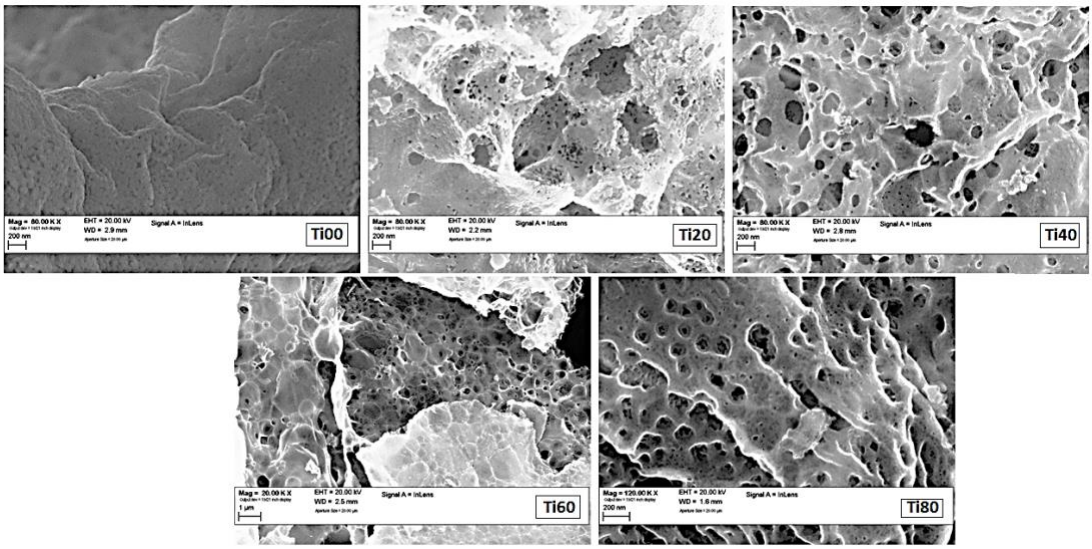

Figure 41. SEM analysis of $LaTi_xFe_{1-x}O_3$ synthesized samples

After the evaluation of the structural and morphological characteristics, sensing performances of different powders have been analysed. Tests were carried out for operating temperatures ranging between 400 and 600 °C and CO concentration of 20-150 ppm, by means of the experimental apparatus earlier illustrated. *Figure 42* shows the Arrhenius plot for samples conductivity. Of course, conductivity decreases with temperature, being the materials as semiconductors. Lower conductivities are caused even by titanium content intensification. As previously discussed, introduction of Ti^{4+} ions instead of Fe^{3+} ions in $LaFeO_3$ perovskite (p-type semiconductor), causes a reduction of oxygen vacancies and then holes concentration, which in turn reduces material's conductivity. This influences the functionality of the sensors, since for practical and operating reasons it is preferable to work with high conductivities (and so low resistances) because of technical limitations of instruments involved on the electrical properties measurements [272].

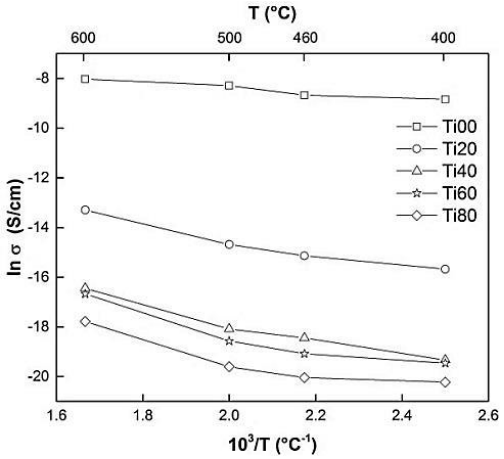

Figure 42. Arrhenius plot for conductivity σ of the various $LaTi_xFe_{1-x}O_3$ materials

In addition, samples showed different responses to carbon monoxide exposures. In *Figure 43*, different resistance responses are summarized, all relative to tests with 150 ppm of CO and temperature of 460 °C and 600 °C, being these the most representative of the entire test campaign. It is confirmed that a partial substitution with titanium ions is profitable, as previously affirmed. Ti00, indeed, showed an unclear response signal for both the temperatures, the same obtained in the previous analysis with LFO and LTFO sensors: as the material is exposed to CO the resistance starts to increase up to a maximum, being a p-

type semiconductor, but then quickly decreases and stabilizes around a constant value while the analyte flow is still present. The same behaviour was registered even for Ti20 sample. On the contrary, with titanium content higher than x=0.4 the resistance development is more clear and stable, with the sharp resistance rising in carbon monoxide atmosphere and its recovery when the analyte is removed. However, this trend was registered at 460 °C for all remaining samples, while at 600 °C Ti60 seemed to be indifferent to CO presence and Ti80 showed the opposite progress, with a sharp decreasing of the resistance typical of an n-type behaviour.

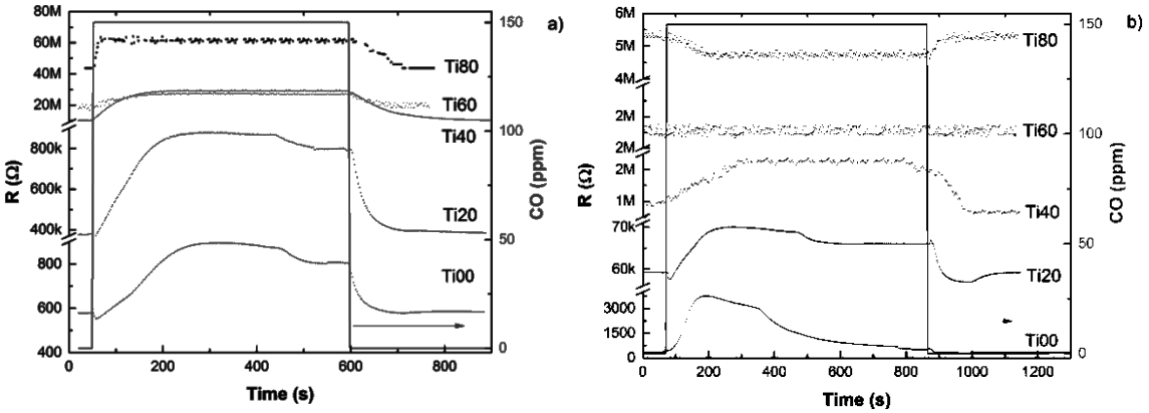

Figure 43. Sensors response to 150 ppm of CO at 460 °C (a) and 600 °C (b)

This phenomenon is ascribed to the dual conductive behaviour of $LaFeO_3$, showing a transition from p-type to n-type properties depending on analyte partial pressure, operating temperature and chemical composition of the material. Since this, it was possible to note n-type behaviour only at the temperature of 600 °C, for carbon monoxide concentration higher than 150 ppm and for titanium content of 0.8. In addition, Ti60 was tested also at the higher temperature of 680 °C, when reported n-type behaviour with 100 and 150 ppm of CO, confirming the influence of operating temperature, concentration and composition on materials conductive characteristics. The transition of the conductive properties is responsible even of the ambiguous trend of Ti00 and Ti20 showing first a growth and later a reduction of the resistance. In those cases, the operation around the minimum in the conductivity trend and a low diffusion coefficient caused a lower gas diffusion rate into the material and then higher response time, hiding sharp resistance decreasing. The change of conductivity is not a limiting factor for sensors operation, but could generate difficulties in the interpretation of the signal and can complicate its functionality. In addition, Ti60 and

Ti80 signals resulted to be more discontinue and noisy, probably even because of the gradually deformation of the perovskite crystal structure by titanium content increasing.

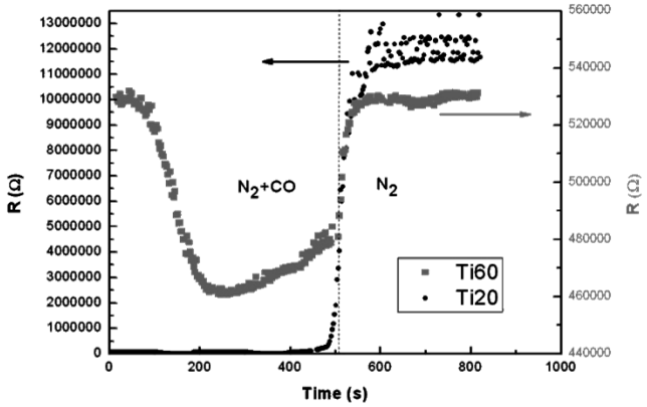

Figure 44. Response to 150 ppm of CO at 680 °C of Ti20 and Ti60 sample

Moreover, regarding the reversibility properties all the materials had no drift on resistance baseline in any case and they were not degraded by carbon monoxide, except for Ti20 which effectively was reduced at 680 °C and 150 ppm CO. In *Figure 44* it is possible to note that the material's resistance fast rose up to 12 MΩ (baseline resistance was 52 kΩ, so three order of magnitude more) and remained stable at this value even without CO presence. It has to be stressed here that, at the same temperature and analyte concentration, sample Ti60 was not reduced and degraded: increasing of titanium content in $LaFeO_3$ composition is effectively profitable for thermal and chemical stability. However, considering also resistance signals and crystal cell deformations, a compromise should be found and sample Ti40 seems to be the best solution, in order to have clear response and good thermal stability.

Sensors sensitivity (*S*, calculated with equation 4.12) to carbon monoxide at different temperatures was also evaluated (*Figure 45*). Maximum sensitivity was 2.1 at 400 °C, proper of Ti20 sample. The same material, however, drops in sensitivity as the temperature is increased. Ti40, instead, shows the maximum sensitivity at 460 °C, assuming a value not far from the previous one of about 1.8. Other samples have not same proper sensing properties, since the sensitivity is always below 1, even if with some variations. However, all the materials demonstrate very low sensitivity as the temperature increases: the best operating range is 400-460 °C. Note that for Ti80, sensitivity assumes negative value since the occurred transition of the conductive properties. Regarding concentration dependence,

in general sensitivity is improved as concentration rise up, but in the case of Ti20 and Ti40 the gain is more evident and plateau region is not yet reached. Hence, sensors can measure even higher concentration, being far from saturation. Therefore, Ti20 and Ti40 are the most suitable materials, but considering that Ti20 reported unclear signals and have a lower thermal stability, once again Ti40 results to be the best sample.

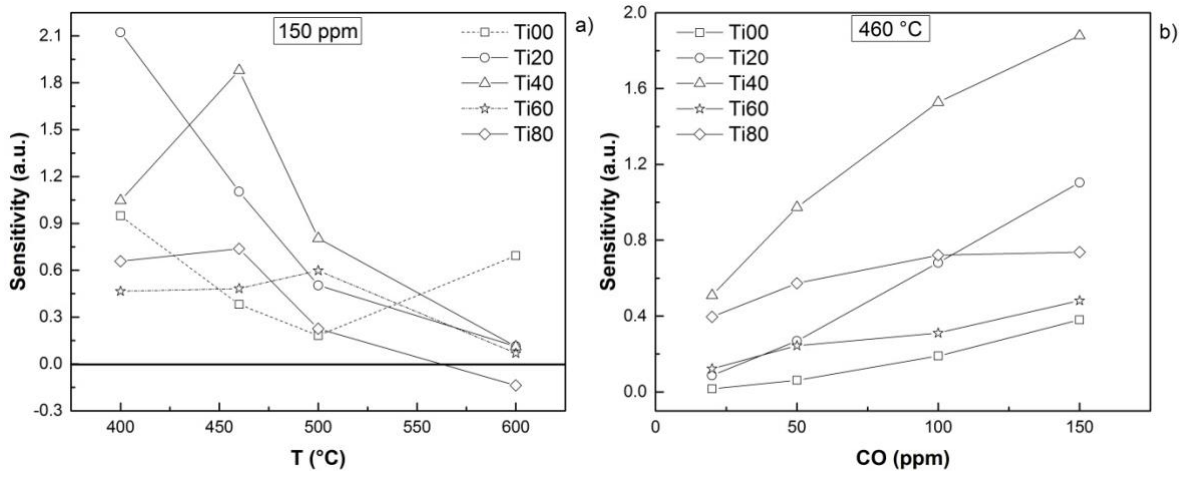

Figure 45. Temperature (a) and concentration (b) dependence of sensors sensitivity to CO exposure

Response and recovery time were also analysed. In *Figure 46* are reported those relative to Ti40 samples, being the most representative ones (20 ppm at 400 °C have not been taken into account since the response was almost zero). Both response and recovery times decrease as the temperature increase, even if the drop is less evident for higher temperature (500-600 °C) when values seem to stabilizing. Interactions between sensing material and analyte based on adsorption-desorption phenomena, indeed, are dependent from temperature, influencing reaction times [273], but response time is also influenced by sensitivity and, in fact, higher response times occurred in cases with higher sensitivity. Gas-solid interactions are influenced even by the amount of analyte involved, since with higher concentrations gas molecules could be easier detect but could complicate the release of the same ones [274,275]. In fact, response and recovery times were shorter for higher concentrations, but the reduction is more evident in the case of the former. Finally, recovery times resulted larger than the response ones in all cases, being in the range of 10-2 minutes, instead of 5-1 minutes. In general, a sensor is considered to have fast responses with times of 1-3 minutes [276,277]. Hence, further studies need to be developed in order

to reduce these ranges of values, for example by improving material's surface area, porosity and thickness [278–281].

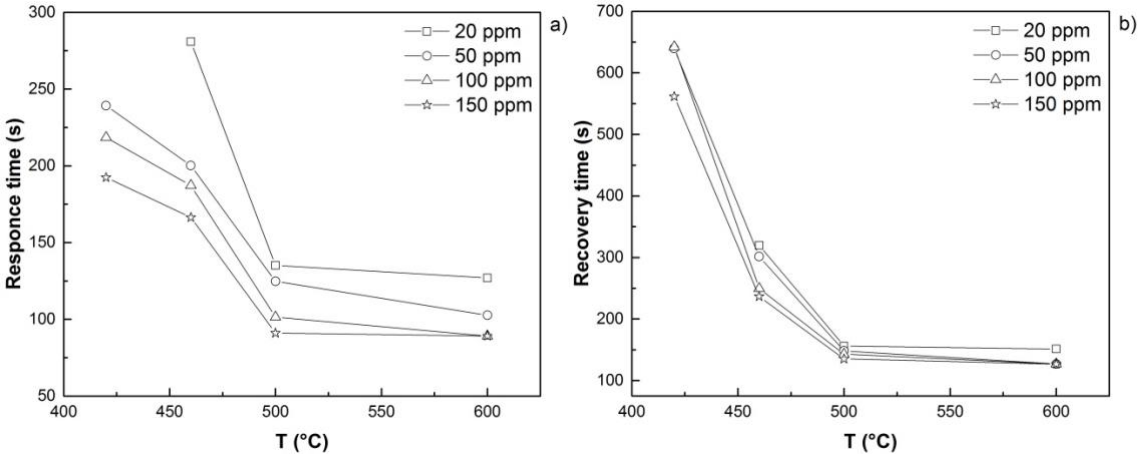

Figure 46. Temperature dependence of Ti40 response time (a) and recovery time (b)

Summarizing, $LaTi_xFe_{1-x}O_3$ perovskites are very advantageous materials for carbon monoxide sensing purposes at relatively high temperatures. The maximum sensibility is reached with 20% of partial substitution in Fe ions, but increasing it to 40% high sensitivity is anyway obtainable at higher temperatures (460 °C). Moreover, the former case leads to unclear response signal, complicating sensor operation. With higher titanium content, thermal and chemical stability of the material is enhanced, but quality of response and sensitivity are gradually lowered. Therefore, the best $LaTi_xFe_{1-x}O_3$ seemed to be $LaTi_{0.2}Fe_{0.8}O_3$ and $LaTi_{0.4}Fe_{0.6}O_3$.

Hydrogen tests

$LaTi_xFe_{1-x}O_3$ perovskites are suitable material for CO sensing and control. Unfortunately, however, they didn't show the same good results for hydrogen and hydrogen sulphide atmosphere. Further researches were then necessary, in order to find out a proper material for these purposes. The attention was anyway focused on partial substitution on B-site of the perovskite material with specific chemical elements, being B-site the most affecting factor on the material sensitivity, as previously stated in chapter 2. In particular, it was decided to investigate the catalytic action of cobalt ions (Co^{2+}) on H_2 sensing purposes, which are supposed to create more active sites for reducing gas interaction and thus to enhance sensitivity to hydrogen [159,160]. The interest was also to evaluate the influence of

divalent ions presence instead of tetravalent ions (Ti^{4+}) and to compare the material behaviour after substitution with p-type or n-type dopant.

Four different perovskite materials were thus synthesized, by means of auto-combustion synthesis technique (citrate-nitrate method) addressing the previously exposed procedure and even the previous considered parameters and parameters values. In particular, it was decided to synthesize the simple lanthanum-ferrite perovskite, the one partially substituted with two different cobalt amounts and that with a mixed partial substitution with cobalt and titanium in the same time (see *Table 25*). In this way it was possible to determine the effect of cobalt ions, the effect of the amount of cobalt and the mutual effect of cobalt and titanium.

$LaM_xFe_{1-x}O_3$	Sample
$LaFeO_3$	LFO
$LaCo_{0.2}Fe_{0.8}O_3$	Co20
$LaCo_{0.4}Fe_{0.6}O_3$	Co40
$LaCo_{0.2}Ti_{0.2}Fe_{0.6}O_3$	Co20Ti20

Table 25. Synthesized $LaM_xFe_{1-x}O_3$ material and samples name (M=Ti and Co)

The obtained powders were subjected to characterization analysis. All the samples resulted to be very fine powders of desired perovskite oxides, showing also a good integration of dopant ions in the crystal structure. Also the Goldshmidt tolerance factor confirms high structural and morphological characteristics: it ranges, in fact, between 1 and 0.95.

Gas sensing performances of the synthesized samples were then evaluated. Tests were carried out in the laboratories of European Commission-Joint Research Centre, specifically in the Institute of Transport and Energy of Petten (The Netherlands). Experimental apparatus used was completely similar to that showed in the paragraph "*Materials preparation*". Operating temperatures considered were between 200 and 600 °C, while hydrogen concentration has range of 0.1-0.4%$_{vol}$. Samples showed different behaviour at different concentration and temperatures: *Figure 47* summarizes different results, displaying only tests with 0.4% of hydrogen and temperature of 200 °C and 400 °C, being these the most emblematic of the test campaign. It should be stressed here that the highly noisy nature of response signal is surely due to the bad temperature control of the furnace. Its regulation by

LabVIEW® software, in fact, was not completely stable at the desired temperature, implicating a sort of fluctuation around it: signal fluctuations are then extremely correlated and caused by temperature fluctuations, as it is possible to note in *Figure 47.a*; of course, resistance decreases as the temperature increases and vice versa, being samples semiconductors materials. In addition, temperature stability was increased as the operating temperature was rose up, when even response showed lower or absent signal noise, confirming the hypothesis of the strict correlation between it and the temperature control. At 200 °C, Co20 and Co40 are the only samples showing responses to the hydrogen presence, even if not so evident, increasing their resistance as H_2 increases (p-type behaviour). Moreover, fluctuations in the signal responses correlated with temperature variations resulted to be lowered in the case of Co40, demonstrating that the amount of cobalt has a sort of influence on the materials temperature dependence. On the contrary, resistance of Co20Ti20 has no changes in analyte atmosphere, while regarding LFO it was not possible to have information in this sense since its high intrinsic resistance. The situation is overturned at 400 °C, when it is evident that samples with only cobalt degraded, having a sharp increase of resistance value that remain constant even when hydrogen is removed. LFO and Co20Ti20, instead, were still able to measure hydrogen concentrations but reported the ambiguous behaviour of a first sharp growth and then a decrease of the resistance until a constant value: the transition of the conductive properties from p-type to n-type behaviour occurred, and in particular LFO showed the transition even at 350 °C. In addition, analysing LFO and Co20Ti20 trends it is possible to note also that the presence of the two dopant in the perovskite structure is advantageous also as regards response and recovery time: LFO was not able to restore the initial resistance even after one hour in nitrogen, differently from Co20Ti20; also the response time was slightly higher.

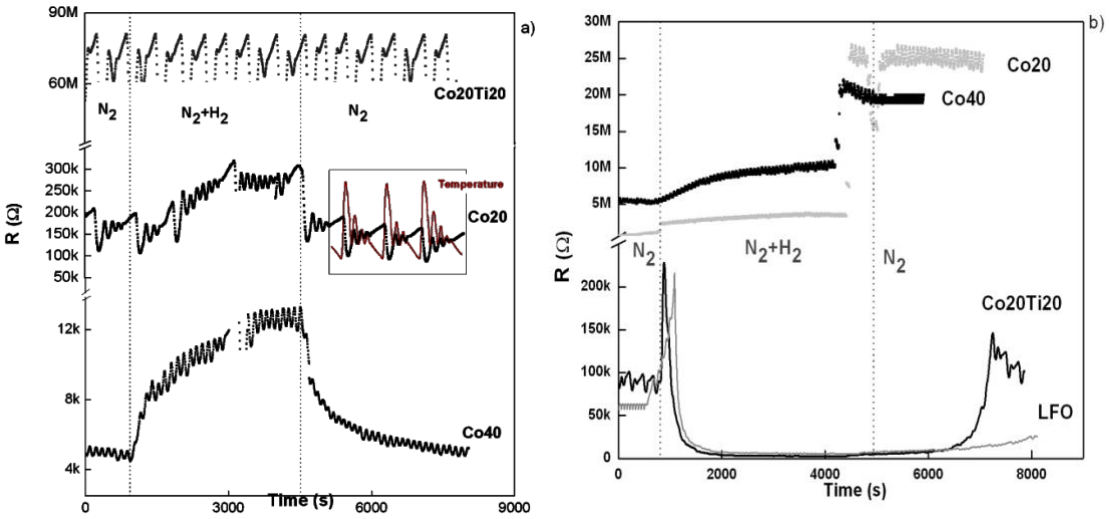

Figure 47. Sensors response to 0.4% of H_2 at 200 °C (a) and 400 °C (b)

Therefore, the substitution with cobalt ions is effectively advantageous since it provides a clearer and more stable signal, avoiding the conductive properties transition occurring. Nevertheless, it shifts the operating range of the samples towards lower temperatures. In the same time, Co20Ti20 showed the largest working range, degrading at 500 °C and confirming the hypothesis of better thermal stability and behaviour for titanium partially substituted perovskites, improving their operation at higher temperatures but impoverishing at the same time response signal at lower temperatures. It has to be stressed, moreover, that the degradation occurred at 500 °C was probably due to circuit damaging because some test problems that affected the experimental procedure, more than materials degradation. Interdigitated electrodes of Co20Ti20 and LFO after tests, in fact, demonstrated damages to gold circuits (see *Figure 48*), leading to interruption of the same circuits and impossibility to measure materials electrical properties.

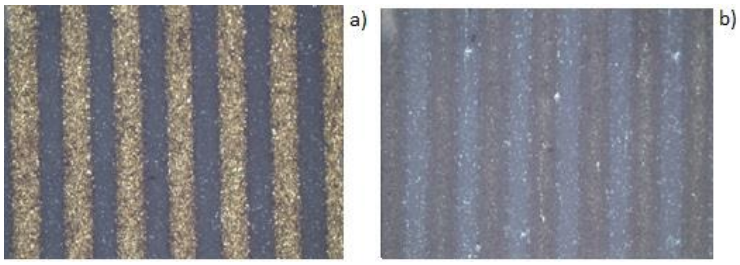

Figure 48. Microscopic pictures of Au circuit, before (a) and after (b) tests at high temperatures

Moreover, each gas sensing test has been repeated on a second sample (S2) of each material, being different from the first sample (S1) in the thickness: S2 had a thickness of 0.2 mm, while S1 was around 0.1 mm. Response signals from two samples of all materials tested were quite similar, reproducing the same trend and behaviour for the same sequence of tests, demonstrating thus good reproducible properties. However, signals from S2 showed a higher variability respect to S1 (*Figure 49*) in terms of noise of response: this means that the thickness of film layers influences the responses signal of the material, making it highly dependent to temperature and to flow conditions, which could generate some turbulences in gas stream and directly inside the film. Hence, also thickness is a crucial parameter for good operation of chemical gas sensors and it is possible to assume that signal stability is enhanced for higher cobalt contents and lower thickness of the materials. In any case, all the materials showed an almost absent drift of the baseline resistance, proving their good recovery properties.

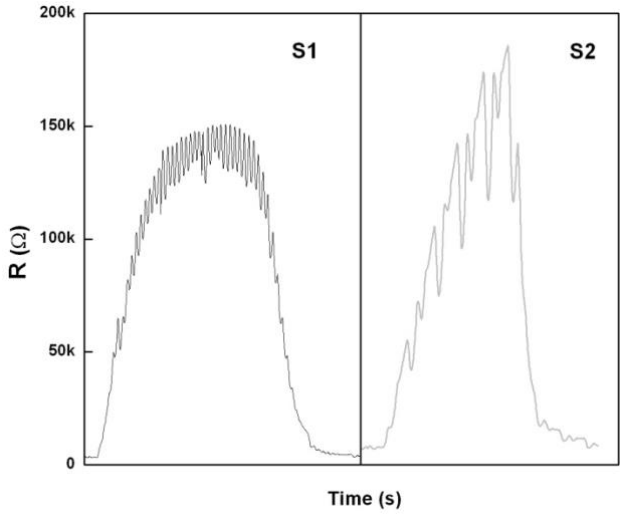

Figure 49. Signal response to 0.4% of H_2 at 300 °C of S1 for different samples thickness

Analysing the Arrhenius plot (*Figure 50*) for samples conductivity, moreover, it is evident that, being all studied materials semiconductors, their baseline resistance R_0 (that is the resistance characteristic of the material in nitrogen flow and for each temperature) decreased as temperature increased. Comparing baseline resistance of different materials, it is possible to note that increasing content of cobalt ions it gradually decreases. Substituting Co^{2+} for trivalent ion site in $LaFeO_3$, in fact, a consequent charge compensation occurs, by means of oxidation of Fe^{3+} ions to Fe^{4+} ions or by the formation of lattice oxygen

vacancies: therefore, the concentration of holes h^+ increases and, in turn, the conductivity of the material, while the resistance decreases [262,263]. In the case of partial substitution with Ti^{4+} ions, instead, the situation is completely the opposite, as demonstrated also by previous researches: the conductivity of Co20Ti20 sample, indeed, is reduced. In particular, in this case the combined effect of cobalt and titanium ions leads to different values of the conductivity for different temperature: over 300 °C, conductivity is less than that of LFO, since effect of Ti^{4+} is prevalent (in fact it increases thermal properties), while below 300 °C it is higher. It was not possible to evaluate conductivity of LFO for those temperatures because of technical measurements limits of the multimeter, but this confirms anyway that its σ is lower than Co20Ti20. Co^{2+} substitution, then, is profitable also for the functionality of the sensor, providing higher conductivity, for sure easier to be managed because of technical limitations of instruments involved on the electrical properties measurements.

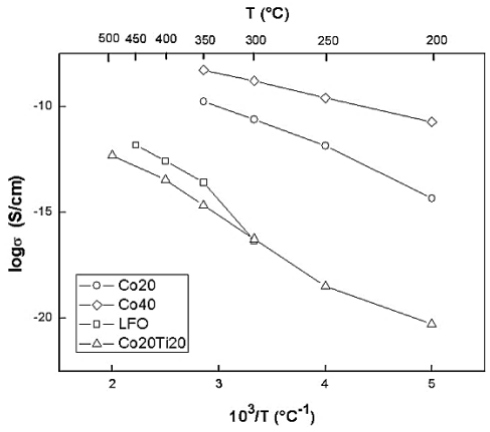

Figure 50. Arrhenius plot for conductivity σ of the various $LaM_xFe_{1-x}O_3$ materials

Finally, sensitivity analysis was performed (*Figure 51*). Regarding temperature dependence, it was possible to note that cobalt partial substitution is effectively advantageous for lanthanum ferrite perovskites, since it highly increases the sensitivity to hydrogen presence at higher temperatures: at 350 °C, sensitivity of Co40 was around 100, instead of 16 for LFO (sensitivity of LFO decreases as the temperature and hydrogen concentration increases because of the transition of conductive properties occurred). At 300 °C the conditions are favourable for the latter, but at those order of temperature material resistance is very high and its measuring could be problematic, as happened in this experimental campaign. Focusing on cobalt content, sample Co40 resulted to be the

preferable one, since it shows very higher sensitivity at higher operating temperature: Co20 demonstrated a pure bell-shaped trend with maximum on 300 °C, anyway lower than Co40 maximum. As regards mixed partial substitution with titanium ions, the sensitivity was very low for all the temperatures considered, having anyway a maximum on 350 °C: presence of titanium, hence, was effectively profitable for material thermal stability, as stated previously, but not for sensitivity. Also for concentration dependence, Co40 seems to be the preferable material, since it shows the maximum sensitivity and a perfect increasing trend, not an almost constant curve as the other materials, which are already in the saturation region and thus do not allow a clear hydrogen measuring. Even in this case, LFO has a decreasing trend since the transition of conductive properties. Comparing this hydrogen sensitivity results with those obtained with $LaTi_{0.4}Fe_{0.6}O_3$, it is possible to assume that partial substitution with Co^{2+} ions is in effect advantageous for hydrogen sensing purposes, since it allows to obtain very higher sensitivity both respect to the basic lanthanum ferrite perovskite and to the titanium substituted one. Nevertheless, it shifts the operating range of the sensor towards lower temperatures, implicating a maximum operating temperature of 350 °C.

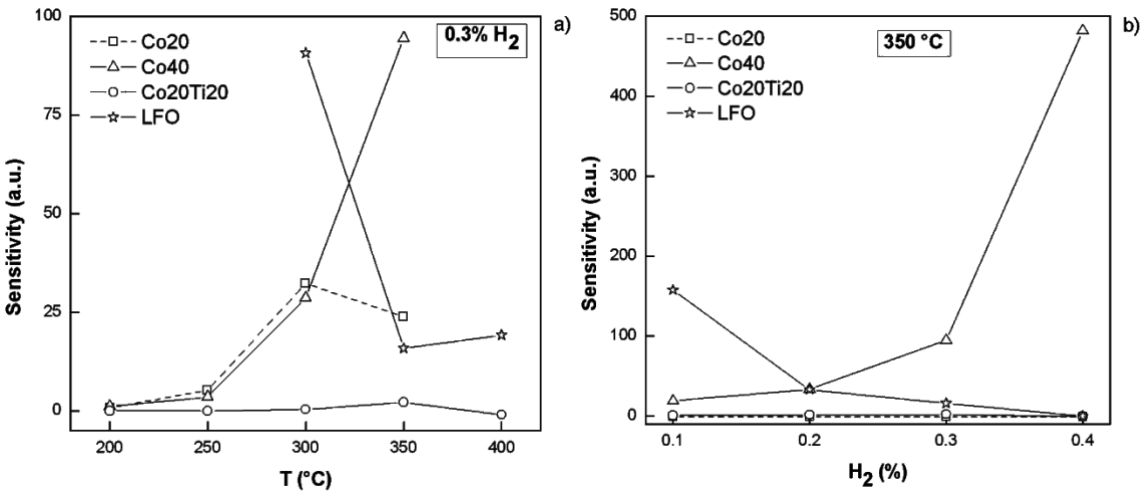

Figure 51. Temperature (a) and concentration (b) dependence of samples sensitivity

Operating parameters influence

From previous analysis it is evident how sensors sensitivity and response are influenced by operating conditions, such as temperature and gas concentration. A deeper study was then conducted on the evaluation of sensors performances dependence on tests

parameters. The support of chemometrics was fundamental either in the experimental campaign planning, with the Design of Experiment (DoE), either in the results evaluation, with the multivariate analysis.

This study was carried out on $LaTi_{0.2}Fe_{0.8}O_3$ perovskite regarding the carbon monoxide sensing performances, since one of the most promising material for this purpose. It was chosen a full factorial experimental design with three factors and three levels, addressing the Central Composite Design. The relative DoE consists of 27 experiments, arranged geometrically as a body, side and edge-centred square, as shown in *Figure 52.*

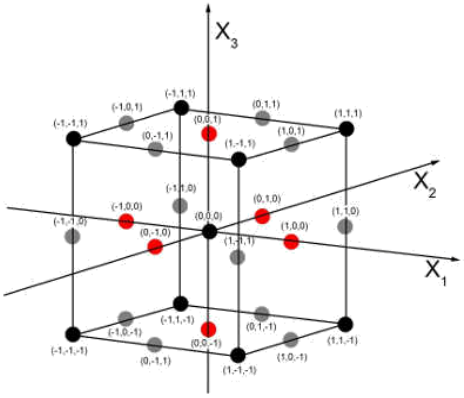

Figure 52. Geometrical representation of DoE for operating parameters influence evaluation

The independent parameters considered were CO concentration (X_{CO}), operating temperature (T) and gas flow (Q), varied respectively in the ranges of 100-200ppm, 300-460 °C and 40-100 Nml/min, being the most representative as affirmed by previous analyses. Multivariate data analysis was based on a non-linear multiple regression, having polynomial function as

$$Y = b_0 + b_1X_1 + b_2X_2 + b_3X_3 + b_{12}X_1X_2 + b_{13}X_1X_3 + b_{23}X_2X_3 + b_{11}{X_1}^2 + b_{22}{X_2}^2 + b_{33}{X_3}^2 \quad \textbf{(4.15)}$$

Y is the response and X_1, X_2, X_3, normalized from –1 to +1, are X_{CO}, T and Q respectively. *b* coefficients represent the influence of independent parameters on responses: in particular, b_0 is a constant, b_i represent the main direct effects of variable X_i, b_{ii} show the non-linear relationship between the responses and the experimental variables and, finally, the indirect effects produced by cross-interaction between X_i and X_j are represented by b_{ij} coefficient.

Responses studied were the sensitivity of the sensor (*S*, calculated with equation 4.12) and the speed of response (*v*, expressed as kΩ/s), which is strictly correlated to the response time. *Table 26* summarizes the different test conditions for the different experiments, including also values of responses considered.

	Model matrix			*Experimental Matrix*			*Responses*	
	X_1	X_2	X_3	X_{CO} (ppm)	T (°C)	Q (Nml/min)	S	v (kΩ/s)
exp 1	-1	-1	-1	100	300	40	0.16	38.02
exp 2	1	-1	-1	200	300	40	0.14	60.09
exp 3	-1	1	-1	100	460	40	0.20	1.84
exp 4	1	1	-1	200	460	40	0.63	4.09
exp 5	-1	-1	1	100	300	100	0.22	67.22
exp 6	1	-1	1	200	300	100	0.24	98.35
exp 7	-1	1	1	100	460	100	0.20	2.87
exp 8	1	1	1	200	460	100	0.66	6.39
exp 9	-1	-1	0	100	300	70	0.19	59.48
exp 10	1	-1	0	200	300	70	0.19	66.61
exp 11	-1	1	0	100	460	70	0.33	4.38
exp 12	1	1	0	200	460	70	1.03	9.75
exp 13	-1	0	-1	100	380	40	1.03	52.11
exp 14	1	0	-1	200	380	40	2.22	94.85
exp 15	-1	0	1	100	380	100	2.05	115.07
exp 16	1	0	1	200	380	100	2.78	153.89
exp 17	0	-1	-1	150	300	40	0.15	54.58
exp 18	0	1	-1	150	460	40	0.32	1.97
exp 19	0	-1	1	150	300	100	0.21	83.70
exp 20	0	1	1	150	460	100	0.38	4.25
exp 21	-1	0	0	100	380	70	1.29	46.05
exp 22	1	0	0	200	380	70	2.60	111.98
exp 23	0	-1	0	150	300	70	0.20	63.89
exp 24	0	1	0	150	460	70	0.68	8.12
exp 25	0	0	-1	150	380	40	1.26	36.50
exp 26	0	0	1	150	380	100	2.31	116.17
exp 27	0	0	0	150	380	70	2.22	127.92

Table 26. Chemometric analysis for operating parameters influence evaluation

Some differences occurred during the different experiments. Sensor responses to carbon monoxide presence, in fact, were generally displayed as p-type behaviour: typical output signal from the sensor is shown in *Figure 53*.Test at 460 °C and 100 Nml/min of total flow, however, showed the ambiguous behaviour of a slight decrease of resistance while CO is still present. It is already possible to note how measuring and test conditions influence sensor operation and interpretation. From the obtained output signals were then evaluated the different values of sensitivity and speed in the response, listed in *Table 26*.

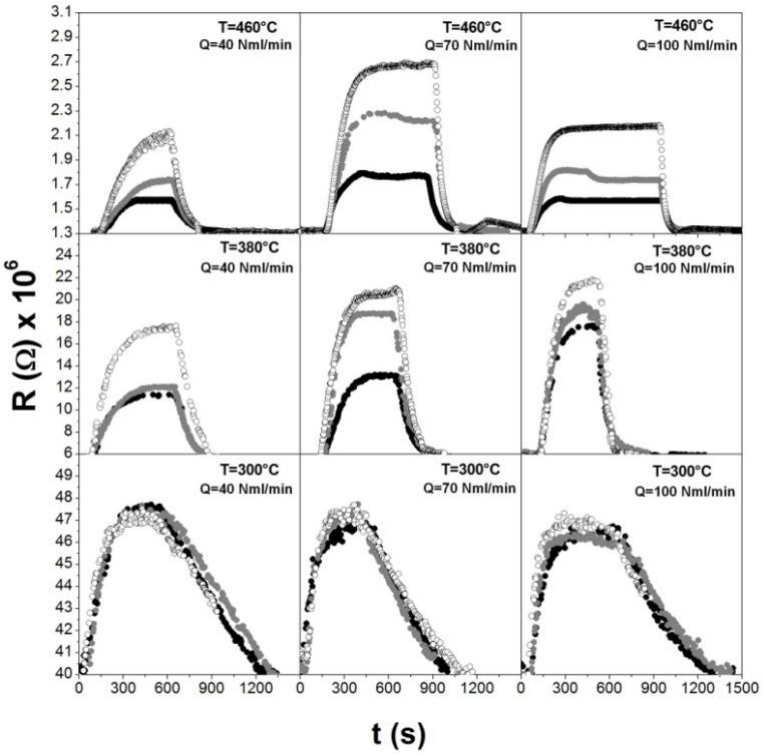

Figure 53. Response signal of $LaTi_{0.2}Fe_{0.8}O_3$ for different test condition (● 100 ppm CO; ● 150 ppm CO; ○ 200 ppm of CO)

Multivariate analysis on sensor sensitivity is shown in *Figure 54*, carried out considering all factors, all cross-terms and all square terms according to equation 4.15. In the bar chart of the coefficient of the mathematical model (*Figure 54.a*), also the relative statistical significances are displayed by means of the *p* parameter: only coefficient with $p<0.001$ were considered statistically significant and in the chart are marked with three stars (***). In addition, significance could be evaluated also with an analysis of the boundaries of the

confidence interval respect to the height of the bars factors: factors with bars within the boundaries of the confidence interval have no significance, while factors with bars bigger than the confidence interval are statistically significant. As it possible to observe in the figure, this evaluation confirms the analysis conducted on the *p* parameter. Therefore, it is possible to assume that coefficients statistically crucial are b_1, b_2, b_3, b_{12} and b_{22}: all three test parameters considered, thus, affect sensitivity of the material. In particular, carbon monoxide concentration, related to b_1, plays a key role, affecting the sensitivity only with a linear correlation, namely with a direct effect: indeed, increasing analyte concentration sensitivity is supposed to increase until saturation of the material is reached, when the sensitivity trend approaches the asymptotic value and stabilizes around a constant value. In the case analysed, it was not possible to observe the asymptotic region, since saturation was not reached with the concentration values considered. The same considerations are valid also for the gas flow influence, related to b_2, which showed only a linear and direct correlation with the sensitivity. Different is, instead, the case of the operating temperature, whose relative significant coefficients are b_2 and b_{22}, where the latter is quite prevalent on the former. Hence, the quadratic correlation is predominant and, in fact, perovskite materials have maximum sensing properties at a specific operating temperature, gradually lowered as long as temperature is reduced or enhanced. The variation of sensitivity with the temperature, in addition, is even mutual dependent on the concentration values, as demonstrated by the statistical significance of b_{12} cross-term, which in fact expresses that temperature and analyte concentration are correlated each other. All of these considerations are confirmed by the response surface plots (*Figure 54.b,c,d*). Sensitivity trend depending on X_{CO} and Q are effectively linear, while that of temperature T is quadratic and bell-shaped.

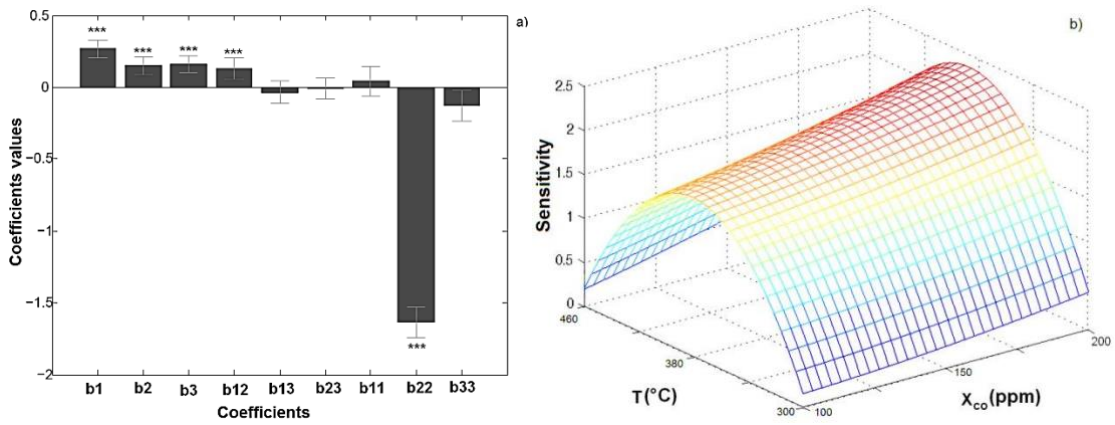

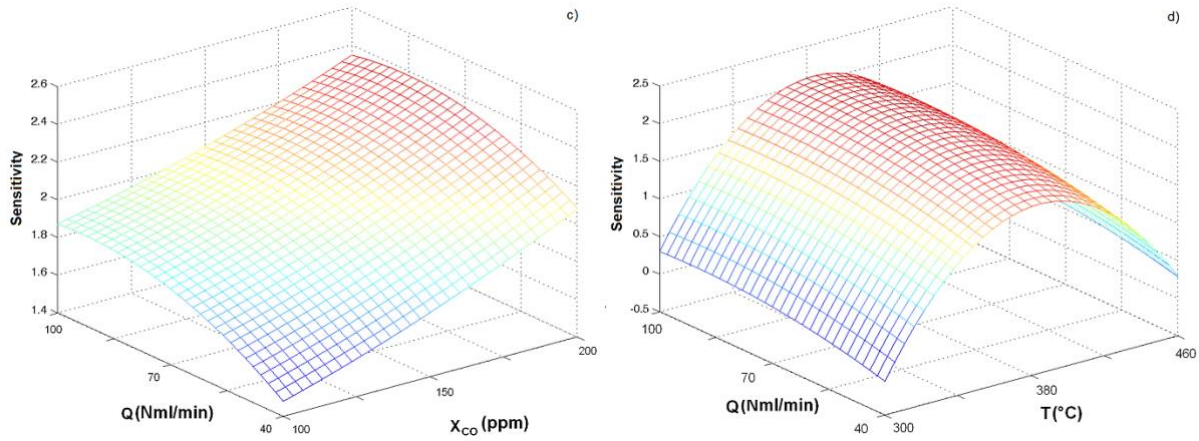

Figure 54. Coefficients (a) and Response surface (b, c, d) for the effect of test conditions on sensitivity ("no star" indicates no statistically significance, "three stars" p < 0.001)

Regarding the multivariate analysis on the speed of response of the sensor (*Figure 55*), the statistically significance limit of the b_i coefficients was set to p<0.05. The significant coefficients were, thus, b_1, b_2, b_3 and b_{22}. Therefore, as in the previous case of the sensitivity, all the three parameters considered affect the speed of response of the sensor and mainly by a direct effect. Analyte's concentration and gas flow have a linear correlation with the response, while for the temperature the quadratic correlation is prevalent. However, in this case, cross-interactions seem to be irrelevant.

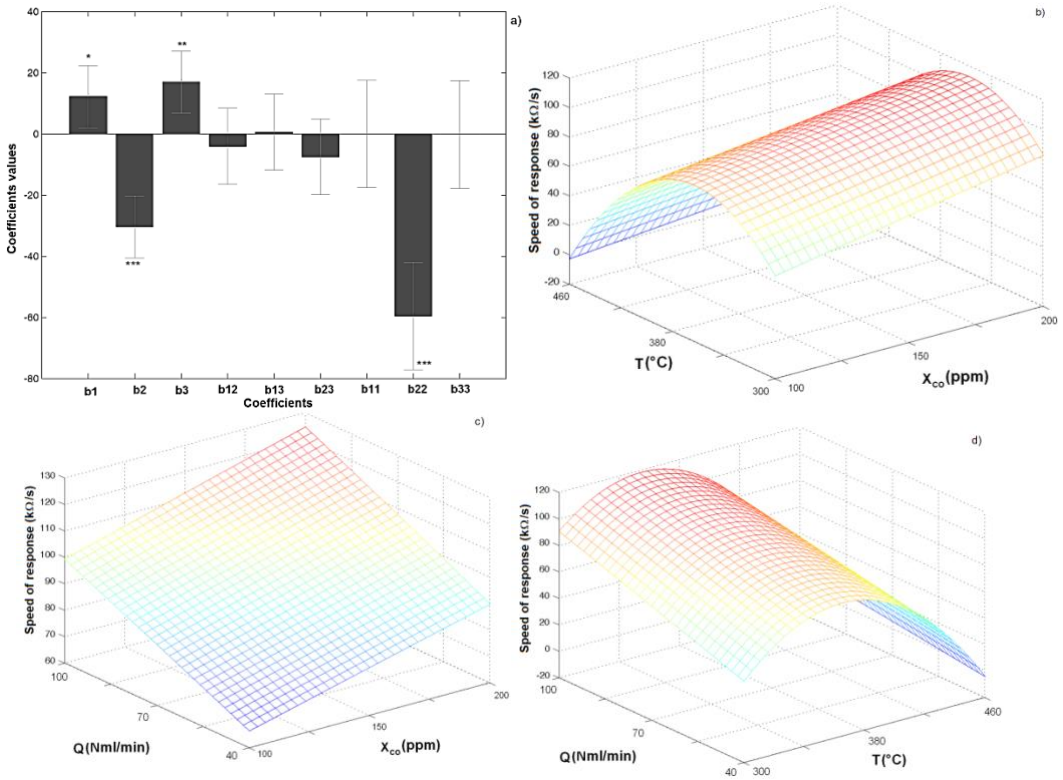

Figure 55. Coefficients (a) and Response surface (b, c, d) for the effect of test conditions on speed of response ("no star" indicates no statistically significance, "one star" $p < 0.05$, "two stars" $p < 0.01$, "three stars" $p < 0.0001$)

The analysis of the response surface plots (*Figure 55.b,c,d*) confirms these considerations: relationship between T and *v* are quadratic and bell-shaped, centred on 380 °C, while concentration and flow dependence trends increase linearly. As for the sensitivity, indeed, the speed of response is optimized around the specific temperature which provides the best chemical and physical conditions for sensing properties of the material. Moreover, even for the speed of response there is an increase when concentration and flow are enhanced. Higher content of analyte could be easier detect from the material, reporting consequently higher values of *v* [274,275]. Gas flow has even a higher influence, since it represents the amount of gas that reacts with the material and thus of the speed in the reaction between the perovskite and the analyte. It has to be noted here that as the speed of response increases, the response time decreases, even is not possible to perfectly correlate them since response time is strictly dependent on sensitivity also.

5. Conclusions and perspective

At the present, research activities on biomass waste thermochemical conversion processes and optimization of their energy and environmental efficiency are object of several research studies, in order to find out reliable and efficient systems to exploit the energy content of biomass, which is considered one of the most promising renewable energy sources.

The aim of this work was to develop new innovative chemoresistive gas sensors for control and optimization of biomass steam gasification power plants at different scale and configuration. Studies on gasification system and relative different configurations were then conducted. In particular, an innovative dual bubbling fluidized bed gasifier (DBFB) and its integration in a real plant were studied. Different biomasses were gasified with steam/air in a bench-scale bubbling fluidized bed gasifier, evaluating different producer gas compositions and tar content. The energetic contents of the output gases obtained was pretty similar and in any case quite relevant, thanks to the use of steam as gasifying agent. Also the tar contents in the producer gases were quite constant, having used olivine sand as catalytic bed material, but high. Similar results were obtained even in the pilot 100 kW_{th} dual fluidized bed gasifier, pointing out also the advantage of two chambers configuration that leads to higher quality syngas since its less dilution in nitrogen. It was stressed, thus, the importance of a gas cleaning and conditioning section for the removal of tar. Hence, a gas cleaning and conditioning system was analysed for further application of syngas in an ICE, in particular composed by an upstream guard bed of calcined dolomite and a waste vegetable oil scrubber. The complete cleaning system resulted to be efficient, with a reduction of heavier tars of almost 100% even after 12 hours of operation. Finally, an evaluation of the global gasification system has been carried out, in order to analyse the integration of DBFB gasifier in a real plant, its performances and efficiency and to determine which are the streams and their main features (in term of composition and operating conditions) where apply the sensor investigations. It was chosen to globally analyse a biomass gasification plant for pure hydrogen production, since its higher restrictions in terms of contaminants and syngas quality and its high temperature gas conditioning steps. A sensitivity study has been carried out at different steam to biomass ratio (SB) and different water gas shift reactor operating temperature and residence time, in order to determine

their influence on syngas quality and system's performances. Results showed that the higher the SB, the higher is the hydrogen yield and also the system chemical efficiency and the electric energy need. The case with SB equal to 2.0 was the preferable one, since the higher hydrogen yield and chemical efficiency and also because it provides the better thermal energy exploitation, even if it requires additional electric energy input. Regarding WGS operating temperature and residence time, the optimum values were 300 °C and 0.8 seconds.

These experimental considerations on biomass gasification pointed out the high dependence of system's performances from input parameters and conditions. Having, therefore, a system control able to measure syngas composition and its contaminants and impurities on-line and directly in the gas stream, even at relatively high temperatures, is extremely useful for optimal operation of the plant. Thus, experimental activities on chemoresistive gas sensors have been carried out, consisting in the synthesis, characterization and test of innovative perovskite materials for sensing purposes. Firstly, preliminary studies on the auto-combustion synthesis method were conducted, by means of a theoretic determination of the optimal parameters values (e.g. combustion settings, metal complexing conditions and solutions acidity) and thanks to a multivariate analysis on the synthesis parameters influence on sensors quality (e.g. sensitivity, response time, stability and electrical characteristics). These activities allowed to optimize the synthesis method for further preparation of proper and efficient materials to be tested in the sensing properties: the suitable conditions resulted to be Φ parameter equal to 0.45, CA/M ratio set at 2.5 and pH level around 7. Successively, $LaTi_{0.4}Fe_{0.6}O_3$ was tested for different gas atmospheres. Results showed that the titanium presence in the perovskite structure is effectively profitable, mostly for carbon monoxide presence: it leads to proper sensitivity in the CO measurements and increase the thermal and chemical stability of the material respect to $LaFeO_3$. Its performances, however, resulted to be unsatisfactory for H_2S and H_2 sensing. Further researches were then carried out focused on $LaCo_xTi_wFe_zO_3$ (x+w+z=1) for H_2 sensing purposes: cobalt ions presence allows to obtain very higher sensitivity both respect to the basic lanthanum ferrite perovskite and to the titanium substituted one, even if it shifts the operating range towards slightly lower temperatures. Regarding the CO sensing, studies on the effects of the amounts of titanium ions in the lanthanum ferrite perovskite were also performed, revealing that the best materials are $LaTi_{0.2}Fe_{0.8}O_3$ and $LaTi_{0.4}Fe_{0.6}O_3$. Gas sensing

tests were performed using the “flow-through” method, perfectly comparable with real conditions as assessed by literature. In addition, a multivariate analysis on the test conditions influence on sensors responses was carried out, validating the gas sensing tests performed. Sensors analysed for CO and H_2 showed their maximum sensitivity at temperatures around 350-450 °C. Considering these investigations, it is possible to deduce that the studied gas sensors could be used in a biomass gasification system, in particular in the flue gas stream, for the determination of CO level and relative environmental limits, or at the exit of the water gas shift reactor, for the measurement of CO and H_2 syngas content in order to have an evaluation of the WGS efficiency, or on the high temperature fuel cells for safety control of hydrogen leakages.

Results obtained stressed the possibility of integration of high temperature, on-line and low cost measurement instruments in thermochemical conversion systems, thanks to the chemoresitive gas sensors perovskite based. In this way is then possible to overcome the hindrances related to the conventional analytical techniques for the monitoring of hydrocarbons and other involved gases, based on gas/liquid chromatography and mass spectrometry. Further researches are, however, necessary. In particular, suitable materials for hydrogen sulphide measurements need to be developed, together with those for higher hydrogen concentration. An additional outlook is the testing of gas sensors with a gas mixture representative of syngas and the developing of an electronic nose able to perfectly detect all the gases present in the mixtures. The nose could be made of different optimized single gas sensors as the ones tested, in order to make them selective to the specific analyte and the specific temperature. It is possible, indeed, to integrate them with temperature correction signals, for the providing of the right response relative to the operating temperature, or with particular traps for other gases present in the atmosphere different from the analyte one.

References

[1] IPCC. Summary for Policymakers. In: Stocker, T.F., D. Qin, G.-K. Plattner, M. Tignor, S.K. Allen, J. Boschung, A. Nauels, Y. Xia VB, Midgley PM, editors. Clim. Chang. 2013 Phys. Sci. Basis. Contrib. Work. Gr. I to Fifth Assess. Rep. Intergov. Panel Clim. Chang., Cambridge, United Kingdom: Cambridge University Press; 2013. doi:10.1017/CBO9781107415324.004.

[2] Report of the Millennium Ecosystem Assessment: Ecosystems and human well-being. vol. 5. Washington, DC: Island Press; 2005. doi:10.1196/annals.1439.003.

[3] The United Nation Framework Convention on Climate Change. http://unfccc.int/kyoto_protocol/items/2830.php n.d.

[4] The European Commission. https://ec.europa.eu/clima/policies/strategies/2020_en n.d.

[5] The European Commission. https://ec.europa.eu/clima/policies/strategies/2050_en n.d.

[6] The European Commision. https://ec.europa.eu/clima/policies/international/negotiations/paris_en n.d.

[7] ENEA, Baldissara B, Ciorba U, Gaeta M, Rao M, Virdis MR. Rapporto Energia e Ambiente - Scenari e Strategie. 2013.

[8] Soytas U, Sari R. Energy consumption, economic growth, and carbon emissions: Challenges faced by an EU candidate member. Ecol Econ 2009;68:1667–75. doi:10.1016/j.ecolecon.2007.06.014.

[9] Soytas U, Sari R, Ewing BT. Energy consumption, income, and carbon emissions in the United States. Ecol Econ 2007;62:482–9. doi:10.1016/j.ecolecon.2006.07.009.

[10] Fedrigo-Fazio D, ten Brink P. Briefing Green Economy – what do we mean by green economy? 2012. doi:10.1017/CBO9781107415324.004.

[11] Abbasi T, Abbasi S a. Biomass energy and the environmental impacts associated with its production and utilization. Renew Sustain Energy Rev 2010;14:919–37. doi:10.1016/j.rser.2009.11.006.

[12] Sikarwar VS, Zhao M, Clough P, Yao J, Zhong X, Memon MZ, et al. An overview of advances in biomass gasification. Energy Environ Sci 2016;9:2939–77. doi:10.1039/C6EE00935B.

[13] Pejcic B, Eadington P, Ross A. Environmental monitoring of hydrocarbons: A chemical sensor perspective. Environ Sci Technol 2007;41:6333–42. doi:10.1021/es0704535.

[14] Praveen K., Eric L.Brosha, Rangachary Mukundan FHG. Chemical Sensors for Environmental Monitoring and Homeland Security. Electrochem Soc Interface 2010:35–40.

[15] Peter M. Energy production from biomass (part 1): overview of biomass 2002;83:37–46.

[16] Lin Y-C, Huber GW. The critical role of heterogeneous catalysis in lignocellulosic biomass conversion. Energy Environ Sci 2009;2:68–80. doi:10.1039/B814955K.

[17] Dincer I. Renewable energy and sustainable development: a crucial review. Renew Sustain Energy Rev 2000;4:157–75. doi:10.1016/S1364-0321(99)00011-8.

[18] Bocci E, Di Carlo A, McPhail S, Gallucci K, Foscolo P, Moneti M, et al. Biomass to fuel cells state of the art: A review of the most innovative technology solutions. Int J

Hydrogen Energy 2014;39:21876–21895.

[19] Werther J, Saenger M, Hartge EU, Ogada T, Siagi Z. Combustion of agricultural residues. Prog Energy Combust Sci 2000;26:1–27. doi:10.1016/S0360-1285(99)00005-2.

[20] Basu P. Biomass Gasification and Pyrolysis Handbook. 2010. doi:http://dx.doi.org/10.1016/B978-0-12-374988-8.00001-5.

[21] McKendry P. Energy production from biomass (part 2): conversion technologies. Bioresour Technol 2002;83:47–54. doi:Pii S0960-8524(01)00119-5\rDoi 10.1016/S0960-8524(01)00119-5.

[22] Bocci E, Sisinni M, Moneti M, Vecchione L, Di Carlo A, Villarini M. State of Art of Small Scale Biomass Gasification Power Systems: A Review of the Different Typologies. Energy Procedia 2014;45:247–256.

[23] Mckendry P. Energy production from biomass (part 3): gasification technologies. Bioresour Technol 2002;83:55–63.

[24] Bridgwater A. Renewable fuels and chemicals by thermal processing of biomass. Chem Eng J 2003;91:87–102. doi:10.1016/S1385-8947(02)00142-0.

[25] Balat M, Balat M, Kirtay E, Balat H. Main routes for the thermo-conversion of biomass into fuels and chemicals. Part 2: Gasification systems. Energy Convers Manag 2009;50:3158–68. doi:10.1016/j.enconman.2009.08.013.

[26] Boerrigter H, Rauch R. Review of applications of gases from biomass gasification. In: HAM K, editor. Hanb. Biomass Gasif., The Netherlands Biomass Technology Group (BTG); 2005, p. 21–30.

[27] Beheshti SM, Ghassemi H, Shahsavan-Markadeh R. Process simulation of biomass gasification in a bubbling fluidized bed reactor. Energy Convers Manag 2015;94:345–52. doi:10.1016/j.enconman.2015.01.060.

[28] Le CD. Gasification of biomass: an investigation of key challenges to advance acceptance of the technology. University of Bath, 2012.

[29] Bang-Møller C, Rokni M. Thermodynamic performance study of biomass gasification, solid oxide fuel cell and micro gas turbine hybrid systems. Energy Convers Manag 2010;51:2330–9. doi:10.1016/j.enconman.2010.04.006.

[30] Gabra M, Pettersson E, Backman R, Kjellstr??m B. Evaluation of cyclone gasifier performance for gasification of sugar cane residue - Part 1: Gasification of bagasse. Biomass and Bioenergy 2001;21:351–69. doi:10.1016/S0961-9534(01)00043-5.

[31] Hasler P, Nussbaumer T. Gas cleaning for IC engine applications from fixed bed biomass gasification. Biomass and Bioenergy 1999;16:385–95. doi:10.1016/S0961-9534(99)00018-5.

[32] Wang L, Weller CL, Jones DD, Hanna M a. Contemporary issues in thermal gasification of biomass and its application to electricity and fuel production. Biomass and Bioenergy 2008;32:573–81. doi:10.1016/j.biombioe.2007.12.007.

[33] Brammer JG, Bridgwater a. V. The influence of feedstock drying on the performance and economics of a biomass gasifier - Engine CHP system. Biomass and Bioenergy 2002;22:271–81. doi:10.1016/S0961-9534(02)00003-X.

[34] van der Stelt MJC, Gerhauser H, Kiel JH a, Ptasinski KJ. Biomass upgrading by torrefaction for the production of biofuels: A review. Biomass and Bioenergy

2011;35:3748–62. doi:10.1016/j.biombioe.2011.06.023.

[35] Tijmensen MJ a, Faaij a. PC, Hamelinck CN, Van Hardeveld MRM. Exploration of the possibilities for production of Fischer Tropsch liquids and power via biomass gasification. Biomass and Bioenergy 2002;23:129–52. doi:10.1016/S0961-9534(02)00037-5.

[36] Shen L, Gao Y, Xiao J. Simulation of hydrogen production from biomass gasification in interconnected fluidized beds. Biomass and Bioenergy 2008;32:120–7. doi:10.1016/j.biombioe.2007.08.002.

[37] Song T, Wu J, Shen L, Xiao J. Experimental investigation on hydrogen production from biomass gasification in interconnected fluidized beds. Biomass and Bioenergy 2012;36:258–67. doi:10.1016/j.biombioe.2011.10.021.

[38] Knoef H, Ahrenfeldt J. Handbook biomass gasification. The Netherlands: BTG Biomass Technology Group; 2005.

[39] Umeki K, Yamamoto K, Namioka T, Yoshikawa K. High temperature steam-only gasification of woody biomass. Appl Energy 2010;87:791–8. doi:10.1016/j.apenergy.2009.09.035.

[40] Chen W-H, Chen C-J, Hung C-I, Shen C-H, Hsu H-W. A comparison of gasification phenomena among raw biomass, torrefied biomass and coal in an entrained-flow reactor. Appl Energy 2013;112:421–30. doi:10.1016/j.apenergy.2013.01.034.

[41] Rapagnà S, Jand N, Kiennemann a., Foscolo PU. Steam-gasification of biomass in a fluidised-bed of olivine particles. Biomass and Bioenergy 2000;19:187–97. doi:10.1016/S0961-9534(00)00031-3.

[42] Li XT, Grace JR, Lim CJ, Watkinson AP, Chen HP, Kim JR. Biomass gasification in a circulating fluidized bed. Biomass and Bioenergy 2004;26:171–93. doi:10.1016/S0961-9534(03)00084-9.

[43] Meng X, de Jong W, Fu N, Verkooijen AHM. Biomass gasification in a 100 kWth steam-oxygen blown circulating fluidized bed gasifier: Effects of operational conditions on product gas distribution and tar formation. Biomass and Bioenergy 2011;35:2910–24. doi:10.1016/j.biombioe.2011.03.028.

[44] Mondal P, Dang GS, Garg MO. Syngas production through gasification and cleanup for downstream applications — Recent developments. Fuel Process Technol 2011;92:1395–410. doi:10.1016/j.fuproc.2011.03.021.

[45] Milne TA, Abatzoglou N, Evans RJ. Biomass gasifier“ tars”: their nature, formation, and conversion. vol. 570. National Renewable Energy Laboratory Golden, CO; 1998.

[46] Olofsson I, Nordin A, Söderlind U. Initial Review and Evaluation of Process Technologies and Systems Suitable for Cost-Efficient Medium-Scale Gasification for Biomass to Liquid Fuels. Umeå; 2005.

[47] Gil J, Aznar MP, Caballero MA, Francés E, Corella J. Biomass Gasification in Fluidized Bed at Pilot Scale with Steam−Oxygen Mixtures. Product Distribution for Very Different Operating Conditions. Energy & Fuels 1997;11:1109–18. doi:10.1021/ef9602335.

[48] Hofbauer H, Knoef H. Success stories on biomass gasification. Handb Biomass Gasification BTG Biomass Technol Group, Enschede, Netherlands 2005:115–161.

[49] Hofbauer H, Rauch R, Bosch K, Koch R, Aichernig C. Biomass CHP Plant Güssing - A Success Story. Proc. Expert Meet. pyrolysis Gasif. biomass waste, Strasbourg: 2002.

[50] Hofbauer H, Rauch R, Loeffler G, Kaiser S, Fercher E, Tremmel H. Six years experience with the FICFB-gasification process. 12th Eur. Conf. Technol. Exhib. Biomass Energy, Ind. Clim. Prot., Amsterdam, The Netherlands: 2002, p. 982–985.

[51] Paisley MA. Commercial development of the Battelle/FERCO biomass gasification process in McNeil gasifier. Proc. 3rd Biomass Conf. Am., 1997.

[52] Pieratti E. Biomass gasification in small scale plants : experimental and modelling analysis. 2011.

[53] VVBGC. http://www.vvbgc.se/ 2010.

[54] Granatstein DL. Case study on waste-fuelled gasification project greve in Chianti, Italy, Task 36, Report, IEA Bioenergy Agreement. 2003.

[55] Barisano D, Canneto G, Nanna F, Alvino E, Pinto G, Villone A, et al. Steam/oxygen biomass gasification at pilot scale in an internally circulating bubbling fluidized bed reactor. Fuel Process Technol 2016;141:74–81. doi:10.1016/j.fuproc.2015.06.008.

[56] Pieratti E, Baratieri M, Baggio P, Grigiante M, Ceschini S. A biomass steam gasification pilot plant: syngas suitability for SOFC stacks. Proc. 3rd Int. Conf. Eng. Waste Biomass Valoris., Beijing, China: 2010.

[57] Baggio P, Baratieri M, Fiori L, Grigiante M, Avi D, Tosi P. Experimental and modeling analysis of a batch gasification/pyrolysis reactor. Energy Convers Manag 2009;50:1426–35. doi:10.1016/j.enconman.2009.03.004.

[58] Orecchini F, Bocci E. Biomass to hydrogen for the realization of closed cycles of energy resources. Energy 2007;32:1006–1011.

[59] Pari L. Energy production from biomass : the case of Italy 2001;22:21–30.

[60] Bocci E, Di Carlo A, Vecchione L, Villarini M, De Falco M, Dell'Era A. Technical-Economic Analysis of an Innovative Cogenerative Small Scale Biomass Gasification Power Plant. Comput Sci Its Appl 2013 2013:256–270.

[61] Rabou LPLM, Zwart RWR, Vreugdenhil BJ, Bos L. Tar in biomass producer gas, the Energy research Centre of The Netherlands (ECN) experience: An enduring challenge. Energy and Fuels 2009;23:6189–98. doi:10.1021/ef9007032.

[62] Van Paasen SVB, Kiel JHA, Veringa HJ. Tar Formation in a Fluidised Bed Gasifier. Report ECN-C--04-013. 2004.

[63] Bridgwater A V. The technical and economic feasibility of biomass gasif ication for power generation. Fuel 1995;14:631–53. doi:10.1016/0016-2361(95)00001-L.

[64] Devi L, Ptasinski KJ, Janssen FJJG. A review of the primary measures for tar elimination in biomass gasification processes. Biomass and Bioenergy 2002;24:125–40. doi:10.1016/S0961-9534(02)00102-2.

[65] Bergman P, van Paasen S, Boerrigter H. The novel "OLGA" technology for complete tar removal from biomass producer gas. Pyrolysis Gasif Biomass Waste 2002:10.

[66] Delgado J, Aznar MP, Corella J. Calcined dolomite, magnesite, and calcite for cleaning hot gas from a fluidized bed biomass gasifier with steam: life and usefulness. Ind Eng Chem Res 1996;35:3637–3643.

[67] Phuphuakrat T, Namioka T, Yoshikawa K. Tar removal from biomass pyrolysis gas in two-step function of decomposition and adsorption. Appl Energy 2010;87:2203–11. doi:10.1016/j.apenergy.2009.12.002.

[68] Narváez I, Orío A, Aznar MP, Corella J. Biomass Gasification with Air in an

Atmospheric Bubbling Fluidized Bed. Effect of Six Operational Variables on the Quality of the Produced Raw Gas. Ind Eng Chem Res 1996;35:2110–20. doi:10.1021/ie9507540.

[69] Corella J, Orio A, Toledo JM. Biomass gasification with air in a fluidized bed: Exhaustive tar elimination with commercial steam reforming catalysts. Energy and Fuels 1999;13:702–9. doi:10.1021/ef980221e.

[70] Di Carlo A, Savuto E, Foscolo PU, D'Orazio A, Bocci E. CFD model of the gasifier with catalytic filter candles in the freeboard, Deliverable 6.3, Confidental report, UNIFHY Project #299732 in FP7. 2015.

[71] D'Orazio a., Rapagnà S, Foscolo PU, Gallucci K, Nacken M, Heidenreich S, et al. Gas conditioning in H2 rich syngas production by biomass steam gasification: Experimental comparison between three innovative ceramic filter candles. Int J Hydrogen Energy 2015;40:7282–90. doi:10.1016/j.ijhydene.2015.03.169.

[72] Dogru M, Midilli A, Howarth CR. Gasification of sewage sludge using a throated downdraft gasifier and uncertainty analysis. Fuel Process Technol 2002;75:55–82. doi:10.1016/S0378-3820(01)00234-X.

[73] Koppatz S, Pfeifer C, Rauch R, Hofbauer H, Marquard-Moellenstedt T, Specht M. H2 rich product gas by steam gasification of biomass with in situ CO2 absorption in a dual fluidized bed system of 8 MW fuel input. Fuel Process Technol 2009;90:914–21. doi:10.1016/j.fuproc.2009.03.016.

[74] Malkow T. Novel and innovative pyrolysis and gasification technologies for energy efficient and environmentally sound MSW disposal. Waste Manag 2004;24:53–79. doi:10.1016/S0956-053X(03)00038-2.

[75] Wang LK, Pereira NC, Hung Y-T, Li KH. Air pollution control engineering. vol. 1. Springer; 2004.

[76] Pfeifer C, Rauch R, Hofbauer H. In-Bed Catalytic Tar Reduction in a Dual Fluidized Bed Biomass Steam Gasifier. Ind Eng Chem Res 2004;43:1634–40. doi:10.1021/ie030742b.

[77] Könemann HWJ, Van Paasen SVB. OLGA tar removal technology: 4 MW commercial demonstration. Dahlman, Pap. Present. 15th Eur. biomass Conf. Berlin, 2007.

[78] Phuphuakrat T, Namioka T, Yoshikawa K. Absorptive removal of biomass tar using water and oily materials. Bioresour Technol 2011;102:543–9. doi:10.1016/j.biortech.2010.07.073.

[79] Corella J, Toledo JM, Padilla R. Olivine or dolomite as in-bed additive in biomass gasification with air in a fluidized bed: Which is better? Energy and Fuels 2004;18:713–20. doi:10.1021/ef0340918.

[80] Corella J, Aznar MP, Gil J, Caballero M a. Biomass gasification in fluidised bed: where to locate the dolomite to improve gasification? Energy and Fuels 1999;13:1122–7.

[81] Delgado J, Aznar MP, Corella J. Biomass gasification with steam in fluidized bed: Effectiveness of CaO, MgO, and CaO-MgO for hot raw gas cleaning. Ind Eng Chem Res 1997;36:1535–1543.

[82] Caballero MA, Corella J, Aznar M-P, Gil J. Biomass Gasification with Air in Fluidized Bed. Hot Gas Cleanup with Selected Commercial and Full-Size Nickel-

Based Catalysts. Ind Eng Chem Res 2000;39:1143–54. doi:10.1021/ie990738t.

[83] Simell P, Kurkela E, Ståhlberg P, Hepola J. Catalytic hot gas cleaning of gasification gas. Catal Today 1996;27:55–62. doi:10.1016/0920-5861(95)00172-7.

[84] Zhang R, Wang Y, Brown RC. Steam reforming of tar compounds over Ni/olivine catalysts doped with CeO2. Energy Convers Manag 2007;48:68–77. doi:10.1016/j.enconman.2006.05.001.

[85] Savuto E, Di Carlo a., Gallucci K, Natali S, Bocci E. Characterization and performance analysis of an innovative Ni/Mayenite catalyst for the steam reforming of raw syngas. Fuel 2017;194:348–56. doi:10.1016/j.fuel.2017.01.022.

[86] Rapagna S, Jand N, Foscolo PU. Catalytic gasification of biomass to produce hydrogen rich gas. Int J Hydrog Energyt J Hydrog Energy 1998;23:551–7. doi:10.1016/S0360-3199(97)00108-0.

[87] UNIQUE Cooperative Research Project, Contract N.211517 7FP, n.d.

[88] Rapagna S, D'orazio A, Gallucci K, Foscolo PU, Nacken M, Heidenreich S. Hydrogen rich gas from catalytic steam gasification of biomass in a fluidized bed containing catalytic filters. Chem Eng Trans 2014;37:157–62.

[89] Heidenreich S, Nacken M, Foscolo PU, Rapagna S. Gasification apparatus and method for generating syngas from gasifiable feedstock material. U.S. Patent Application US 2010/0223848 A1, 2010.

[90] Clayton SJ, Stiegel GJ, Wimer JG. DOE/FE-0447. 2002.

[91] Vandecruys F, Brauns E, Engelen W, Schutter F De, Vangrunderbeek J. A H2 sensor for on-line measurements in a coal gasification system 1998;112:95–102.

[92] Sur R, Sun K, Jeffries JB, Hanson RK, Pummill RJ, Waind T, et al. TDLAS-based sensors for in situ measurement of syngas composition in a pressurized, oxygen-blown, entrained flow coal gasifier. Appl Phys B Lasers Opt 2014;116:33–42. doi:10.1007/s00340-013-5644-6.

[93] Aroutiounian V. Metal oxide hydrogen, oxygen, and carbon monoxide sensors for hydrogen setups and cells. Int J Hydrogen Energy 2007;32:1145–58. doi:10.1016/j.ijhydene.2007.01.004.

[94] Nussbaumer T. Combustion and Co-combustion of Biomass: Fundamentals, Technologies, and Primary Measures for Emission Reduction. Energy and Fuels 2003;17:1510–21. doi:10.1021/ef030031q.

[95] The European Commision. European Directive 2008/50/EC 2008.

[96] Italian Government. Italian Directive DLgs 155/2010 2010.

[97] Colpan CO, Hamdullahpur F, Dincer I, Yoo Y. Effect of gasification agent on the performance of solid oxide fuel cell and biomass gasification systems. Int J Hydrogen Energy 2010;35:5001–9. doi:10.1016/j.ijhydene.2009.08.083.

[98] Nagel FP, Schildhauer TJ, Biollaz SMA. Biomass-integrated gasification fuel cell systems - Part 1: Definition of systems and technical analysis. Int J Hydrogen Energy 2009;34:6809–25. doi:10.1016/j.ijhydene.2009.05.125.

[99] Hofmann P, Panopoulos KD, Fryda LE, Schweiger A, Ouweltjes JP, Karl J. Integrating biomass gasification with solid oxide fuel cells: Effect of real product gas tars, fluctuations and particulates on Ni-GDC anode. Int J Hydrogen Energy 2008;33:2834–44. doi:10.1016/j.ijhydene.2008.03.020.

[100] Dornburg V, Faaij APC. Efficiency and economy of wood-fired biomass energy systems in relation to scale regarding heat and power generation using combustion and gasification technologies. Biomass and Bioenergy 2001;21:91–108. doi:10.1016/S0961-9534(01)00030-7.

[101] Di Carlo A, Borello D, Bocci E. Process simulation of a hybrid SOFC/mGT and enriched air/steam fluidized bed gasifier power plant. Int J Hydrogen Energy 2013;38:5857–74. doi:10.1016/j.ijhydene.2013.03.005.

[102] Di Carlo A, Bocci E, Naso V. Process simulation of a SOFC and double bubbling fluidized bed gasifier power plant. Int J Hydrogen Energy 2013;38:532–42.

[103] Toonssen R, Woudstra N, Verkooijen AHM. Exergy analysis of hydrogen production plants based on biomass gasification. Int J Hydrogen Energy 2008;33:4074–82. doi:10.1016/j.ijhydene.2008.05.059.

[104] Balthasar W, Hambleton D. Industrial scale production of hydrogen from natural gas, naphtha and coal. Int J Hydrogen Energy 1980;5:21–33. doi:10.1016/0360-3199(80)90112-3.

[105] Spencer MS. The role of zinc oxide in Cu/ZnO catalysts for methanol synthesis and the water–gas shift reaction. Top Catal 1999;8:259–66. doi:10.1023/A:1019181715731.

[106] U.S. Department of Energy. Fuel Cell Handbook (7th edition) 2004.

[107] Zaza F, Paoletti C, Lopresti R, Simonetti E, Pasquali M. Multiple regression analysis of hydrogen sulphide poisoning in molten carbonate fuel cells used for waste-to-energy conversions. Int J Hydrogen Energy 2011;36:8119–25. doi:10.1016/j.ijhydene.2011.01.174.

[108] Zheng LL, Wang X, Zhang L, Wang JY, Jiang SP. Effect of Pd-impregnation on performance, sulfur poisoning and tolerance of Ni/GDC anode of solid oxide fuel cells. Int J Hydrogen Energy 2012;37:10299–310. doi:10.1016/j.ijhydene.2012.03.105.

[109] Devianto H, Simonetti E, McPhail SJ, Zaza F, Cigolotti V, Paoletti C, et al. Electrochemical impedance study of the poisoning behaviour of Ni-based anodes at low concentrations of H2S in an MCFC. Int J Hydrogen Energy 2012;37:19312–8. doi:10.1016/j.ijhydene.2012.03.110.

[110] Palmisano V, Boon-Brett L, Bonato C, Harskamp F, Buttner WJ, Post MB, et al. Evaluation of selectivity of commercial hydrogen sensors. Int J Hydrogen Energy 2014;39:20491–6. doi:10.1016/j.ijhydene.2014.03.251.

[111] Buttner WJ, Post MB, Burgess R, Rivkin C. An overview of hydrogen safety sensors and requirements. Int J Hydrogen Energy 2011;36:2462–70. doi:10.1016/j.ijhydene.2010.04.176.

[112] Boon-Brett L, Bousek J, Moretto P. Reliability of commercially available hydrogen sensors for detection of hydrogen at critical concentrations: Part II - selected sensor test results. Int J Hydrogen Energy 2009;34:562–71. doi:10.1016/j.ijhydene.2008.10.033.

[113] Hulanicki A, Glab S, Ingman F. Chemical sensors: definitions and classification. Pure Appl Chem 1991;63:1247–50. doi:10.1351/pac199163091247.

[114] Hübert T, Boon-Brett L, Buttner WJ. Sensors for safety and process control in hydrogen technologies. Boca Raton, FL: CRC Press; 2016.

[115] Bochenkov VE, Sergeev GB. Sensitivity, Selectivity, and Stability of Gas-Sensitive

Metal-Oxide Nanostructures. In: Umar A, Hahn Y-B, editors. Met. Oxide Nanostructures Their Appl., vol. 3, American Scientific Publishers; 2010, p. 31–52.

[116] Sze SM. Physics of Semiconductor Devices. New York, USA: John Wiley & Sons, Inc; 1969. doi:10.1049/ep.1970.0039.

[117] Fraden J. Handbook of Modern Sensors: physics, designs, and applications. vol. 53. 3rd ed. New York, USA: Springer-Verlag New York, Inc.; 2013. doi:10.1017/CBO9781107415324.004.

[118] Ho CK, Itamura MT, Kelley MJ, Hughes RC. Review of Chemical Sensors for In-Situ Monitoring of Volatile Contaminants, Sandia Report. 2001. doi:10.2172/780299.

[119] Sberveglieri G. Gas sensors. Boston, MA: Kluwer Academic Publisher; 1992.

[120] Chou J. Hazardous Gas Monitors: A Practical Guide to Selection, Operation and Applications. New York, USA: McGraw-Hill; 2000.

[121] Capone S, National I, Rella R, National I, Italian S, Aging A, et al. Solid State Gas Sensors : State of the Art and Future Activities. J Optoelectron Adv Mater 2003;5:1335–48. doi:10.1002/chin.200429283.

[122] Gardner JW, Bartlett PN. Electronic noses – Principles and Applications. Oxford: Oxford University Press; 1999.

[123] Gardner JW, Persaud KC. Electronic Noses and Olfaction 2000. 7th Symp. Olfaction Electron. Noses, Brighton, UK: IOP Publishing; n.d.

[124] Mielle P, Marquis F, Latrasse C. Electronic noses: specify or disappear. Sensors Actuators, B Chem 2000;69:287–94. doi:10.1016/S0925-4005(00)00509-8.

[125] Janata J. Principles of Chemical Sensors. 2nd ed. New York, USA: Springer Science+Business Media; 2009. doi:10.1007/b136378.

[126] Gründler P. Chemical sensors: An introduction for scientists and engineers. Berlin: Springer-Verlag Berlin Heidelberg; 2007. doi:10.1007/978-3-540-45743-5.

[127] Korotcenkov G. Metal oxides for solid-state gas sensors: What determines our choice? Mater Sci Eng B Solid-State Mater Adv Technol 2007;139:1–23. doi:10.1016/j.mseb.2007.01.044.

[128] Gopel W, Hesse J, Zemel JN. Sensors, A comprhensive survey. New York, USA: VCH Publisher Inc.; 1991.

[129] Gran View Research. http://www.grandviewresearch.com/press-release/global-gas-sensors-market n.d.

[130] Azo Sensors. https://www.azosensors.com/news.aspx?newsID=10346 2015.

[131] Bcc Research. https://www.bccresearch.com/pressroom/ias/global-market-sensors-worth-$91.5-billion-2016 2011.

[132] Korotcenkov G. Chemical sensors: comprehensive sensor technologies, Vol. 6 Chemical sensors applications. New York, USA: Momentum Press; 2011.

[133] Wohltjen H, Barger WR, Snow a. W, Jarvis NL. A vapor-sensitive chemiresistor fabricated with planar microelectrodes and a Langmuir-Blodgett organic semiconductor film. IEEE Trans Electron Devices 1985;32:1170–4. doi:10.1109/T-ED.1985.22095.

[134] Madou MJ, Morrison SR. Chemical sensing with solid state devices. Boston (MA): Academic Press; 1989. doi:http://dx.doi.org/10.1016/B978-0-12-464965-1.50001-6.

[135] Simon I, Bârsan N, Bauer M, Weimar U. Micromachined metal oxide gas sensors: Opportunities to improve sensor performance. Sensors Actuators, B Chem 2001;73:1–26. doi:10.1016/S0925-4005(00)00639-0.

[136] Inc. FE. Figaro Products Catalogue, Figaro gas sensors 1-series 8-series n.d.

[137] Fine GF, Cavanagh LM, Afonja A, Binions R. Metal oxide semi-conductor gas sensors in environmental monitoring. Sensors 2010;10:5469–502. doi:10.3390/s100605469.

[138] Kim ID, Rothschild A, Tuller HL. Advances and new directions in gas-sensing devices. Acta Mater 2013;61:974–1000. doi:10.1016/j.actamat.2012.10.041.

[139] Fierro JLG. Metal Oxide, Chemistry and Applications. Boca: CRC Press; 2006. doi:10.1007/978-1-4419-9931-3.

[140] Barsan N, Koziej D, Weimar U. Metal oxide-based gas sensor research: How to? Sensors Actuators, B Chem 2007;121:18–35. doi:10.1016/j.snb.2006.09.047.

[141] Eranna G, Joshi BC, Runthala DP, Gupta RP. Oxide materials for development of integrated gas sensors - A comprehensive review. Crit Rev Solid State Mater Sci 2004;29:111–88. doi:10.1080/10408430490888977.

[142] Yamazoe N, Shimanoe K. New perspectives of gas sensor technology. Sensors Actuators, B Chem 2009;138:100–7. doi:10.1016/j.snb.2009.01.023.

[143] Korotcenkov G. Gas response control through structural and chemical modification of metal oxide films: State of the art and approaches. Sensors Actuators, B Chem 2005;107:209–32. doi:10.1016/j.snb.2004.10.006.

[144] Park CO, Akbar SA. Ceramics for chemical sensing. J Mater Sci 2003;38:4611–37. doi:10.1023/A:1027402430153.

[145] Yamazoe N, Sakai G, Shimanoe K. Oxide semiconductor gas sensors. Catal Surv from Asia 2003;7:63–75. doi:10.1023/A:1023436725457.

[146] Smith AM, Nie S. Semiconductor Nanocrystals: Structure, Properties, and Band Gap Engineering. Acc Chem Res 2010;43:190–200. doi:10.1021/ar9001069.Semiconductor.

[147] Xu CH, Shi SQ, Surya C. Gas Sensors Based on One-Dimensional Nanostructures. Sensors (Peterborough, NH) 2008;XX.

[148] Comini E, Baratto C, Concina I, Faglia G, Falasconi M, Ferroni M, et al. Metal oxide nanoscience and nanotechnology for chemical sensors. Sensors Actuators, B Chem 2013;179:3–20. doi:10.1016/j.snb.2012.10.027.

[149] Gurlo A. Nanosensors: towards morphological control of gas sensing activity. SnO2 , In2O3 , ZnO and WO3 case studies. Nanoscale 2011;3:154–65. doi:10.1039/C0NR00560F.

[150] Orton JW, Powell MJ. The Hall Effect in Polycrystalline and Powdered Semiconductors. Rep Prog Phys 1980;43:1263–307.

[151] Rothschild A, Komem Y. The effect of grain size on the sensitivity of nanocrystalline metal-oxide gas sensors. J Appl Phys 2004;95:6374–80. doi:10.1063/1.1728314.

[152] Rothschild A, Komem Y. On the relationship between the grain size and gas-sensitivity of chemo-resistive metal-oxide gas sensors with nanosized grains. J Electroceramics 2004;13:697–701. doi:10.1007/s10832-004-5178-8.

[153] Wang W. Advances in Chemical Sensors. Rijeka, Croatia: InTech; 2011.

[154] Barsan N, Simion C, Heine T, Pokhrel S, Weimar U. Modeling of sensing and transduction for p-type semiconducting metal oxide based gas sensors. J Electroceramics 2010;25:11–9. doi:10.1007/s10832-009-9583-x.

[155] Wang C, Yin L, Zhang L, Xiang D, Gao R. Metal oxide gas sensors: Sensitivity and influencing factors. Sensors 2010;10:2088–106. doi:10.3390/s100302088.

[156] Yamazoe N, Shimanoe K. Theory of power laws for semiconductor gas sensors. Sensors Actuators, B Chem 2008;128:566–73. doi:10.1016/j.snb.2007.07.036.

[157] Mizsei J. How can sensitive and selective semiconductor gas sensors be made? Sens Actuators, B 1995;23:173–6. doi:10.1016/0925-4005(94)01269-n.

[158] Pokhrel S, Simion CE, Quemener V, Bârsan N, Weimar U. Investigations of conduction mechanism in Cr2O3 gas sensing thick films by ac impedance spectroscopy and work function changes measurements. Sensors Actuators, B Chem 2008;133:78–83. doi:10.1016/j.snb.2008.01.054.

[159] Tejuca LG, Fierro JLG, Tascón JMD. Structure and Reactivity of Perovskite-Type Oxides. Adv Catal 1989;36:237–328. doi:10.1016/S0360-0564(08)60019-X.

[160] Pena M a, Fierro JLG. Chemical structures and performances of perovskite oxides. Chem Rev 2001;101:1981–2017. doi:10.1021/cr980129f.

[161] Bukhari SM. New Perovskite Materials for Sensors and Low Temperature Solid Oxide Fuel Cell (LT-SOFC) Applications. University of Ottawa, 2011.

[162] Baran EJ. Structural chemistry and physicochemical properties of perovskite-like materials. Catal Today 1990;8:133–51.

[163] Ishihara T. Perovskite Oxide for Solid Oxide Fuel Cells. New York, USA: Springer Science+Business Media; 2009.

[164] Bhalla AS, Guo R, Roy R. The perovskite structure - a review of its role in ceramic science and technology. Mater Res Innov 2000;4:3–26. doi:10.1007/s100190000062.

[165] Voorhoeve RJH, Johnson DWJ, Remeika JP, Gallagher PK. Perovskite Oxides: Materials Science in Catalysis. Science (80-) 1977;195:827–33.

[166] Raveau B. Numerous structures of oxides can be built up from the ReO3-type framework. Proc Indian Natn Sci Acad 1986;1:66–101.

[167] Kay Yoth M. Magnetic properties of Sr2YRu1-xIrxO6 compunds. San Diego State University, 2013.

[168] Goldschmidt V. Die Gesetze der Krystallochemie. Naturwissenschaften 1926;14:477–85.

[169] Fergus JW. Perovskite oxides for semiconductor-based gas sensors. Sensors Actuators, B Chem 2007;123:1169–79. doi:10.1016/j.snb.2006.10.051.

[170] Arakawa T, Kurachi H, Shiokawa J. Physicochemical properties of rare earth perovskite oxides used as gas sensor material. J Mater Sci 1985;20:1207–10. doi:10.1007/BF01026315.

[171] J. Cerdà, , J. Arbiol, G. Dezanneau, R. Díaz JRM. Perovskite-type BaSnO3 powders for high temperature gas sensor applications. Sensors Actuators B Chem 2002;84:21–5. doi:10.1016/S0925-4005(02)00005-9.

[172] Martinelli G, Carotta MC, Ferroni M, Sadaoka Y, Traversa E. Screen-printed perovskite-type thick films as gas sensors for environmental monitoring. Sensors Actuators, B Chem 1999;55:99–110. doi:10.1016/S0925-4005(99)00054-4.

[173] Perego C, Villa P. Catalyst preparation methods. Catal Today 1997;34:281–305. doi:10.1016/S0920-5861(96)00055-7.

[174] Cousin P, Ross RA. Preparation of mixed oxides: a review. Mater Sci Eng A 1990;130:119–25. doi:10.1016/0921-5093(90)90087-J.

[175] Zhang L. Preparation of Multi-Component Ceramic Nanoparticles. 2004.

[176] Idrees M, Nadeem M, Siddiqi SA, Ahmad R, Hussnain A, Mehmood M. The organic residue and synthesis of LaFeO3 by combustion of citrate and nitrate precursors. Mater Chem Phys 2015;162:652–8. doi:10.1016/j.matchemphys.2015.06.039.

[177] Wærnhus I, Vullum PE, Holmestad R, Grande T, Wiik K. Electronic properties of polycrystalline LaFeO3. Part I: Experimental results and the qualitative role of Schottky defects. Solid State Ionics 2005;176:2783–90. doi:10.1016/j.ssi.2005.08.012.

[178] Feng J, Liu T, Xu Y, Zhao J, He Y. Effects of PVA content on the synthesis of LaFeO 3 via sol – gel route 2011;37:0–4. doi:10.1016/j.ceramint.2010.11.045.

[179] Qi X, Zhou J, Yue Z, Gui Z, Li L. Auto-combustion synthesis of nanocrystalline LaFeO 3. Mater Chem Phys 2003;78:25–9.

[180] Wang X, Qin H, Sun L, Hu J. CO2 sensing properties and mechanism of nanocrystalline LaFeO3 sensor. Sensors Actuators, B Chem 2013;188:965–71. doi:10.1016/j.snb.2013.07.100.

[181] Iwasaki K, Ito T, Yoshino M, Matsui T, Nagasaki T, Arita Y. Power factor of La1-xSrxFeO3 and LaFe1-yNiyO3. J Alloys Compd 2007;430:297–301. doi:10.1016/j.jallcom.2006.05.012.

[182] Tascón JMD, Tejuca LG, Rochester CH. Surface interactions of NO and CO with LaMO3 oxides. J Catal 1985;95:558–66. doi:10.1016/0021-9517(85)90134-4.

[183] Giang HT, Duy HT, Ngan PQ, Thai GH, Thu DTA, Thu DT, et al. Hydrocarbon gas sensing of nano-crystalline perovskite oxides LnFeO3 (Ln = La, Nd and Sm). Sensors Actuators, B Chem 2011;158:246–51. doi:10.1016/j.snb.2011.06.013.

[184] Tejuca LG, Fierro JLG. Properties and applications of perovskite-type oxides. New York, USA: Marcel Dekker, Inc.; 1993.

[185] Haron W, Wisitsoraat A, Wongnawa S. Nanostructured perovskite oxides – LaMO3 (M=Al, Co, Fe) prepared by co-precipitation method and their ethanol-sensing characteristics. Ceram Int 2017;43:5032–40. doi:10.1016/j.ceramint.2017.01.013.

[186] Bai S, Shi B, Ma L, Yang P, Liu Z, Li D, et al. Synthesis of LaFeO3 catalytic materials and their sensing properties. Sci China, Ser B Chem 2009;52:2106–13. doi:10.1007/s11426-009-0289-3.

[187] Bidrawn F, Lee S, Vohs JM, Gorte RJ. The Effect of Ca, Sr, and Ba Doping on the Ionic Conductivity and Cathode Performance of LaFeO[sub 3]. J Electrochem Soc 2008;155:B660. doi:10.1149/1.2907431.

[188] Kojima I, Adachi H, Yasumori I. Electronic structures of the LaBO3 (B=Co, Fe, Al) perovskite oxides related to their catalysis. Surf Sci 1983;130:50–62.

[189] Crespin M, Hall WK. The surface chemistry of some perovskite oxides. J Catal 1981;69:359–70. doi:10.1016/0021-9517(81)90171-8.

[190] Du X, Wang Y, Mu Y, Gui L, Wang P. A New Highly Selective H2 Sensor Based on TiO2/PtO-Pt Dual-Layer Films. Thin Solid Films 2002;8:3953–7. doi:10.1021/cm0201293.

[191] Phokha S, Pinitsoontorn S, Rujirawat S, Maensiri S. Polymerized complex synthesis and effect of Ti dopant on magnetic properties of LaFeO3 nanoparticles. J Nanosci Nanotechnol 2015;15:9171–7. doi:10.1166/jnn.2015.11407.

[192] Good J, Ventress L, Knoef H, Group BT, Zielke U, Hansen PL, et al. Sampling and analysis of tar and particles in biomass producer gases 2005;20002:1–44.

[193] Villarini M, Bocci E, Di Carlo A, Savuto E, Pallozzi V. The case study of an innovative small scale biomass waste gasification heat and power plant contextualized in a farm. Energy Procedia 2015;82:335–42. doi:10.1016/j.egypro.2015.11.790.

[194] Pang CH, Hewakandamby B, Wu T, Lester E. An automated ash fusion test for characterisation of the behaviour of ashes from biomass and coal at elevated temperatures. Fuel 2013;103:454–66. doi:10.1016/j.fuel.2012.06.120.

[195] Olanders B, Steenari BM. Characterization of ashes from wood and straw. Biomass and Bioenergy 1995;8:105–15. doi:10.1016/0961-9534(95)00004-Q.

[196] Demirbaş A. Heavy Metal Contents of Fly Ashes from Selected Biomass Samples. Energy Sources 2005;27:1269–76. doi:10.1080/009083190519384.

[197] Gao N, Li A, Quan C, Gao F. Hydrogen-rich gas production from biomass steam gasification in an updraft fixed-bed gasifier combined with a porous ceramic reformer. Int J Hydrogen Energy 2008;33:5430–8.

[198] Huang Z, He F, Zheng A, Zhao K, Chang S, Zhao Z, et al. Synthesis gas production from biomass gasification using steam coupling with natural hematite as oxygen carrier. Energy 2013;53:244–51.

[199] Nikoo MB, Mahinpey N. Simulation of biomass gasification in fluidized bed reactor using ASPEN PLUS. Biomass and Bioenergy 2008;32:1245–54. doi:10.1016/j.biombioe.2008.02.020.

[200] ECN. Thersites the ECN tar dew point site, http://www.thersites.nl/completemodel.aspx n.d.

[201] Pallozzi V, Di Carlo A, Bocci E, Carlini M. Combined gas conditioning and cleaning for reduction of tars in biomass gasification. Biomass and Bioenergy 2018;109C:85–90.

[202] Orìo A, Corella J, Narvàez I. Performance of Different Dolomites on Hot Raw Gas Cleaning from Biomass Gasification with Air. Ind Eng Chem Res 1997;36:3800–8. doi:10.1021/ie960810c.

[203] Gil J, Caballero M a., Martín J a., Aznar M-P, Corella J. Biomass Gasification with Air in a Fluidized Bed: Effect of the In-Bed Use of Dolomite under Different Operation Conditions. Ind Eng Chem Res 1999;38:4226–35. doi:10.1021/ie980802r.

[204] Yin X, Wu CZ, Zheng SP, Chen Y. Design and operation of a CFB gasication and power generation system for rice husk. Biomass and Bioenergy 2002;23:181 – 187.

[205] Bhave AG, Vyas DK, Patel JB. A wet packed bed scrubber-based producer gas cooling–cleaning system. Renew Energy 2008;33:1716–1720.

[206] Pfeifer C, Hofbauer H. Development of catalytic tar decomposition downstream from a dual fluidized bed biomass steam gasifier. Powder Technol 2008;180:9–16.

[207] Anis S, Zainal Z a. Tar reduction in biomass producer gas via mechanical, catalytic and thermal methods: A review. Renew Sustain Energy Rev 2011;15:2355–77. doi:10.1016/j.rser.2011.02.018.

[208] Corella J, Caballero MA, Aznar M-P, Brage C. Two advanced models for the kinetics of the variation of the tar composition in its catalytic elimination in biomass gasification. Ind Eng Chem Res 2003;42:3001–3011.

[209] Pallozzi V, Di Carlo A, Bocci E, Villarini M, Foscolo PU, Carlini M. Performance evaluation at different process parameters of an innovative prototype of biomass gasification system aimed to hydrogen production. Energy Convers Manag 2016;130:34–43. doi:10.1016/j.enconman.2016.10.039.

[210] Savuto E, Di Carlo a., Bocci E, D'Orazio a., Villarini M, Carlini M, et al. Development of a CFD model for the simulation of tar and methane steam reforming through a ceramic catalytic filter. Int J Hydrogen Energy 2015;40:7991–8004. doi:10.1016/j.ijhydene.2015.04.044.

[211] Li Y, Fu Q, Flytzani-Stephanopoulos M. Low-temperature water-gas shift reaction over Cu-and Ni-loaded cerium oxide catalysts. Appl Catal B … 2000;27:179–91.

[212] Campbell J. Influences of catalyst formulation and poisoning on the activity and die-off of low temperature shift catalysts. Ind Eng Chem Process Des … 1970;9:588–95. doi:10.1021/i260036a016.

[213] Courson C, Lang C, Secordel X, Kiennemann A, Zimmermann I. Synthesis of Cu/Foam catalyst and characterization, Deliverable 2.5, Confidential Report, UNIFHY project #299732 in FP7. Strasbourg: 2014.

[214] Bakalis DP, Stamatis AG. Incorporating available micro gas turbines and fuel cell: Matching considerations and performance evaluation. Appl Energy 2013;103:607–17. doi:10.1016/j.apenergy.2012.10.026.

[215] Zhang N, Cai R. Analytical solutions and typical characteristics of part-load performances of single shaft gas turbine and its cogeneration. Energy Convers Manag 2002;43:1323–37. doi:10.1016/S0196-8904(02)00018-3.

[216] Elmo-Rietschle. Data sheet compressor G-BH1, 2BH1-910 2015. http://www.gd-elmorietschle.it/uploadedfiles/elmo-rietschle/downloads/content_g/datasheets/g-bh1_g-bh9/fc/2bh1910_fu_en.pdf.

[217] Joseph Mehrer GmbH & Co KG Maschinenfabrik. Oil-free Compression of Biogas and Biome hane 2015. http://www.dge-wittenberg.de/english/vortraege/Vortrag Biogas- und Biomethanverdichter 27.10.2006-EN.pdf.

[218] Joseph Mehrer GmbH & Co KG Maschienenfabrik. Datasheet Dry Cylinder Compressors 2015.

[219] Rep M. PSA unit design and construction, Deliverable 3.1, Confidental report, UNIFHY Project #299732 in FP7. 2014.

[220] UNIfHY Collaborative Project, Project ID 299732 7FP, n.d.

[221] Fremaux S, Beheshti S-M, Ghassemi H, Shahsavan-Markadeh R. An experimental study on hydrogen-rich gas production via steam gasification of biomass in a research-scale fluidized bed. Energy Convers Manag 2015;91:427–32. doi:10.1016/j.enconman.2014.12.048.

[222] Lv X, Xiao J, Du Y, Shen L, Zhou Y. Experimental study on biomass steam gasification for hydrogen-rich gas in double-bed reactor. Int J Hydrogen Energy 2014;39:20968–78. doi:10.1016/j.ijhydene.2014.10.083.

[223] Font Palma C. Modelling of tar formation and evolution for biomass gasification: A review. Appl Energy 2013;111:129–41. doi:10.1016/j.apenergy.2013.04.082.

[224] Han L, Wang Q, Yang Y, Yu C, Fang M, Luo Z. Hydrogen production via CaO sorption enhanced anaerobic gasification of sawdust in a bubbling fluidized bed. Int J Hydrogen Energy 2011;36:4820–9. doi:10.1016/j.ijhydene.2010.12.086.

[225] Acharya B, Dutta A, Basu P. An investigation into steam gasification of biomass for hydrogen enriched gas production in presence of CaO. Int J Hydrogen Energy 2010;35:1582–9. doi:10.1016/j.ijhydene.2009.11.109.

[226] Deganello F, Marcì G, Deganello G. Citrate-nitrate auto-combustion synthesis of perovskite-type nanopowders: A systematic approach. J Eur Ceram Soc 2009;29:439–50. doi:10.1016/j.jeurceramsoc.2008.06.012.

[227] Li W, Li J, Guo J. Synthesis and characterization of nanocrystalline CoAl2O4 spinel powder by low temperature combustion. J Eur Ceram Soc 2003;23:2289–95. doi:10.1016/S0955-2219(03)00081-5.

[228] Zaza F, Pallozzi V, Serra E, Pasquali M. Combustion synthesis of LaFeO3 sensing nanomaterial. AIP Conf Proc 2015;1667. doi:10.1063/1.4922559.

[229] Junliang L, Wei Z, Cuijing G, Yanwei Z. Synthesis and magnetic properties of quasi-single domain M-type barium hexaferrite powders via sol-gel auto-combustion: Effects of pH and the ratio of citric acid to metal ions (CA/M). J Alloys Compd 2009;479:863–9. doi:10.1016/j.jallcom.2009.01.081.

[230] Korotcenkov G. Materials for Thick Film Technology. In: Potyrailo RA, editor. Handb. Gas Sens. Mater. Prop. Advantages Shortcomings Appl. Vol. I Conv. Approaches, vol. 1, Springer Science+Business Media; 2013, p. 249–54. doi:10.1007/978-1-4614-7388-6.

[231] Zaki W, Suhaimizan W, Wagiran R, Noor M. Thick film paste preparation and characterization of BaTiO3 for humidity sensor. FEIIC Semin. Eng. Technol., Putrajaya, Malaysia: 2006, p. 417–24.

[232] Liu Z, Chung DDL. Burnout of the organic vehicle in an electrically conductive thick-film paste. J Electron Mater 2004;33:1316–25. doi:10.1007/s11664-004-0160-4.

[233] Yang WD, Haile SM. Highly preferred oriented lead barium titanate thin films using acetylacetone as chelating agent in a sol-gel process. Rev Adv Mater Sci 2005;10:143–8.

[234] Zardetto V, De Angelis G, Vesce L, Caratto V, Mazzuca C, Gasiorowski J, et al. Formulations and processing of nanocrystalline TiO2 films for the different requirements of plastic, metal and glass dye solar cell applications. Nanotechnology 2013;24:255401. doi:10.1088/0957-4484/24/25/255401.

[235] ISO 26142 Hydrogen Detector Apparatus - Stationary applications n.d.

[236] UL 2075 - Standard for Gas and Vapour Detectors and Sensors n.d.

[237] Boon-Brett L, Bousek J, Castello P, Salyk O, Harskamp F, Aldea L, et al. Reliability of commercially available hydrogen sensors for detection of hydrogen at critical concentrations: Part I - Testing facility and methodologies. Int J Hydrogen Energy 2008;33:7648–57. doi:10.1016/j.ijhydene.2008.10.004.

[238] NREL DoE. http://www.nrel.gov/hydrogen/facilities_hsl.html n.d.

[239] Bergman R, Lundstedt T, Abramo L, Pettersen J, Thelin B, Seifert E, et al. Experimental design and optimization. Chemom Intell Lab Syst 1998;42:3–40. doi:10.1016/S0169-7439(98)00065-3.

[240] Carlson R. Designs for explorative experiments in organic synthetic chemistry. Chemom Intell Lab Syst 2004;73:151–66. doi:10.1016/j.chemolab.2004.04.005.

[241] Law CK. Combustion physics. New York: Cambridge University Press; 2006. doi:https://doi.org/10.1017/CBO9780511754517.

[242] Li G, Zhang X, Kawi S. Relationships between sensitivity , catalytic activity , and surface areas of SnO 2 gas sensors 1999:64–70.

[243] Zaza F, Orio G, Serra E. Quality by design approach for SrTiO3 perovskite nanomaterials synthesis. J Mater Sci 2016;51:9649–68. doi:10.1007/s10853-016-0198-8.

[244] Martell AE, Smith RM. Critical Stability Constants, Volume 3: Other Organic Ligands. New York: Springer Science+Business Media; 1977. doi:10.1007/978-1-4757-1568-2.

[245] Smith RM, Martell AE. Critical Stability Constants, Volume 4: Inorganic Complexes. vol. 4. New York: Springer Science+Business Media; 1976.

[246] Lee WJ, Fang TT. The effect of the molar ratio of cations and citric acid on the synthesis of barium ferrite using a citrate process. J Mater Sci 1995;30:4349–54. doi:10.1007/BF00361516.

[247] Guo RS, Wei QT, Li HL, Wang FH. Synthesis and properties of La0.7Sr0.3MnO3 cathode by gel combustion. Mater Lett 2006;60:261–5. doi:10.1016/j.matlet.2005.08.027.

[248] Collins JM, Uppal R, Incarvito CD, Valentine AM. Titanium(IV) citrate speciation and structure under environmentally and biologically relevant conditions. Inorg Chem 2005;44:3431–40. doi:10.1021/ic048158y.

[249] Korotcenkov G. The role of morphology and crystallographic structure of metal oxides in response of conductometric-type gas sensors. Mater Sci Eng R Reports 2008;61:1–39. doi:10.1016/j.mser.2008.02.001.

[250] Pallozzi V, Di Carlo A, Zaza F, Villarini M, Carlini M, Bocci E. Perovskite sensing materials for syngas composition monitoring and biomass gasifier numerical model validation: A preliminary approach 2016;20002:20002. doi:10.1063/1.4954485.

[251] Scherrer P. Bestimmung der inneren Struktur und der Grobe von Kolloidteilchen mittels Rontgenstrahlen in Kolloidchemie Ein Lehrbuch. Berlin: Springer-Verlag Berlin Heidelberg; 1912.

[252] Pallozzi V, Zaza F, Di Carlo A, Bocci E, Carlini M. Gas sensors for sustainable and safe intergated gasification-FC system. Int J Hydrogen Energy 2017;42:29606–19. doi:https://doi.org/10.1016/j.ijhydene.2017.10.084.

[253] Carlo S Di, Falasconi M. Drift Correction Methods for Gas Chemical Sensors in Artificial Olfaction Systems: Techniques and Challenges. Adv. Chem. Sensors, In Tech; 2012, p. 305–26. doi:10.5772/33411.

[254] Lantto V, Saukko S, Toan NN, Reyes LF, Granqvist CG. Gas sensing with perovskite-like oxides having ABO3 and BO3 structures. J Electroceramics 2004;13:721–6. doi:10.1007/s10832-004-5182-z.

[255] Wærnhus I, Vullum PE, Holmestad R, Grande T, Wiik K. Electronic properties of polycrystalline LaFeO3. Part I: Experimental results and the qualitative role of Schottky defects. Solid State Ionics 2005;176:2783–90. doi:10.1016/j.ssi.2005.08.012.

[256] Wærnhus I, Grande T, Wiik K. Electronic properties of polycrystalline LaFeO3. Part II: Defect modelling including Schottky defects. Solid State Ionics 2005;176:2609–16. doi:10.1016/j.ssi.2005.07.014.

[257] Gurlo a., Bârsan N, Oprea a., Sahm M, Sahm T, Weimar U. An n- to p-type conductivity transition induced by oxygen adsorption on α-Fe2O3. Appl Phys Lett 2004;85:2280–2. doi:10.1063/1.1794853.

[258] Mizusaki J, Sasamoto T, Cannon WR, Kent Bowen H. Electronic Conductivity, Seebeck Coefficient, and Defect Structure of LaFe03. J Am Ceram Soc 1982;65:363–8.

[259] Tsipis EV, Patrakeev MV, Kharton VV, Yaremchenko AA, Mather GC, Shaula AL, et al. Transport properties and thermal expansion of Ti-substituted La1−xSrxFeO3−δ (). Solid State Sci 2005;7:355–65. doi:10.1016/j.solidstatesciences.2005.01.001.

[260] Solis JL, Golovanov V, Lantto V, Leppavuori S. A Study of Dual Conductance Response to Carbon Monoxide of CdS and a-SnWO4 Thin Films. Phys Scr 1994;T54:248–51.

[261] Moseley PT. New trends and future prospect of thick- and thin-film gas sensors. Sensors Actuators B 1991;3:167–74.

[262] Inoue T, Seki N, Kamimae J, Eguchi K, Arai H. The conduction mechanism and defect structure of acceptor- and donr-doped SrTiO3. Solid State Ionics 1991;48:283–8.

[263] Moos R, Menesklou W, Schreiner HJ, Härdtl KH. Materials for temperature independent resistive oxygen sensors for combustion exhaust gas control. Sensors Actuators, B Chem 2000;67:178–83. doi:10.1016/S0925-4005(00)00421-4.

[264] Liu BS, Wan ZY, Zhan YP, Au CT. Desulfurization of hot coal gas over high-surface-area LaMeOx/MCM-41 sorbents. Fuel 2012;98:95–102. doi:10.1016/j.fuel.2012.03.048.

[265] Hong YS, Zhang ZF, Cai ZP, Zhao XH, Liu BS. Deactivation Kinetics Model of H2S Removal over Mesoporous LaFeO3/MCM-41 Sorbent during Hot Coal Gas Desulfurization. Energy & Fuels 2014;28:6012–8. doi:10.1021/ef5008825.

[266] Fang H, Zhao K, Huamg Z, Li X, Wei G, Li H. Synthesis of three-dimensionally ordered macroporous LaFeO3 perovskites and their performance for chemical-looping reforming of methane. Chinese J Catal 2013;34:1242–9. doi:10.1016/S1872.

[267] Zhang X, Li H, Li Y, Shen W. Structural properties and catalytic activity of Sr-substituted LaFeO3 perovskite. Chinese J Catal 2012;33:1109–14.

[268] Levasseur B, Kaliaguine S. Methanol oxidation on LaBO3 (B=Co, Mn, Fe) perovskite-type catalysts prepared by reactive grinding. Appl Catal A Gen 2008;343:29–38. doi:10.1016/j.apcata.2008.03.016.

[269] Zhang L, Hu J, Song P, Qin H, An K, Wang X, et al. CO-sensing properties of perovskite La0.68Pb0.32FeO3 nano-materials. Sensors Actuators, B Chem 2006;119:315–8. doi:10.1016/j.snb.2005.12.030.

[270] Sun Y, Peng J, Chen Y, Yao Y, Liang Z. Triple-cation mixed-halide perovskites: towards efficient, annealing-free and air-stable solar cells enabled by Pb(SCN)2 additive. Sci Rep 2017;7:46193. doi:10.1038/srep46193.

[271] Lide DR. CRC Handbook of Chemistry and Physics Version 2005. Boca Raton, FL: CRC Press; 2005.

[272] Minh D Le, Nu V, Hoa M, Dinh NN, Thuy NT. Electric and Thermoelectric Properties of LaFeO 3 Compounds Doped by Ti , Co and Cu ions 2013;29:42–8.

[273] Yoon J-W, Choi J-K, Lee J-H. Design of a highly sensitive and selective C2H5OH sensor using p-type Co3O4 nanofibers. Sensors Actuators B Chem 2012;161:570–7. doi:10.1016/j.snb.2011.11.002.

[274] Tan J, Dun M, Li L, Zhao J, Tan W, Lin Z, et al. Synthesis of hollow and hollowed-out Co3O4 microspheres assembled by porous ultrathin nanosheets for ethanol gas sensors: Responding and recovering in one second. Sensors Actuators, B Chem 2017;249:44–52. doi:10.1016/j.snb.2017.04.063.

[275] An D, Li Y, Lian X, Zou Y, Deng G. Synthesis of porous ZnO structure for gas sensor and photocatalytic applications. Colloids Surfaces A Physicochem Eng Asp 2014;447:81–7. doi:10.1016/j.colsurfa.2014.01.060.

[276] Deng S, Chen N, Deng D, Li Y, Xing X, Wang Y. Meso- and macroporous coral-like Co<inf>3</inf>O<inf>4</inf> for VOCs gas sensor. Ceram Int 2015;41:11004–12. doi:10.1016/j.ceramint.2015.05.045.

[277] Wen Z, Zhu L, Mei W, Hu L, Li Y, Sun L, et al. Rhombus-shaped Co3O4 nanorod arrays for high-performance gas sensor. Sensors Actuators, B Chem 2013;186:172–9. doi:10.1016/j.snb.2013.05.093.

[278] Li T, Zeng W, Long H, Wang Z. Nanosheet-assembled hierarchical SnO2 nanostructures for efficient gas-sensing applications. Sensors Actuators, B Chem 2016;231:120–8. doi:10.1016/j.snb.2016.03.003.

[279] Che H, Liu A, Hou J, Mu J, Bai Y, Zhao S, et al. Solvothermal synthesis of hierarchical Co3O4 flower-like microspheres for superior ethanol gas sensing properties. J Mater Sci Mater Electron 2014;25:3209–18. doi:10.1007/s10854-014-2005-0.

[280] Jin WX, Ma SY, Tie ZZ, Jiang XH, Li WQ, Luo J, et al. Hydrothermal synthesis of monodisperse porous cube, cake and spheroid-like α-Fe2O3 particles and their high gas-sensing properties. Sensors Actuators B Chem 2015;220:243–54. doi:10.1016/j.snb.2015.05.098.

[281] Rao J, Yu A, Shao C, Zhou X. Construction of hollow and mesoporous ZnO microsphere: A facile synthesis and sensing property. ACS Appl Mater Interfaces 2012;4:5346–52. doi:10.1021/am3012966.